TECHNISCHE
UNIVERSITÄT
WIEN

DISSERTATION

Interfacial processes in adhesively bonded joints under corrosive load

zur Erlangung des akademischen Grades eines Doktors der technischen Wissenschaften

unter der Leitung von

Univ.Prof. Dipl.-Ing. Dr.techn. Markus Valtiner

Institut für Angewandte Physik, E134

eingereicht an der Technischen Universität WienFakultät für Physik

von

Dipl.-Ing. Tanja Denise Singewald

Matrikelnummer 01056257

Ort, Datum	(Unterschrift Verfasser)	(Unterschrift Betreuer)

ii

Eidesstattliche Erklärung

Ich erkläre an Eides statt, dass die vorliegende Arbeit nach den anerkannten Grundsätzen für wissenschaftliche Abhandlungen von mir selbstständig erstellt wurde. Alle verwendeten Hilfsmittel, insbesondere die zugrunde gelegte Literatur, sind in dieser Arbeit genannt und aufgelistet. Die aus den Quellen wörtlich entnommenen Stellen, sind als solche kenntlich gemacht.

Das Thema dieser Arbeit wurde von mir bisher weder im In- noch Ausland einer Beurteilerin/einem Beurteiler zur Begutachtung in irgendeiner Form als Prüfungsarbeit vorgelegt. Diese Arbeit stimmt mit der von den Begutachterinnen/Begutachtern beurteilten Arbeit überein.

Ich nehme zur Kenntnis, dass die vorgelegte Arbeit mit geeigneten und dem derzeitigen Stand der Technik entsprechenden Mitteln (Plagiat-Erkennungssoftware) elektronisch-technisch überprüft wird. Dies stellt einerseits sicher, dass bei der Erstellung der vorgelegten Arbeit die hohen Qualitätsvorgaben im Rahmen der geltenden Regeln zur Sicherung guter wissenschaftlicher Praxis „Code of Conduct" an der TU Wien eingehalten wurden. Zum anderen werden durch einen Abgleich mit anderen studentischen Abschlussarbeiten Verletzungen meines persönlichen Urheberrechts vermieden.

Linz, am 22.09.2022

_____

Unterschrift

iv

Contents

Acknowledgments

This work originates from research in DuraBond (FFG 865864 CEST-K1, 2019-2022) project and from research in strategic CIMCA (FFG 865864 CEST-K1, 2019-2022) project.

At first, I would like to express my gratitude to my supervisor Univ. Prof. Dipl.-Ing. Dr. techn. Markus Valtiner for your immense support throughout the entire course of this PhD thesis. I really appreciate that you always provided me with useful advice and helped me when I had questions or got stuck, but you also gave me enough space to grow and to figure things out on my own. In this context, I would also like to thank the entire Institute of Applied Physics. Even though I was a rather rare guest due to COVID, I was warmly welcomed every time. Laura Mears always took special care of me and I would like to thank you for your support.

Next, I would like to thank Alexander Balatka for the opportunity to do my PhD thesis at CEST Competence Center for Electrochemical Surface Technology GmbH. I really appreciate the positive atmosphere and the support of the whole team at CEST during my thesis. Especially the team at Linz has grown very close to my heart and many friendships have formed during my work. A special thanks goes to Laura, who has always supported me 100% as project manager during my work. I could not have asked for a better project manager to supervise my thesis. You always managed to motivate me and were always there for me when I needed help. I would also like to thank my second project manager Gabi. You awakened my enthusiasm for electrochemistry and actively supported me in my experiments such as the EIS measurements, SKP measurements and the development of the pH electrodes. I am very grateful that I was able to learn

from such an expert in this field. You also gave me many great moments at CEST with your humorous personality. I am also very grateful for all the PhD students at CEST. We could always rely on each other and exchange thoughts about the status and problems of our work and help each other. Here, I especially want to thank Ines and Thomas. I am very grateful to Ines for your help with the production of the niobium pH electrodes and for the training on various instruments. I especially appreciate your helpful, uncomplicated and diligent manner, with which we successfully wrote two papers. To my "diss buddy" Thomas, I am very grateful for the many hours you put up with me when I was stressed. Your advice was always very supportive and the result of the thesis would not have been the same without your help. You are extremely fun to be around, and the thesis would not have been such a great experience without you. Finally, I would also like to thank the technicians at CEST for their help. Especially Philipp helped me a lot with my corrosion tests, scratching my samples and I was able to learn a lot through his technical skills. In our leisure time, Philipp taught me how to prepare the perfect schilerol, challenged me to try many Asian delicacies like the thousand-year-old egg and always reminds me to never forget to ask, "How much is the fish?" when planning a holiday to an Asian country.

Thank you very much for taking the time to discuss my results with me in numerous meetings.

I would also like to thank my research partners Univ.-Prof. DI Dr. Christian Paulik and Assoc. Univ.-Prof. DI Dr. David Stifter from JKU Linz for their support.

Last but not least, I would like to express my gratitude to my friends and family for their support. They always believed in me and cheered me up in stressful and difficult times. A big thanks goes to Tina and Juliana for the many hikes and trips they took with me when I needed a break. Juliana, I am really looking forward to celebrating my finished dissertation with you in Norway with hopefully many orca sightings and polar lights. You really motivate me with the pictures you send me to keep going and do my best to finish the thesis in time. Madschi and Jana, I am very grateful that I could always count on you to have an open ear for me when needed. Lisa, I am grateful to you for going swimming with me every week and helping me to free my mind. I would also like to thank my friends Annika, Petra and Lisa for the numerous and fun game evenings and for the fact that I can count on you for advice on how to find a good balance between work and free time. I would also like to take this opportunity to thank my canoe polo team for the numerous training sessions, tournaments, white water paddling tours and camping trips. Without them, the time during my thesis would not have been as fun and varied.

Abstract

Adhesive bonding has become an accepted joining method in the automotive industry due to the increasing importance of lightweight construction and the use of multi-material design. However, water absorption is a problem as it can cause electrochemical reactions at the adhesive-metal interface, which can lead to degradation or even failure of the adhesive bond. In this study, several model formulations (MF) containing D.E.R. 331, DICY and additives commonly used in the adhesive industry are investigated to simulate a commercially available adhesive as well as a commercial formulation (CF) whose exact composition is unknown. This thesis therefore addresses a comprehensive approach using electrochemical techniques as well as corrosion tests to investigate the water absorption and delamination of the interface of galvanised steel/epoxy adhesive systems in NaCl solutions.

Electrochemical impedance spectroscopy (EIS) is used to determine the water uptake via the linear relationship of the wet coating dielectric constant and the dielectric constant of the dry coating. EIS measurements allowed to detect differences between the model and the commercially available adhesives which could be traced back to specific additives present in the commercially available adhesive. Admixing different concentrations of hollow glass microspheres (HGM) as well as other commonly used additives to the model formulation allowed to understand the significant different absorption behaviour of both adhesives and the role of admixed components. Whereas scanning Kelvin probe (SKP) measurements allowed to observe the preferred delamination process of our epoxy coated galvanized steel surfaces. Not only different adhesives but also different Zn coatings were tested to investigate the influence of different alloying elements such as aluminium and magnesium. It was found that pure zinc coatings mainly cause cathodic delamination, whereas a certain concentration of magnesium in the zinc coating leads to anodic delamination such as filiform corrosion.

In addition, metal oxide (MO_x) pH electrodes were fabricated from niobium to test whether these electrodes are suitable for future studies at the adhesive/metal interface. pH electrodes are valuable for corrosion research because the pH value can provide information about the corrosion mechanism, such as whether different polymer coated galvanized steel samples delaminate anodically or cathodically and reveal corrosion pathways. Niobium oxide (NbO_x) is a promising pH sensing material because it is easily available, inexpensive, chemically very stable, and non-toxic. Therefore, three fast and simple fabrication methods for NbO_x pH electrodes were tested, and the electrochemical fabrication method was found to produce pH electrodes with the highest reproducibility and the highest sensitivity of -41 mV/pH. In addition, their pH sensing and electrode performance properties were determined by measurements of open circuit potential (OCP) and long-term stability. Scanning electron microscopy (SEM), energy dispersive X-ray spectroscopy (EDX) and EIS were used to characterize the oxide layer. It was found that niobium-based pH electrodes have very good stability in corrosive environments and therefore could be a more affordable alternative to other MO_x electrodes.

Kurzfassung

Das Kleben hat sich in der Automobilindustrie aufgrund der zunehmenden Bedeutung des Leichtbaus und der Verwendung von Multimaterialkonstruktionen zu einer anerkannten Verbindungsmethode entwickelt. Die Wasseraufnahme stellt jedoch ein Problem dar, da sie elektrochemische Reaktionen an der Klebstoff-Metall-Grenzfläche hervorrufen kann, die zu einer Verschlechterung oder sogar zum Versagen der Klebverbindung führen können. In dieser Dissertation werden mehrere Modellformulierungen untersucht, die D.E.R. 331, DICY und in der Klebstoffindustrie übliche Additive enthalten, um einen handelsüblichen Klebstoff zu simulieren sowie eine kommerzielle Formulierung, deren genaue Zusammensetzung unbekannt ist. In dieser Arbeit wird daher ein umfassender Ansatz verfolgt, bei dem elektrochemische Techniken sowie Korrosionstests eingesetzt werden, um die Wasseraufnahme und Delaminierung an der Grenzfläche von verzinktem Stahl/Epoxid-Klebstoffsystemen in NaCl-Lösungen zu untersuchen. Mit Hilfe der elektrochemischen Impedanzspektroskopie wird die Wasseraufnahme über die lineare Beziehung zwischen der Dielektrizitätskonstante der nassen Beschichtung und der Dielektrizitätskonstante der trockenen Beschichtung bestimmt.

Mit Hilfe der EIS-Messungen konnten Unterschiede zwischen der Modellformulierung und dem kommerziellen Klebstoff festgestellt werden, die auf spezifische Additive im handelsüblichen Klebstoff zurückgeführt werden konnten. Die Beimischung verschiedener Konzentrationen von Mikrohohlglaskugeln sowie anderer üblicherweise verwendeter Zusatzstoffe zur Modellformulierung ermöglichte es, dass deutlich unterschiedliche Absorptionsverhalten der beiden Klebstoffe und die Rolle der beigemischten Komponenten zu verstehen. Messungen mit der Raster-Kelvin-Sonde ermöglichten die Bestimmung des bevorzugten Delaminationsprozess auf den epoxidbeschichteten verzinkten Stahloberflächen. Neben den unterschiedlichen Klebstoffen wurden auch verschiedene Zn-

Beschichtungen getestet, um den Einfluss verschiedener Legierungselemente wie Aluminium und Magnesium auf den Delaminationsprozess zu untersuchen. Es stellte sich heraus, dass reine Zinküberzüge hauptsächlich kathodische delaminieren, während eine bestimmte Konzentration an Magnesium in Zinkbeschichtung zu anodischer Delaminierung wie Filiformkorrosion führt.

Darüber hinaus wurden Metalloxid pH-Elektroden aus Niob hergestellt, um zu testen, ob diese Elektroden für künftige Studien an der Klebstoff/Metall-Grenzfläche geeignet sind. pH-Elektroden sind für die Korrosionsforschung wertvoll, da der pH-Wert Informationen über den Korrosionsmechanismus liefern kann, z. B. ob verschiedene polymerbeschichtete verzinkte Stahlproben anodisch oder kathodisch delaminieren und Korrosionspfade aufzeigen. Nioboxid ist ein vielversprechendes Material für pH-Messungen, da es leicht verfügbar, kostengünstig, chemisch sehr stabil und ungiftig ist. Daher wurden drei schnelle und einfache Herstellungsmethoden für NbO_x pH-Elektroden getestet und es zeigte sich, dass die elektrochemische Herstellungsmethode pH-Elektroden mit der höchsten Reproduzierbarkeit und der höchsten Empfindlichkeit von -41 mV/pH ergibt. Darüber hinaus wurde die Elektrodenperformanz durch OCP-Messungen und Langzeitstabilitätsmessungen bestimmt. Zur Charakterisierung der Oxidschicht wurden Rasterelektronenmikroskopie (SEM), energiedispersive Röntgenspektroskopie (EDX) und EIS eingesetzt. Es wurde festgestellt, dass pH-Elektroden auf Niob Basis eine sehr gute Stabilität in korrosiven Umgebungen aufweisen und daher eine kostengünstigere Alternative zu anderen MO_x-Elektroden darstellen könnten.

Glossary

Abbreviations

1K	One-component
AFM-IR	Atomic force microscopy-based infrared spectroscopy
ATR-FTIR	Attenuated total reflection–Fourier transform infrared spectroscopy
BIW	Body-in-white
B-K	Brasher-Kingsbury
CE	Counter electrode
CF	Commercial formulation
CSP	Cross-section polishing
DSA	Dimensionally stable anode
EDX	Energy-dispersive X-ray spectroscopy
EIS	Electrochemical impedance spectroscopy
FIB	Focused ion beam
HGM	Hollow glass microspheres
HR-SKP	Height-regulated scanning Kelvin probe
IRRAS	Infrared reflection-absorption spectroscopy
JF	Jeffamine formulation
LC	Linear combination/relationship
LDH	Layered double hydroxides
MF	Model formulation
MO_x	Metal oxide
NbO_x	Niobium oxide
NSS	Neutral salt spry test
OCP	Open circuit potential
ORR	Oxygen reduction reaction
RE	Reference electrode

SEM	Scanning electron microscopy
SGM	Solid glass microspheres
SHE	Standard hydrogen electrode
SKP	Scanning Kelvin probe
ToF-SIMS	Time-of-flight secondary ion mass spectrometry
ULAM	Ultra-low angle microtome
WE	Working electrode
XPS	X-ray photoelectron spectroscopy
ZE	Electrogalvanized steel
ZM	Zn-Al-Mg hot-dip galvanized steel

Part I

Introduction

Chapter 1

Motivation and Literature Reviews

1.1 Literature background

1.1.1 Adhesive bonding in the automotive industry

Adhesive bonding has become increasingly important in the automotive industry due to lightweight construction, design flexibility and multi-material structures to reduce CO_2 emissions and fuel consumption. Furthermore, adhesive bonding can be used to increase the crash performance and therefore the safety of the car, because continuous bonding often results in stronger and stiffer structures and the more uniform stress distribution under load ensures that local stress concentrations are avoided [1,2]. Fig. 1.1 illustrates examples where adhesive bonding is used in a vehicle. Adhesives commonly used in the automotive industry are structural adhesives such as epoxy resins [2–4]. Structural adhesives were first reported to be used during the First World War for bonding the wooden frames of Mosquito aircraft. From the 1950s, the motivation for the aerospace industry increased to replace mechanical fasters with adhesives to reduce the weight as well as costs and to prolong the aircraft life. Only from the late 1960s, structural adhesives were used in the automotive industry [2,5,6].

Adhesive bonding also comes with some disadvantages. One of the most important one is the durability of the bonded joints when exposed to harsh conditions, such as water and corrosive surroundings [2,7]. It is known that all adhesives permeable water, although to varying extent [2,8]. Once water enters the adhesive joints, they can be weakened in several ways. For example, the absorbed water leads to plasticization of the adhesive and thus weaken the bond. Plasticization is a reversible process and although it is usually a weakening effect, low water concentrations can sometimes lead to strengthening of the bond [2,8–10]. Another

important degradation process is related to free energy. Here, the adhesive is most likely displaced by the water and physical effects such as Van der Waals interactions can no longer take place [8]. Other possible effects that water can have on adhesive joints are swelling which can cause internal stress or corrosion of the underlaying metal substrate when the water reaches the interface between the adhesive and the metal substrate [2,8,11–13]. The impact of adhesive failure can be devastating in the automotive industry. It can cause the operation of the car to be hindered and the safety of the driver to be compromised [1,14]. Although the processes are better understood and many studies have been carried out, the exact effects and mechanisms of adhesive debonding especially with commercially available adhesives and commonly used additives under corrosive load are not yet fully understood.
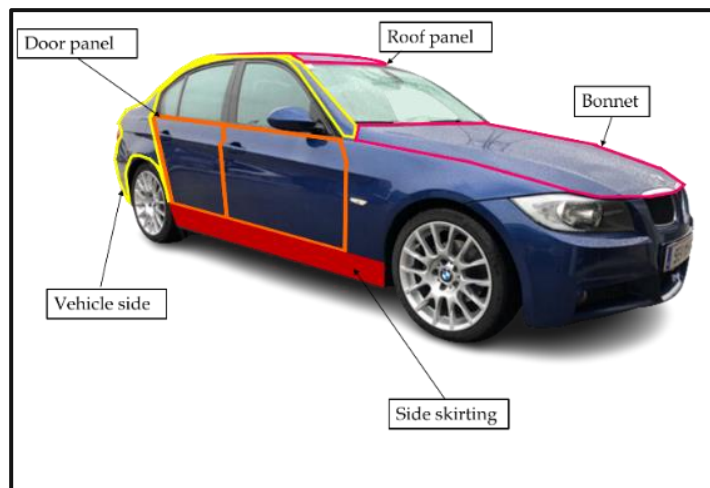
Figure 1.1: A vehicle with marked areas where adhesives are frequently used.

1.1.2 Theories of adhesion

To better understand delamination processes at the adhesive/metal interface, it is necessary to know the main theories of adhesion, which include mechanical theory, physical adsorption, chemical bonding, diffusion theory and electrostatic theory. Despite the numerous theories, the mechanism responsible for adhesion is much

more complex and not yet fully elucidated [2,15–18]. Fig. 1.2 illustrates some of the most important adhesion models, which are also summarised below:

- **Mechanical theory:** This concept was proposed by McBain and Hopkins in 1925 and is the oldest adhesion theory [19]. The mechanical theory is also referred to as mechanical interlocking because the adhesive is keying into the surface of the adherend where it fills the cavities and pores. Therefore, this theory states that the strength of the adhesion is directly depending on the porosity and roughness of the substrate [15,20–22]. However, this theory is controversial because a higher porosity means also an increase in the surface area of the substrate and thus could mean an increase in the number of chemical bonds, which results in higher adhesive strength [23]. In addition, good adhesion can also be obtained on smooth surfaces and is not limited to porous surfaces [24]. Whether this theory applies to adhesion between a polymer/metal interfaces is strongly dependent on the topographic properties of the metal substrate as well as on the wetting ability of the adhesive [25].

- **Physical adsorption:** Physical adsorption only occurs when two materials are in close molecular contact. Here, adhesion relies on secondary molecular forces such as van der Waals forces, which are the weakest of all intermolecular forces, have a very short range and are experienced just by a single or double molecular layer in the interfacial layers. Van der Waals forces contribute to all adhesive bonds, including the adhesion between the polymer/metal interface [15,26,27]. Depending on whenever non, one or both of the paired atoms have electric dipoles, the van der Waals forces are classified as London, Debye and Keesom forces [2,26,28].

- **Chemical bonding:** Chemical bonding is similar to physical adsorption but involves the formation of stronger primary chemical bonds such as covalent, ionic bonds, hydrogen bonds or acid-base interactions. Here, the reactivity of the adhesive and the adherend depends on whether a chemical bond is formed or not [27,29]. One of the most important interactions that occur at a polymer/metal interface is the acid-base interaction. Here, an acceptor

interacts with an electron pair donor. The acceptor consists of unoccupied levels with an affinity for electrons, while the donor has a lone pair of electrons. According to Brønsted, an acid is a proton donor and a base is a proton acceptor. A Lewis base, on the other hand, has a lone pair of electrons that can be used to complete the valence shell of a Lewis acid. Lewis acid-base interactions play an important role in adhesion at polymer/metal oxide interfaces [2,30].

- **Diffusion theory:** The basic principles of the diffusion theory of adhesion were established by Voyutskii and are mainly applicable for adhesion between two polymers and therefore not so relevant for adhesion between polymers and metals. The diffusion is based on micro-Brownian motion [18,26,31]. In order to develop a bond, it is necessary for the adhesive to contain a solvent for the adherend. Adhesion is generated when there is interdiffusion of molecules in and between the adhesive and adherend. With two polymer surfaces, the bond is formed by the interdiffusion of the polymer molecules on the first surface into the molecular network of the second polymer surface. In this process, interdiffusion strongly depends on the duration of contact, the temperature, the structure of the polymers and the polymer molecular weight [15,26,32].

- **Electrostatic theory:** Derjaguin was the first to introduce the electrostatic theory of adhesion, in which the adhesive and the material to be bonded are brought into contact (e.g., a polymer and a metal substrate) and on which their surfaces function like the plates of a plate capacitor. Charge is then transferred from one surface to the other, which can be compared to electrochemical processes, but in the absence of an electrolyte. Due to the charge transfer of the dissimilar surfaces, an electrical double layer is formed at the interface, which causes adhesion [15,16,33].
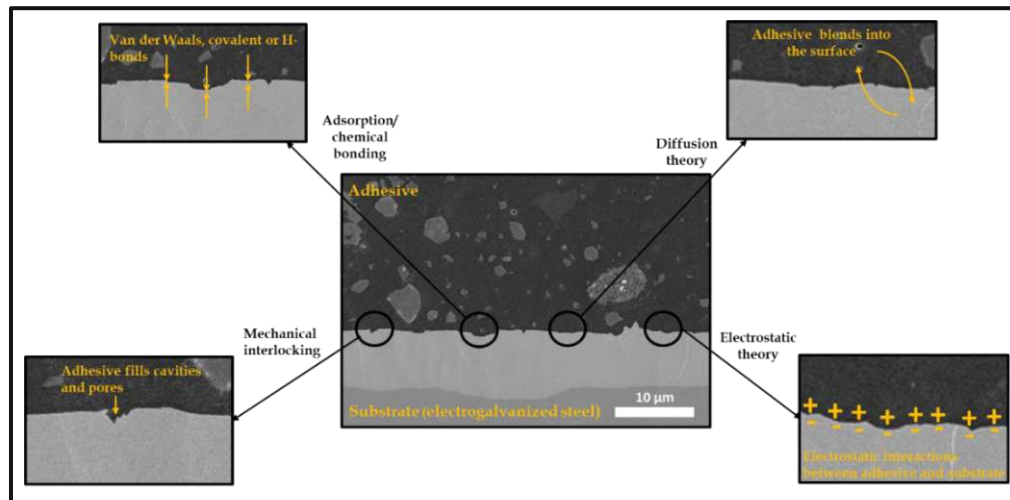
Figure 1.2: Schematic overview of the main adhesion theories including the mechanical interlocking, adsorption and chemical bonding as well as the diffusion and electrostatic theory reproduced after [2].

1.1.3 Effect of water on the adhesive/metal interface

Water can get into the adhesive/metal interface in several ways. One is through capillary action, which can occur when organic coatings have pores or small defects such as cracks. Another way water can penetrate into the polymer is through a concentration gradient that forms if the adhesive is exposed to an aqueous solution or a humid environment [34–36]. According to E. McCafferty, there are three mechanisms that may cause delamination when water penetrates into the polymer/oxide-coated metal interface. The first is the dissolution of the metal oxide film due to a local increase in pH. The second is also due to a strong alkaline environment, which can lead to the degradation of the adhesive. In addition, loss of adhesion at the interface between the adhesive and the oxide-coated metal is possible. The loss of adhesion can be caused either by chemical separation when the water molecules interact with covalent, hydrogen or polar bonds at the interface, while mechanical disbonding can be caused by water accumulation and osmotic pressure [35]. In addition to delamination of the adhesive due to chemical reactions or loss of physical forces at the polymer/metal interface, cathodic and anodic delamination are also well known in the automotive industry. Both delamination processes are caused by the formation of an electrochemical cell in which the anode

and cathode are connected by water as the electrolyte [37,38]. Since cathodic and anodic delamination, especially filiform corrosion, and osmotically induced blistering were the main delamination processes observed in this work, a more detailed literature review of these processes at the adhesive/metal interface is given below:

- **Cathodic delamination:** Cathodic delamination is often found on metals like iron or zinc which form conductive oxides on the metal surface [39]. In the 1980s, numerous research papers on cathodic delamination were written by H. Leidheiser *et al.* and W. Funke. Although cathodic delamination was already known before the 1980s, these two research groups contributed significantly to a better understanding of the mechanism behind cathodic delamination [40–42]. A schematic illustration of cathodic delamination along an adhesive/galvanized steel interface where the defect is in close contact with a NaCl solution is shown in Fig. 1.3. As shown in Fig. 1.3, if there is a defect in the coating and it comes into contact with an electrolyte such as water or seawater, metal dissolution can occur on the uncoated metal surface. When the metal is oxidised, electrons are released and the free electrons on the metal surface are consumed by the oxygen reduction reaction (ORR) under the intact polymer/metal interface. During the ORR, mainly hydroxyl ions are formed, leading to the build-up of an alkaline atmosphere under the coating, which can lead to bond breakage at the interface. In addition to hydroxyl ions, other active intermediates such as peroxides and free radicals are also formed, which can also contribute to delamination of the organic coating. In this process, the defect serves as the local anode and the intact polymer/metal interface as the local cathode. The electrolyte connects the local anode and the local cathode. As a result of an excess of negative charge under the coating, hydrated sodium ions migrate from the anodic site to the cathodic site leading to the formation of a galvanic element. In epoxy coatings, including epoxy-based structural adhesives, cation transfer from the defect to the cathodic site is assumed to be the rate-determining step for cathodic delamination [43–45].
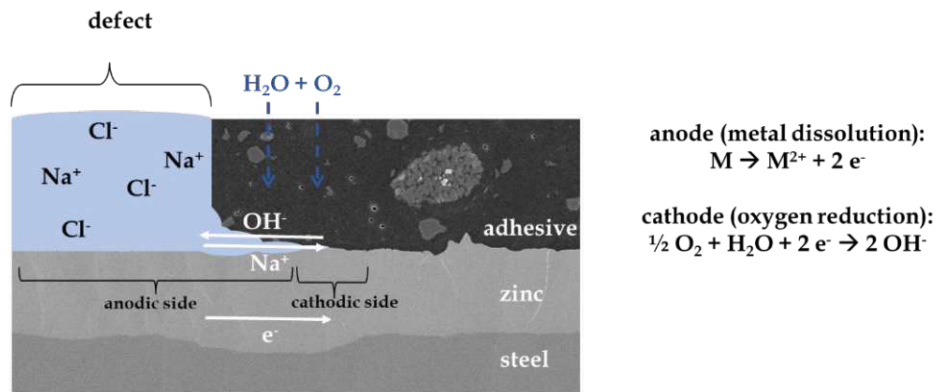
Figure 1.3: Schematic illustration of cathodic delamination along an adhesive/galvanized steel metal interface where the defect is in contact with a NaCl solution reproduced after [45].

- **Anodic delamination:** Anodic delamination is often referred to as anodic undermining. Compared to cathodic delamination, the position of the local anode and cathode is reversed. The anodic metal dissolution reaction takes place under the coating while the cathodic ORR takes place in the defect. Fig 1.4 describes anodic undermining along an adhesive/Zn-Al-Mg hot-dip galvanized steel interface where the local anode and local cathode are connected by an electrolyte forming a galvanic element. Anodic delamination is particular often found on aluminium surfaces. Many studies demonstrated that anodic delamination, especially filiform corrosion, which is a special form of anodic undermining, occurs on polymer coated zinc alloy surfaces containing magnesium [13,46–49].
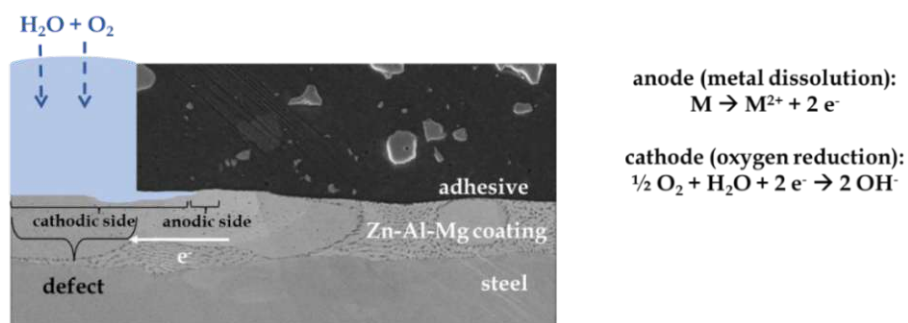
Figure 1.4: Schematic illustration of anodic undermining along an adhesive/Zn-Al-Mg hot-dip galvanized steel interface where the local anode and local cathode are connected by an electrolyte.

9

- **Filiform corrosion:** Filiform corrosion was first studied by Sharman in 1944 [50]. This type of delamination often occurs on polymer coated aluminium, magnesium and iron surfaces when they come into contact with aggressive anions such as chloride ions or when they are exposed to a very humid environment. Fig. 1.5 shows the structure of a corrosion filament at the interface between an adhesive and galvanised steel, where the zinc layer also contains magnesium and aluminium. The filament has a tail and a head, with the head acting as the active corrosion cell and moving across the metal surface. The tail is formed by the formation of inert corrosion products behind the head of the filament which creates a differential aeration cell [47,51]. A. Bautista describes that there are two cathodic sites, one at the end of the head and one around the head of the filament, which was also observed by potential and pH measurements. The anode is at the front of the head and the pH is usually between 1 and 4, depending on the metal surface, while the cathodic sites have alkaline pH values. [47].
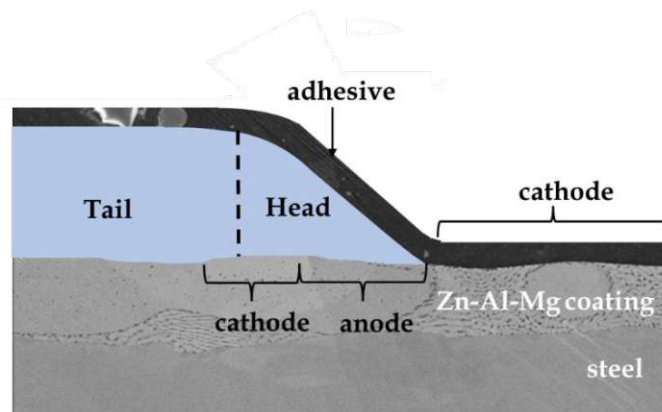
Figure 1.5: Schematic illustration of a corrosion filament at the adhesive/galvanized steel interface reproduced after [47].

- **Osmotically induced blistering:** Osmosis is believed to be one of the main mechanisms causing blistering of organic coatings on steel substrates [52]. When an intact polymer coating, such as an epoxy adhesive, is in close contact with an aqueous environment that is free of solutes or has a lower solute concentration than under the coating, a

semi-permeable membrane can be formed at the polymer/metal interface in combination with water-soluble compounds, often inorganic salts. The membrane formed allows diffusion of water but is impermeable to dissolved solids, resulting in a concentration gradient across the polymer film where the concentration of solutes at the polymer/metal interface is significantly higher than at the outer surface of the coating. Therefore, water is drawn through the film towards the concentrated solute under osmotic pressure. This water transfer takes place because both the water pressure and the salt concentrations on both sides of the membrane strive for equilibrium [53,54]. Blistering then occurs due to the deformation pressure caused by the water entering the polymer/metal interface [52].

1.1.4 State of the art for investigating the buried polymer/metal interface

Investigating the buried polymer/metal interface is often a difficult task, as the interface is located under a µm-thick polymer layer that is difficult to measure using conventional analytical methods. A variety of methods have been used to reach or simulate the interface. One simple method is the mechanical removal of the coating, which can lead to a deformation of the interface and was therefore not considered in this work [55]. A more convenient method might be cross-section techniques such as cross-section polishing (CSP) or focused ion beam (FIP), which allow the buried polymer/metal interface to be accessed with little risk of damage to the interface. The disadvantage, however, is that the interface is then directly exposed to the environment [55,56]. In literature, sputtering with C_{60} ions [57] and Ar [58], ultra-low angle microtome (ULAM) [59,60] and cryo-ULAM [61] are also cited as suitable methods for exposing the buried polymer/metal interface and subsequent examination of the exposed interface with analytical methods such as X-ray photoelectron spectroscopy (XPS), time-of-flight secondary ion mass spectrometry (ToF-SIMS) or atomic force microscopy-based infrared spectroscopy AFM-IR [56,57,60,61].

In this work, however, we have prioritised the use of non-destructive methods for investigating the buried polymer/metal interface, of which we give a rough

overview below. Fig. 1.6 lists a few methods found in literature to investigate the buried interface in a destructive and non-destructive way.
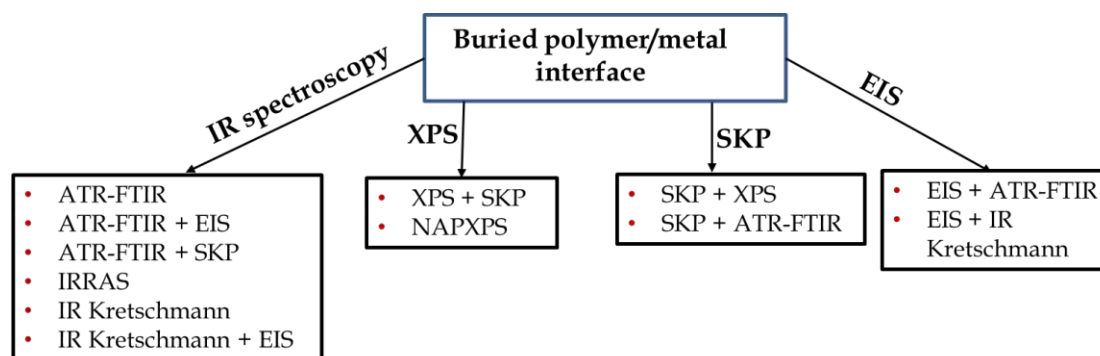
Figure 1.6: An overview of a few commonly used methods to investigate the buried polymer/metal interface.

A frequently used method is to apply model molecules to the metal oxide surface and study their interactions, e.g. using infrared reflection-absorption spectroscopy (IRRAS). Van den Brand *et al.* (2004) used anhydride and carboxylic acid based compounds widely used in the adhesives industry and investigated the chemical bonding of these compounds on aluminium substrates using IRRAS. This is a relatively simple method to simulate a buried polymer/metal interface and obtain valuable information about interfacial interactions. However, the disadvantages of this method are that the polymer coating is not made of monomers, which means that the simulated interface is not very realistic, and that a highly reflective substrate surface is required [55,62].

Another in-situ infrared spectroscopy method to study the buried interface is attenuated total reflection-Fourier transform infrared spectroscopy (ATR-FTIR) in Kretschmann geometry, which was used by Taheri *et al.* (2013) to study ionic bond formation between Zn surfaces and carboxylic polymers [63]. This method is a non-destructive method that also relies on the use of thin polymer films or thin metal (oxide) films. Unlike IRRAS or many other methods, the Kretschmann geometry allows the infrared beam to reach the buried interface not only from the polymer side but also from the metal (oxide) side. It is an appropriate method to measure the transport of water or ionic species through the polymer film to the polymer/metal

interface and is often combined with EIS [55,63–65].

It is also possible to study water transport along the buried polymer/metal interface with HR-SKP. Both EIS and HR-SKP were found to be excellent for studying commercial adhesives as well as model formulations and were therefore used throughout this thesis. A more detailed description of both methods can be found in Chapters 2.3 and 4 and is therefore not explained here.

As described in Chapter 1.1.3, the pH values at the local cathode and the local anode change when a galvanic element forms between the defect and the intact polymer/metal interface due to the absorption of water in the coating. At the cathode, the pH becomes strongly alkaline due to the formation of hydroxide ions by the oxygen reduction reaction whereas at the anode the pH-value becomes more acidic. Measuring of the pH-value at the polymer/metal interface clearly should indicate if the coated metal delaminates cathodically or anodically. Micro- MO_x pH electrodes are one way to measure the pH value at the polymer/metal interface. An overview of already existing micro-MO_x pH electrode and their application in corrosion research is given in Chapter 5.1.

1.2 Motivation and outline of this thesis

1.2.1 Research aim

Within the framework of the DuraBond "Durability of high strength adhesives and adhesive bonds under corrosive load" project and considering the literature background presented above, the following research questions were defined for this PhD thesis in agreement with all company and research partners:

- How to reliably measure water/ion diffusion at the metal/adhesive interface?

- What influence does the composition of the adhesive and the surface chemistry of the metal substrate have on water absorption and the delamination process?

- What methods can be used to electrochemically identify the delamination

processes under an organic coating?

- How can a low-cost, robust and easy-to-manufacture pH electrode be produced for future pH measurements at the adhesive/metal interface? Which metal oxide would be suitable for such measurements?

1.2.2 Thesis outline

This thesis consists of six chapters. The first chapter contains the motivation for this work as well as a comprehensive literature review, while Chapter 2 gives an overview of the main methods used in the course of the work. Starting with a brief introduction to the electrochemistry of corrosion, followed by the basics of electrochemical impedance spectroscopy and the height-regulated scanning Kelvin probe.

In Chapter 3 "Water absorption in hollow glass microspheres and its influence on cathodic and anodic delamination along the polymer/metal interface", it was shown that EIS can be used to investigate commercial adhesives with additives rather than simplified adhesive systems without additives. Here, EIS enabled the estimation of water absorption in hollow glass microspheres, which are important lightweight fillers for structural adhesives. Additionally, the delamination process on two galvanized steel substrates were confirmed using HR-SKP. The results are in good agreement with standardised corrosion tests that were additionally carried out to investigate the influence of HGM on the corrosion resistance of epoxy adhesives.

Chapter 4 "Systematic variation of inorganic additives and their impact on interfacial delamination processes of automotive coating systems" deals with the effects of inorganic additives, in particular CaO, $CaCO_3$ and hydrophobic fumed SiO_2, on various delamination processes. As in Chapter 3, the water absorption behaviour is determined by means of EIS. The results are compared with results from the cataplasma test. The blistering that occurs on the ZE substrate is investigated with additional cataplasma tests under oxygen-

depleted and oxygen-rich atmospheres to determine whether blistering is caused by osmotic blistering or cathodic delamination.

Since the pH value is an important parameter in corrosion research because it can provide information about the corrosion mechanisms that may occur at the polymer/metal interface, Chapter 5 "Versatile, low-cost, non-toxic niobium-based potentiometric pH sensors" focuses on the production of niobium-based pH sensors that are low-cost, non-toxic, easy to produce and have excellent long-term stability. Three different manufacturing routes were compared and the characterisation of the fabricated NbO_x electrodes was performed by SEM, EDX and EIS.

Chapter 6 "Conclusion and outlook" gives an overview of the most important results of this thesis as well as a brief outlook.

Chapter 2

Methodology

This section provides an overview of the relevant methods used in the present work. The exact execution of the measurements can be found in the individual chapters. Firstly, electrochemistry, in particular electrochemical impedance spectroscopy, which was used to determine the water absorption of the different adhesive formulations and to investigate the influence of commonly used additives such as the hollow glass microspheres, $CaCO_3$, CaO and hydrophobic fumed SiO_2 on the water uptake **(see Chapters 3 and 4)**. EIS was also used for the characterization of the NbO_x pH electrodes. Despite EIS measurements, cyclovoltammetry, polarization and open circuit potential measurements were carried out to either prepare the pH electrodes or to determine its performance **(see Chapter 5)**. For the identification of the delamination process along the buried adhesive/galvanized steel interface, a heigh-regulated scanning Kelvin probe (HR-SKP) was used **(see Chapter 3)**.

2.1 Electrochemistry of corrosion

Electrochemistry is a quite old science that deals with chemical reactions in which electrons are transferred at the interface between an electrode and an electrolyte. Here, the electrode can be either a metal or a semi-conductor, whereas the electrolyte is a solution that acts like an ionic conductor. A well-known example of an electrochemical process in material science or nature is corrosion of metals in an aqueous environment. Corrosion of metals with its environment occurs through coupled electrochemical half-

cell reactions that can lead to deterioration or decomposition of the metal. One half-cell reaction is the oxidation reaction, where the electrons are produced. The other half-cell reaction is the reduction reaction, in which the electrons are consumed. Here, the dissolution of the metal is indicated by the oxidation reaction at a local anode as follows [66,67]:

$$M \rightarrow M^{z+} + ze^- \tag{2.1}$$

The cathodic reaction to this is the reduction reaction. In corrosion processes, a common cathodic reaction in neutral or basic environments is the oxygen reduction reaction, in which dissolved oxygen reacts with water to form hydroxyl ions as follows [67]:

$$O_2 + 2H_2O + 4e^- \rightarrow 4OH^- \tag{2.2}$$
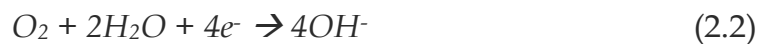
However, in acidic solutions, the predominant cathodic reaction is hydrogen evolution on metal surfaces as follows [67]:

$$2H^+ + 2e^- \rightarrow H_2 \tag{2.3}$$

The driving force for the electron flow, also called corrosion current, is the potential difference between the corresponding cathodes and anodes. A higher potential difference leads to an acceleration of the corrosion process [68,69].

Thermodynamically, when a metal corrodes, there is a change in the Gibbs free energy, which corresponds to the work associated with the corrosion reaction. The spontaneity of such reactions is usually determined by a decrease in Gibbs free energy ($\Delta G < 0$) [69,70]. Marcel Pourbaix invented potential-pH diagrams to sum up thermodynamic information about corrosion of different metals and to show the stability of those metals as a function of potential and pH. Even though the kinetic aspects have been neglected here, Pourbaix diagrams are useful to predict the corrosion tendency of metals [69,71]. Fig. 2.1 illustrates the Pourbaix diagram of an Fe-H_2O system, where the regions of corrosion, immunity and passivity are

marked. The horizontal lines indicate electron transfer reactions that are potential-dependent, while the vertical lines represent reactions that do not involve electron transfer and are pH-dependent. The diagonal lines represent the redox potentials of a solution in a state of equilibrium with hydrogen and oxygen. These equilibria are potential- and pH-dependent. The dotted lines, however, represent the hydrogen and oxygen lines in the Pourbaix diagram [69].
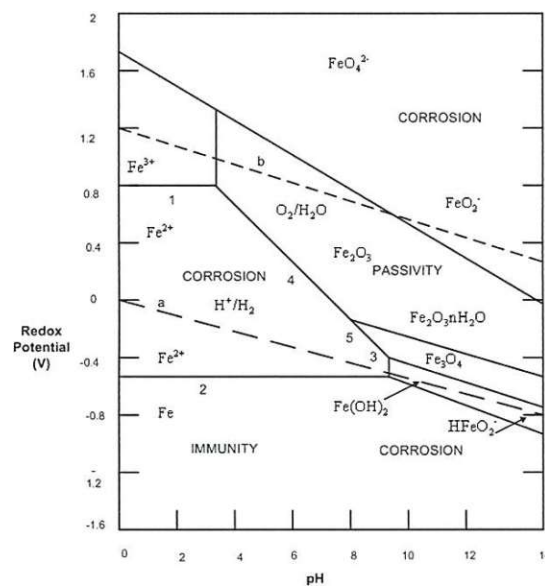

Figure 2.1: Potential-pH diagram for an iron-water system. Reprinted with permission from [69].

2.2 Electrochemical Impedance Spectroscopy

EIS was mainly used to measure the water uptake and the effective water diffusion coefficients for all coatings on ZE or ZM substrates throughout the entire work. The setup of the electrochemical cell for the EIS measurements is illustrated in Fig. 2.2. A three-electrode cell arrangement was used, where the coated sample was the working electrode, a dimensionally stable anode (DSA)

was used as the counter electrode (CE) and an Ag/AgCl (3 M KCl) electrode as the reference electrode (RE) with a 3.5 wt% NaCl solution as the electrolyte. A CompactStat from IVIUM technologies was used for the impedance measurements. The electrochemical impedance spectra were evaluated with the software ZView and IVIUM soft. The measurements were performed in a frequency range of 10^3-$10^{4.5}$ Hz with an AC disturbance of 10 mV with respect to the OCP of the system at room temperature. A detailed description on how the water uptake and the effective water diffusion coefficients were calculated from the EIS data can be found in Chapter 3.
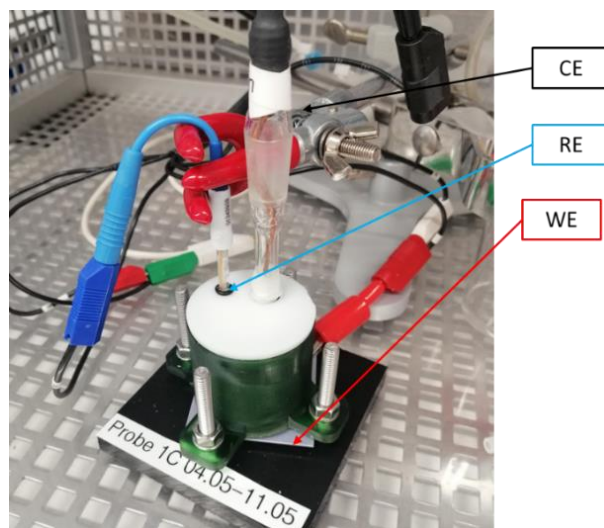
Figure 2.2: The setup of the electrochemical cell for the EIS measurements.

For the characterisation of the oxide layers and for the determination of the porosity of the fabricated NbO_x pH electrodes, EIS measurements were conducted. As with the water uptake measurements, a three-electrode cell arrangement consisting of a dimensionally stable anode as CE, an Ag/AgCl/3 M KCl electrode as RE and the NbO_x electrode as WE was used here. Measurements were carried out at room temperature in a 3.5 wt% NaCl solution and with a frequency range of 10^{-2}-10^4 Hz using a 10 mV AC perturbation at the OCP which was determined before EIS. For these measurements, the EIS spectra were fitted using ZView software (Scribner

Associates, United States).

2.3 Heigh-regulated scanning Kelvin probe

HR-SKP has proven to be a powerful, versatile and non-destructive tool for investigating delamination processes of organic coatings on metal substrates. The SKP technique was first introduced to electrochemical corrosion by M. Stratmann and H. Streckl. Fig. 2.3a demonstrates the set-up of an SKP technique. As illustrated in the figure, the SKP consists of a vibrating probe tip that forms a capacitor when brought to a short distance from the sample surface. An image of the experimental set-up of the SKP in the climate chamber used throughout the entire work is shown in Fig. 2.3b. If the tip, which acts as the reference electrode and the sample are made of different metals and are brought into contact, the different Fermi levels lead to a potential gradient that can be used to determine the contact potential difference (CPD) or the Volta potential difference $\Delta\psi$ between a WE and the vibrating RE. As shown in Fig. 2.3c, the equilibrium of the Fermi levels leads to a Volta potential difference because of the correlated charge transfer. Applying an external bias voltage between the sample and the tip equalises the Volta potential difference and the two surfaces are no longer charged [72,73].

The SKP was mainly used in this dissertation to investigate the delamination processes of close-to-reality adhesive formulations on different galvanized steel surfaces. For this purpose, an artificial defect was created with a scalpel and then an untreated wool thread was placed inside the defect. The exact procedure of the measurement as well as a detailed description of the sample preparation for the SKP measurements can be found in Chapter 3.2.6. The climate chamber made it possible to carry out measurements under elevated oxygen concentration and thus accelerate the delamination processes. Furthermore, due to the climate chamber and a humidity sensor, measurements could be carried out with a relative humidity of 96 %. The prepared samples were then stored in the humid climate chamber for at

least 10 hours to eliminate electrostatic charges. Delamination was then initiated by soaking the wool threads with 0.5 M NaCl solution. The surface scans were performed with an HR-SKP from Wicinski-Wicinski GbR. The SKP tip used consisted of 80 wt.% Ni and 20 wt.% Cr and had a diameter of 174 µm. Before the measurements, the SKP was calibrated with a Cu/Cu^{2+}-system [13].
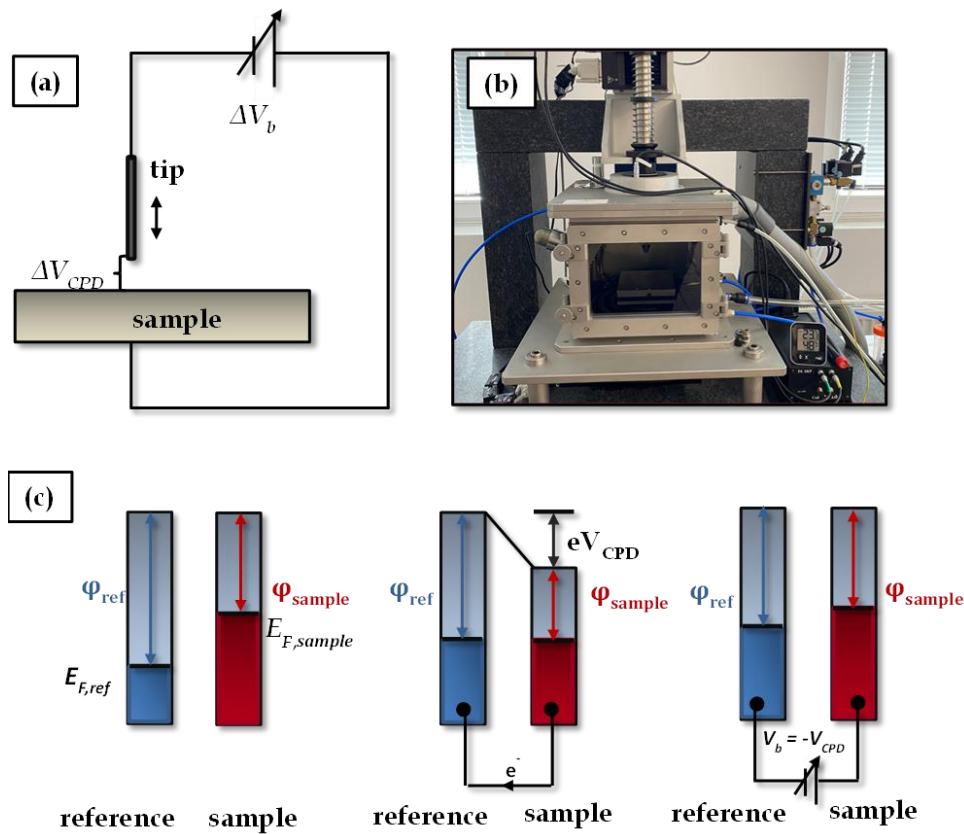
Figure 2.3: The set-up of a SKP technique (a) as well as a picture of the used SKP in the climate chamber (b). When the Kelvin probe, the reference electrode and a sample are brought into contact, the balance of the Fermi levels results in a Volta potential difference as a consequence of the correlated charge transfer. Applying an external bias voltage between the sample and the tip equalises the Volta potential difference and the two surfaces are no longer charged reproduced after [72,74].

Part II

Results and Discussion

Chapter 3

Water-uptake in hollow glass microspheres and their influence on cathodic and anodic delamination along the polymer/metal interface

This chapter is based on the article published under the same title in the journal Corrosion Science (see [13]) and reproduced under the corresponding copyright agreement. This study was conducted because water absorption can cause reactions at the adhesive/metal interface that can lead to degradation and failure of the bonded joint. Many publications therefore deal with water absorption in epoxy coatings and its effects on delamination processes at the interface. In contrast to previous publications, our study shows for the first time that EIS can be used to investigate commercially available adhesives with additives rather than simplified adhesive systems without additives. In this case, EIS enabled the estimation of water absorption in HGM, which are important lightweight fillers for structural adhesives. The results are in good agreement with standardised corrosion tests that were additionally carried out to investigate the influence of HGM on the corrosion resistance of epoxy adhesives.

Most of the experiments were carried out by the author herself. With the exception of the SEM images, which were carried out by voestalpine Stahl GmbH, and the corrosion tests, which were conducted with the assistance of Philipp Ricopuerto.

Water-uptake in hollow glass microspheres filled polymers, and in turn corrosion processes along the polymer/metal interface are not well studied to date. Here, we examine water absorption and diffusion of two epoxy adhesives in the absence and presence of HGM on zinc coated steel using electrochemical impedance spectroscopy and height-regulated scanning Kelvin probe. Mild filiform corrosion was detected on all epoxy adhesive coated Zn-Al-Mg (ZM) surfaces during cataplasma aging, suggesting anodic delamination as degradation mechanism. In contrast substantial cathodic delamination and blistering was observed for epoxy/electrogalvanized steel samples (ZE). Hence, HGM containing coatings can inverse effects on ZM or ZE coated steel, having important implications for industrial application.

3.1 Introduction

Given the increasing importance of lightweight construction and the deployment of multi material design in the automotive industry, adhesive bonding has become established as a joining process. Often used structural adhesives for automotive applications are epoxy adhesives [75–77]. Advantages of epoxy adhesives are a good chemical and heat resistance, excellent mechanical properties, high corrosion resistance, as well as strong adhesion [78–80]. However, epoxy resins are inherently brittle and have poor pressure resistance without additives [81,82].

One way to improve the properties of epoxy resins and to make the adhesive still suitable for lightweight construction is by adding HGM [83]. HGM are important lightweight fillers for polymers used in the aerospace industry, ship engineering and automotive industry [84,85]. For example, HGM fabricated foams are much stronger than other commonly used foams for building ships while maintaining the low weight. Properties which make HGM a key additive for the polymer industry are the controllable size and shape of the microspheres, the low density combined with the relatively high crack resistance, followed by the dielectric properties as well as the good thermal and acoustic insulation of the hollow glass beads [83].

Despite the improved properties due to the fillers, one known problem of adhesive bonding is that water absorption can generate reactions at the adhesive/metal interface, which can cause degradation and failure of the adhesive bond [75,86–89]. Considering the amount of research work published on the thermal, mechanical, and electrochemical properties of epoxy-HGM composites, little attention was placed on their influence on corrosion processes along the polymer/metal interface [81,90–94].

Therefore, the aim of this study was to determine the influence of HGM on the water uptake and the delamination process of two galvanized steel surfaces coated with epoxy adhesives as schematically shown in Fig. 3.1a-c and described in more detail in Chapter 3.2.3. EIS was used to determine the water uptake and the effective water diffusion coefficients of the coatings and HGM whereas corrosion tests allowed to identify the impact of HGM on the delamination process in structural adhesives. Finally, HR-SKP was used to confirm the delamination mechanism on both metal substrates.

3.2 Materials and Methods

3.2.1 Materials

For this study electrogalvanized steel and Zn-Al-Mg hot-dip galvanized steel were provided by voestalpine Stahl GmbH. The composition of the ZM coating was approximately 96 wt% Zn, 2.5 wt% Al and 1.5 wt% Mg ± 0.25 wt%. The average coating weight was 35 g/m² per side with a coating thickness of 5.5 μm and the steel substrate was CR4 mild steel with a thickness of 0.71 mm. ZE had an average coating weight on both sides of 100 g/m² Zn with a coating thickness of 7 μm. The substrate again was CR4 mild steel sheet with a thickness of 0.76 mm.

For the investigation of the water uptake, both substrates were coated with two different epoxy adhesives containing solid glass microspheres (SGM) or different amount of HGM from 3M technologies provided by Henkel AG & Co.

KGaA. The coating was applied by using a doctor blade. The first investigated adhesive was a MF containing D.E.R. 331 epoxy resin, dicyandiamide, and several additives like CaO as water scavenger, $CaCO_3$ as inert filler, polyurethane prepolymer flexibilizers, core-shell rubber tougheners and purple dioxazine pigments to simulate a commercially available adhesive. Tab. 3.1 illustrates the exact composition of MF. The second adhesive was a CF of which the exact composition is unknown. For HR-SKP measurements a further simplified adhesive formulation referred as Jeffamine formulation (JF), consisting of 37.8 wt% Jeffamine D400 and 62.2 wt% D.E.R. 331 P, was used to determine the interfacial delamination process.

Table 3.1: Detailed description of all concentrations and components used to prepare MF.

Substance name	wt (%)
D. E. R. 331 epoxy resin	40.00
DGEBA with core shell particles	10.00
Flexibilizers	10.00
CTBN modified epoxy resin	10.00
Hydrophobic silica	3.00
Dicyandiamide	5.60
Accelerator	0.35
$CaCO_3$	16.00
CaO	5.00
Dye, violet	0.05

3.2.2 SEM

Scanning electron microscopy, used to image the microstructure of HGM and the HGM charged CF coating, was performed on the Carl Zeiss AG-SUPRA 35 with an acceleration voltage of 15 kV or 5 kV.

3.2.3 EIS measurements

For sample preparation, ZE and ZM were ultrasonically cleaned with benzine and acetone. Afterwards, the cleaned metal surfaces were coated with neat MF

and CF, respectively. Additional MF coated ZE samples with different concentrations of HGM were prepared. Either 2 wt%, 4 wt%, 6 wt% HGM or 2 wt% SGM were added to the uncured MF adhesive and mixed using a Dual Asymmetric Centrifuge by SpeedMixer. After coating, the samples were cured at 180 °C for 0.5 h and the thickness of the adhesive coating was measured using a portable coating thickness gauge PHASCOPE PMP10 DUPLEX by Fisher. To obtain homogeneous coatings, a larger metal surface was coated than necessary for the EIS measurements, the thickness of the coating was measured with the portable coating thickness gauge and the samples were cut out into 45 x 45 mm² pieces where the coating had the desired homogeneity. The dry coating thickness d was 80 ± 35 µm for EIS measurements. Three parallel samples of each coating were prepared and measured to obtain a representative set of results.

For the EIS measurements, a three-electrode cell arrangement was used in which the coated sample acted as working electrode, a dimensionally stable anode was used as counter electrode and a Ag/AgCl (3 M KCl) electrode was used as reference electrode. The electrolyte for all measurements was a 3.5 wt% NaCl solution. Impedance measurements were carried out using a CompactStat by IVIUM technologies. Electrochemical impedance spectra were analysed with the software ZView and IVIUM soft. The measurements were carried out over a frequency range of 10^3-$10^{4.5}$ Hz using a 10 mV AC perturbation with respect to the OCP of the system at room temperature. The active electrode area was 12.5 cm² and the electrochemical cell which was placed on top of the working electrode was sealed with an O-ring. The water absorption of fully H_2O saturated coatings determined via EIS was compared with gravimetric measurements. Here, the MF coated samples mixed with 2 wt%, 4 wt% or 6 wt% HGM and the MF coated samples containing 2 wt% SGM were first weighed dry and after complete saturation of the coatings with water. Fig. 3.1a and c illustrate the coated sample including HGM and the equivalent circuit of epoxy coated metal surfaces. The SEM image in Fig. 3.1b shows the HGM charged CF coating. According to the manufacturer, the used HGM and SGM generally have a size distribution of 25-85 µm. In the equivalent circuit, R_s, R_p

and R_{ct} are the resistances of the electrolyte solution, the pore, and the charge transfer whereas CPE_c and CPE_{dl} are the constant phase elements of the coating and the double layer. Because of the non-ideal capacitance behaviours of the coating and the double layer, constant phase elements are used to fit the EIS spectra instead of capacitors. The impedance of CPE is described by Eq. (3.1) [94,95].

$$Z(j\omega) = (Y_0)^{-1} (j\omega)^{-n} \tag{3.1}$$

where Y_0 is the CPE constant, j the imaginary unit, ω the angular frequency and n represents the power of CPE. The CPE is a pure capacitor if n equals 1 and a pure resistor if n equals 0 [95].
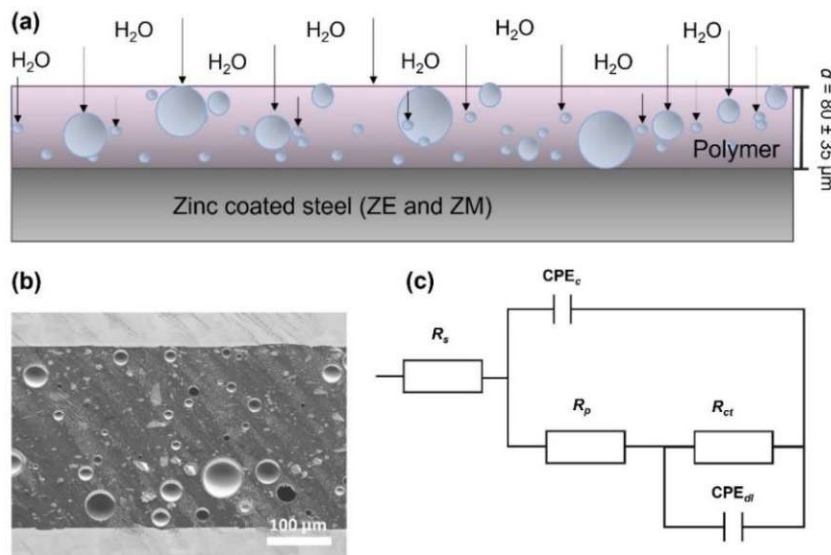
Figure 3.1: The diffusion of water in a MF-HGM coated steel surface after exposure to 3.5 wt% NaCl solution (a) including a SEM image of HGM charged CF (b) and an equivalent circuit of epoxy coated metal surfaces (c).

3.2.4 Determination of the water uptake and effective diffusion coefficient

The water uptake ϕ of a polymer coating on a metal surface can be calculated

using the Brasher-Kingsbury (B-K) equation, where C_t is the coating capacitance, C_0 is the initial coating capacitance and ε_{water} is the relative permittivity of water (80 at RT), Eq. (3.2) [86,96,97].

$$\phi = \frac{\log\left(\frac{C_t}{C_0}\right)}{\log(\varepsilon_{water})} \tag{3.2}$$

Since the capacitance of the polymer coating changes with water diffusion, this method is often referred to as the capacitance method. C_t is calculated according to Eq. (3.3) [97].

$$C_t = \frac{1}{2\pi f Z''} \tag{3.3}$$

where f is the frequency and Z'' is the imaginary part of the impedance at f.

Another used method to calculate the water uptake ϕ from EIS data is via linear relationship (LC), Eq. (3.4) [98].

$$\varepsilon_w = \varepsilon_c (1 - \phi) + \varepsilon_{water}\, \phi \tag{3.4}$$

where ε_w is the wet coating dielectric constant and ε_c is the dielectric constant of the dry coating. The wet coating dielectric constant ε_w can be calculated according to Eq. (3.5) [98].

$$\varepsilon_w = \frac{C_t d}{\varepsilon_0} \tag{3.5}$$

where d is the coating thickness and ε_0 is the vacuum permittivity.

The water uptake can be separated into two parts, whereas the water uptake at the initial first stage is fast and follows the Fick´s law as compared to the water uptake in the second part, which finally leads to a saturation of the polymer layer. If the possible swelling of the epoxy adhesives is ignored, Eq. (3.6) can be used to determine the effective water diffusion coefficient D_{eff} [86,95,99].

31

$$\frac{\ln C_t - \ln C_0}{\ln C_s - \ln C_0} = \frac{2 \sqrt{t}}{d \sqrt{\pi}} \sqrt{D_{eff}} \qquad (3.6)$$

where C_t is the capacitance of the time t , C_0 is the dry coating capacitance, C_s is the coating capacitance when the coating is saturated with water and d is the coating thickness [95].

3.2.5 Corrosion tests

Neutral salt spray tests according EN ISO 9227 as well as cataplasma tests according EN ISO 9142 were performed to determine the influence of HGM on the corrosion resistance of the epoxy adhesives. For all corrosion tests, ZE and ZM steel sheets were cut into 80 x 150 mm² pieces and ultrasonically cleaned with benzine and acetone. Afterwards, the sample surfaces were knife coated with MF containing 0 wt%, 2 wt%, 4 wt% or 6 wt% HGM as well as with CF. The adhesives were cured at 180 °C for 0.5 h. A 1 mm wide and 70 mm long defect was scratched with a Sikkens scratching tool through the polymer coating into the metal coating of each sample, subsequently. The edges and backside of each sample were covered with tape, to prohibit edge corrosion.

The salt spray tests were performed up to 480 h using a Q-FOG cyclic corrosion camber (Q-Lab) whereas the cataplasma tests were carried out up to 504 h with deionized H$_2$O at 70 °C in an oven. The area of interest was 40 x 70 mm² for all samples including the 70 mm long artificial defect in the middle of the shorter side. Afterwards, the delaminated area of each sample was removed via scalpel and its extension was determined by using the software ImageJ. Five parallel samples were measured per coating, for each metal substrate and each corrosion test. The dry coating thickness for the epoxy coated ZE and ZM samples were 140 ± 15 µm.

3.2.6 Determination of the interfacial delamination process via HR-SKP

SKP samples were prepared by ultrasonically cleaning ZM and ZE steel sheets with benzine and acetone. Afterwards, the JF coating was applied by knife

coating on both metal surfaces and cured at 120 °C for 1 h. The coated polymer-metal sheets were cut into 15 x 20 mm² pieces, subsequently. The resulting coating thickness was 90 ± 10 µm. Before the SKP measurements, an artificial defect was created by scratching the samples with a scalpel. Untreated wool threads were then positioned and fixed with tape within the defect. The prepared samples were stored in the humid climate chamber for at least 10 h to eliminate electrostatic charges. Afterwards, the delamination was initiated by soaking the wool threads with 0.5 M NaCl solution. Surface scans were carried out using a HR-SKP by Wicinski-Wicinski GbR. The used SKP tip consisted of 80 wt% Ni and 20 wt% Cr with a diameter of 174 µm. Prior the measurements, the SKP was calibrated using a Cu/Cu^{2+}- system. During all measurements, the relative humidity was set at 96 % and controlled with a feedback control loop connected to a humidity sensor inside the climate chamber. In order to accelerate the delamination process of the samples, the climate chamber was flushed with oxygen.

3.3   Results and Discussion

In this work, a commercial epoxy structural crash resistant adhesive, which is commonly used in the automotive industry, was compared with MF. By using MF, it was possible to draw clean structure-activity relationships of the adhesive´s compounds from measurement results. The commercial adhesive system was a CF which already contained HGM but had an unknown formulation whereas MF mixtures with and without HGM or solid glass microspheres were studied. EIS was used to determine the water uptake as well as the diffusion of water into the adhesives and HGM. Corrosion tests were performed with CF, MF and MF mixed with different amounts of HGM to determine the influence of HGM on the delamination process. Finally, the delamination process on both galvanized steel surfaces was confirmed using HR-SKP.

3.3.1 Water uptake behavior

To calculate the water absorption, it was necessary to determine the coating capacitance. Here, the coating capacitance was calculated according to Eq. 3.3 at a fixed frequency. The chosen frequency was 6.3 kHz for CF and MF coated ZE and ZM samples as well as for MF mixed with 2 wt% SGM or 2 wt% HGM coated ZE substrates, because the total impedance of the system in this high frequency domain was determined by the coating capacitance. For the MF mixed with 4 wt% HGM coated ZE sample, the chosen frequencies to calculate the coating capacitance were 6.3 kHz (0-80 h) and 10.0 kHz (90-140 h) while for MF mixed with 6 wt% HGM covered ZE, the frequencies were 6.3 kHz (0-50 h), 10 kHz (60 h), 15.9 kHz (70 h) and 20.0 kHz (80-140 h). All the chosen frequencies were in a frequency range, where the measured θ was close to   -90 degrees. The Bode plots of CF and MF coated ZE and ZM exposed to 3.5 wt% NaCl solution for 55 h at room temperature with the chosen frequencies marked with dotted lines to calculate the coating capacitance as well as the associated Nyquist plots are illustrated in Fig. A.1.1 and A.1.2. Fig. A.1.3 and A.1.4 describe the Bode and Nyquist plots of MF mixed with 2 wt% SGM, 2 wt% HGM, 4 wt% HGM and 6 wt% HGM covered ZE surfaces exposed to 3.5 wt% NaCl solution for 140 h at room temperature.

Fig. 3.2a and b illustrate water uptake curves of ZE and ZM, each coated with CF and MF determined via B-K approach. In order to remove the thickness effect of the epoxy coatings, all water uptake curves were plotted as a function of the reduced time $\tau = \sqrt{t} / d$ where t is the immersion time [100]. One major difference between CF and MF is the admixing of hollow glass beads to CF. Differences between both adhesives could be identified using EIS. At the beginning of the measurement, CF coated samples shown in Fig. 3.2a absorb water very fast into the coating, followed by a slow down until the first plateau is reached due to saturation of the coating with water. After the first plateau, water diffuses into the HGM and slows down after saturation of HGM with water is reached which marks the second plateau. In the next step, MF was used where HGM were left out to examine the impact of HGM in adhesives on the

34

water absorption behavior. Comparing the water uptake curves of CF coated samples with the water uptake curves of MF coated samples shown in Fig. 3.2b, one plateau was detected instead of two plateaus as seen in Fig. 3.2a which indicated, that the additional water uptake is caused by HGM in CF. Further, the water uptake in CF coatings is lower than in MF coatings as seen in the first plateau, because additives were left out in MF. No significant differences between the water uptake of ZM and ZE could be detected.
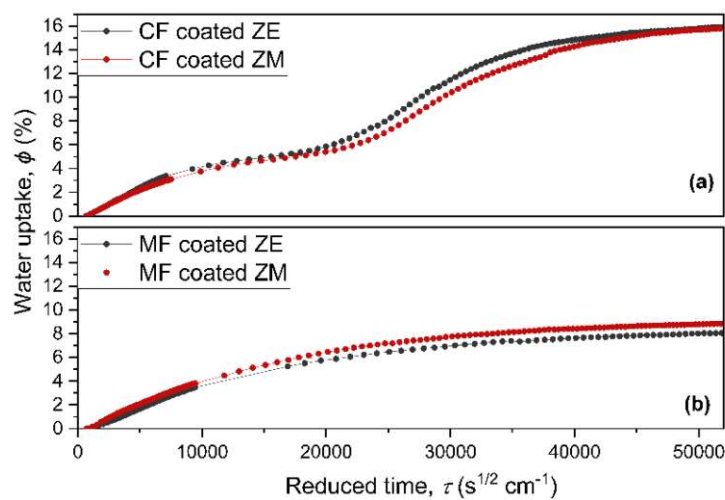
Figure 3.2: Water uptake curves of CF (a) and MF (b) coated ZE and ZM exposed to 3.5 wt% NaCl solution for 55 h at room temperature.

SEM images of pure HGM at magnifications of 200, 500 and 2000 are shown in Fig. 3.3a-c. The SEM images show that some of the HGM were broken and that HGM had a general size distribution of 25-85 μm. Depending on the proportion of broken glass spheres in the adhesive, the water absorption and diffusion may vary slightly. Therefore, each coating was measured at least three times
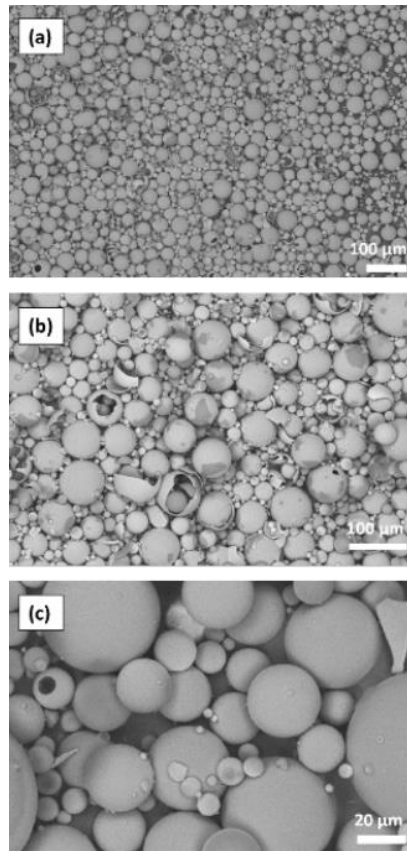
Figure 3.3: SEM images of pure HGM at different magnifications of 200 (a), 500 (b) and 2000 (c).

It is now interesting to understand if an interaction between the glass surface and the adhesive is responsible for the further water uptake. In order to prove that the water uptake is caused by water diffusing inside the hollow glass microspheres, EIS reference measurements with solid glass microspheres were done. As shown in Fig. 3.4, no second plateau could be detected in coatings with 2 wt% SGM compared to coatings with 2 wt% HGM where a second plateau was observed. Therefore, the possibility that interfacial processes between the glass surface and the adhesive caused the additional water absorption can be ruled out and that the water actually diffuses into the inside of HGM. More water is absorbed into the adhesive with SGM compared to MF coated samples without glass beads. The higher water absorption can be explained by the more defect-rich coating, which is created by mixing SGM in

36

the uncured MF [101].
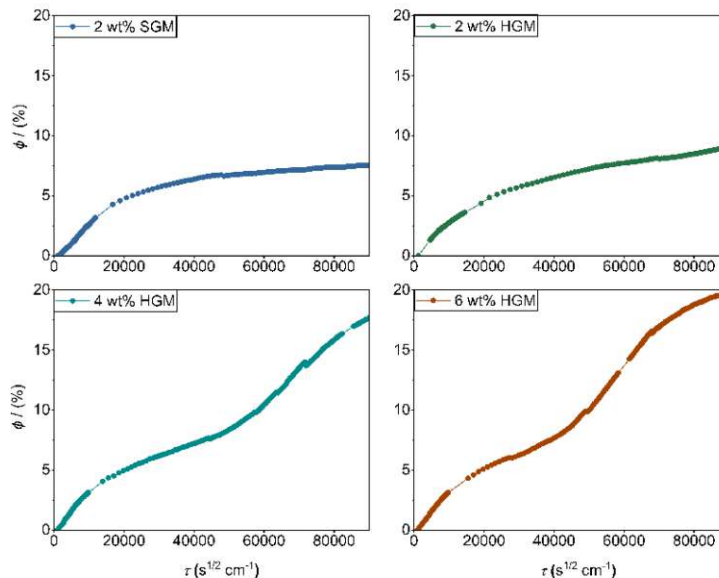
Figure 3.4: Comparison of the water uptake curves of ZE coated with MF mixed with 2 wt% SGM, 2 wt% HGM, 4 wt% HGM and 6 wt% HGM exposed to 3.5 wt% NaCl solution for 140 h at room temperature.

Hence and shown in Fig. 3. 4, the water uptake behavior of MF mixed with different concentrations of HGM was investigated. Generally, the results show a similar two-step water absorption as seen in the water uptake curves of CF coated ZE or ZM samples illustrated in Fig. 3.2b. Moreover, the second saturation is more pronounced with higher concentrations of HGM. This result indicates that water diffuses inside the hollow glass beads. Accordingly, the second plateau of the curve is due to fully saturation of the hollow glass spheres with water. All values for the water uptake in MF, CF and HGM calculated according to B-K are listed in Tab. 3.2. Furthermore, it is noticeable that for all mixtures the adhesive MF absorbs a similar amount of water of about 6-8 vol% until the first plateau of the curve is reached regardless the amount of HGM. However, the additional water uptake by HGM between the first plateau and the second plateau increases with increasing content of HGM. Plotting the

37

additional water uptake against the concentration of HGM resulted in a linear relation given in Fig. 3.5. Consequently, this relation allowed to estimate the amount of HGM in CF which was calculated to be 4.6-4.7 wt% and which is illustrated in Fig. 3.5 as a blue triangle.

Table 3.2: Water uptake in MF, CF and HGM calculated according to B-K as well as effective water diffusion coefficient measured via EIS.

Sample	wt_{HGM} (%)	wt_{SGM} (%)	$\phi_{H_2O\ in\ adhesive}$ (%)	$\phi_{H_2O\ in\ HGM}$ (%)	$D_{eff,\ H_2O\ in\ adhesive}$ (m² s⁻¹)	$D_{eff,\ H_2O\ in\ HGM}$ (m² s⁻¹)
MF coated ZE	-	2	7.2 ± 0.3	-	4.32x10⁻¹³ ± 6.83x10⁻¹⁴	-
MF coated ZE	2	-	7.2 ± 0.3	3.9 ± 0.4	1.18x10⁻¹³ ± 4.03x10⁻¹⁴	1.64x10⁻¹⁴ ± 7.08x10⁻¹⁵
MF coated ZE	4	-	7.9 ± 0.3	9.8 ± 0.7	1.77x10⁻¹³ ± 3.65x10⁻¹⁴	2.54x10⁻¹⁴ ± 1.20x10⁻¹⁴
MF coated ZE	6	-	5.9 ± 0.6	13.4 ± 0.7	2.27x10⁻¹³ ± 4.95x10⁻¹⁴	8.43x10⁻¹⁴ ± 2.40x10⁻¹⁴
MF coated ZE	-	-	5.6 ± 2.1	-	2.09x10⁻¹³ ± 8.35x10⁻¹⁴	-
MF coated ZM	-	-	6.4 ± 2.3	-	4.60x10⁻¹³ ± 1.39x10⁻¹³	-
CF coated ZE	4.7	-	4.4 ± 0.3	10.6 ± 0.2	9.27x10⁻¹³ ± 3.30x10⁻¹³	2.99x10⁻¹³ ± 1.86x10⁻¹³
CF coated ZM	4.6	-	3.1 ± 1.3	10.5 ± 1.3	4.53x10⁻¹³ ± 7.59x10⁻¹⁵	5.87x10⁻¹⁴ ± 5.70x10⁻¹⁴
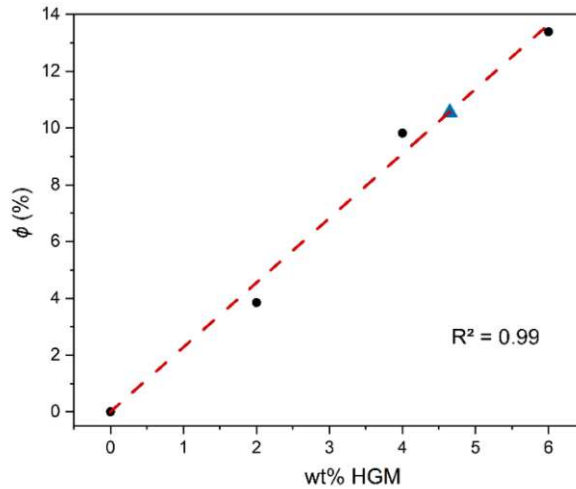
Figure 3.5: Linear relation between the concentration of HGM and the additional water uptake by HGM where the blue data point marks the calculated weight percentage of HMG in CF.

The effective diffusion coefficients of water into the epoxy adhesives determined according to Eq. (3.6) are listed in Tab. 3.2 and are comparable to values found in literature [11,102,103].The effective diffusion coefficient of water in HGM is approximately 3-8 times smaller than the diffusion coefficient of water into the adhesive. Fig. 3.6 illustrates the $\log C_t$-$t^{1/2}$ curves of HGM containing MF coatings on ZE substrates for the determination of the effective diffusion coefficients of water in the adhesives as well as in HGM. The red lines show the linear range fitted to calculate the diffusion coefficients of water into the adhesive or into HGM. It is noticeable that the slopes of the curves are the same for the transport of water into the adhesive, whereas the slopes for the investigation of diffusion in HGM increase with increasing HGM concentration. The diffusion coefficient of water in the adhesive rises with increasing addition of HGM although the slopes are the same for all three curves, which is related to the more defect-rich coating that occurs when glass spheres are mixed into the adhesive as discussed earlier. The lower the proportion of HGM in the coating, the longer it takes for the adhesive to become completely saturated and for the diffusion of the water into HGM to begin, since the quantity of the adhesive in the coating is higher, consequently. The effective diffusion coefficient of water in HGM increases with increasing amounts of HGM, which

can be explained by the larger surface area of glass in the adhesive.
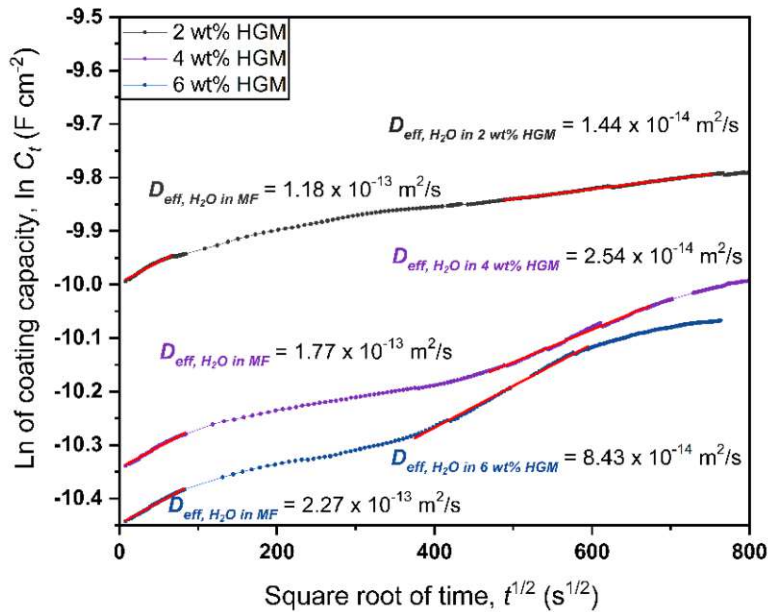
Figure 3.6: The curves $\log C_t$-$t^{1/2}$ of MF mixed with 2 wt%, 4 wt% and 6 wt% HGM covered ZE to determine the effective water diffusion coefficient in MF and HGM.

Tab. 3.3 compares total water uptake values determined gravimetrically and via EIS, for ZE coated with MF containing different amount of glass microspheres. The calculation of the absorbed mass of water using EIS was done by B-K (3.2) and LC (3.4). Values obtained by B-K formula greatly exceeded the gravimetric results. The deviation from gravimetric values reached up to more than 90 %. In contrast, the water uptake values calculated via LC were mainly lower compared to gravimetric ones, with deviations of up to approximately 40 %. Therefore, LC approximated better with gravimetric values than B-K, but the water uptake was usually a bit underestimated. The comparison of the two calculation methods showed that LC is better suited to determine the water uptake in coatings measured via EIS. Similar results are shown in the studies of Nguyen et al. [98].

Table 3.3: Comparison of the total water uptake determined gravimetrically, B-K and LC as well as the deviation of the two calculation methods with that of the gravimetric method.

wt_{HGM} (%)	wts_{GM} (%)	$m_{grav.}$ (mg)	m_{B-K} (mg)	m_{LC} (mg)	$\Delta m_{B-K \, vs \, grav.}$ (%)	$\Delta m_{LC \, vs \, grav.}$ (%)
-	2	5.7 ± 0.5	10.9 ± 1.1	3.6 ± 0.4	+ 91.2	- 36.8
2	-	4.0 ± 0.8	7.1 ± 1.2	2.5 ± 0.5	+ 77.5	- 37.5
4	-	8.7 ± 2.8	15.7 ± 2.9	5.9 ± 1.5	+ 80.5	- 32.2
6	-	7.7 ± 0.5	14.9 ± 0.9	8.3 ± 1.2	+ 93.5	+ 7.8

3.3.2 Influence of HGM in the adhesive on cathodic and anodic delamination

Neutral salt spray (NSS) tests based on EN ISO 9227 as well as cataplasma tests based on EN ISO 9142 were chosen as corrosion tests to evaluate the influence of coatings with different amount of HGM on the interfacial delamination process of ZE and ZM surfaces. Although the same coatings were used for the corrosion tests, two different delamination processes could be detected on ZE and ZM surfaces. This result shows that the different composition of the two zinc layers had a great influence on the delamination behaviour of the adhesive during cataplasma aging, as shown in Figure 3.7a-d. Fig. 3.7a and b show the optical images of two MF coated ZM samples without any glass microspheres and with 6 wt% HGM, where filiform corrosion took place during the cataplasma test. Filiform corrosion is more pronounced in coatings without any HGM than with additional hollow microspheres. The filament consists of an active head and an inactive tail. In general, it is assumed to occur at or near the front of the head whereas the oxygen reduction reaction mainly takes place at the back of the head. Diffusion of oxygen along the tail area, creates different aeration between the head and the tail which moves the head of the filament forward [47,104,105]. Filiform corrosion is a form of anodic delamination and ZM is known to inhibit cathodic delamination, because anodic dissolution from

Mg-rich phases, especially from intermetallic $MgZn_2$ present on the ZM surface, releases Mg^{2+} and forms $Mg(OH)_2$ with cathodically produced OH^-, which buffers the interfacial pH to slightly alkaline values. Therefore, the production of more soluble zinc oxide compounds is hindered and stable zinc compounds like simonkolleite are formed. The mildly alkaline pH values also initiate the anodic dissolution of aluminates from Al-rich phases, which react with Mg^{2+} to form stable layered double hydroxides (LDH). Therefore, the stabilization of the passive layer due to the presence of LDH and protective zinc compounds reduces the cathodic oxygen reduction reaction which would lead to cathodic delamination [48,49,106–109].

In contrast to Fig. 3.7a and b, no filiform corrosion was observed on epoxy coated ZE surfaces as illustrated in Fig. 3.7c and d. Instead of filiform corrosion, blistering took place on all adhesive coated ZE surfaces during the cataplasma test regardless if glass microspheres were added to the coating before curing or not. Blistering is often found on organic polymer coated metal surfaces which preferentially undergo cathodic delamination as seen on epoxy coated ZE surfaces in this study. One reason for blister initiation is the presence of small defects and pores in the coating [110–114]. Comparing the blistering of MF coated ZE without HGM with the blistering of MF coated ZE metal containing 6 wt% HGM, the number of blisters increased with higher concentrations of hollow microspheres in the adhesive. Hence, the increase of blistering can be explained by the more defect-rich coating due the addition of glass microspheres.
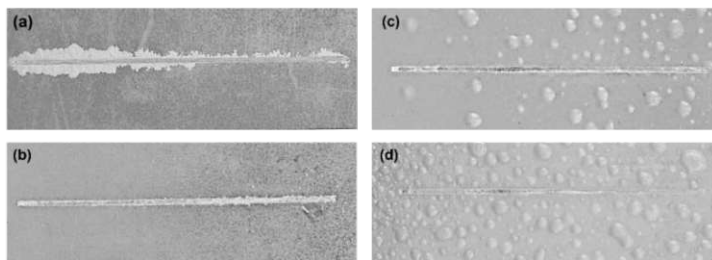
Figure 3.7: Optical images of filiform corrosion on MF coated ZM with 0 wt% HGM (a), 6 wt% HGM (b) as well as blistering on MF coated ZE containing 0 wt% HGM (c) and 6 wt% HGM (d) after the cataplasma test.

Fig. 3.8 summarizes the results obtained from both corrosion tests. Plotted are the percentage of the delaminated and intact area against the differently coated ZE and ZM samples with different concentrations of HGM. On the left the results of the salt spray test are shown and on the right side the results of the cataplasma test. The green bars represent the intact area, while the red bars represent the delaminated area. All tested samples, except CF coated ZM, have a similar area fraction of around 13-16 % which delaminated during the salt spray corrosion test. Therefore, HGM do not seem to influence the delamination process of the coated ZM and ZE samples during NSS. As already mentioned, an exception was the CF coated ZM surface, which was more stable against delamination and only had a delaminated area fraction of 1 %. ZM is known to have lower corrosion rates due to the addition of a certain amount of magnesium in the alloy [115–117]. CF contains additional unidentified additives, which are not included in MF, and which causes the CF coating to be more resistant against anodic delamination. The reason is not yet fully elucidated and will be investigated in future studies.

In contrast to the results of the salt spray test, in the cataplasma test, the size of the delaminated areas differs significantly depending on the metal substrate. The delamination of the adhesive is more pronounced on the ZE surfaces where cathodic delamination occurs. The five parallel samples from each coating differ strongly, which is visible in the large standard deviation. As discussed above, blistering was observed during the cataplasma test in addition to cathodic delamination. Depending on the location where the blistering occurs, differences in the size of the delaminated area were detected, because the size of the delaminated area increased with blisters closer to the artificial defect. For this reason, the delaminated area caused only by cathodic delamination as well as the influence of the hollow glass spheres on the cathodic delamination during cataplasma aging of the adhesive coated ZE samples could not be determined. Considering the delaminated areas of the coated ZM surfaces after cataplasma aging, it can be observed that the delaminated areas of all coated ZM surfaces containing up to 4 wt% HGM show a comparable delaminated

area fraction of 1.6-2.0 %. By adding 6 wt% HGM to MF, the delaminated area is only 0.7 % which leads to the assumption that a higher content of HGM improves the resistance against filiform corrosion during cataplasma aging. Bahrami et al. found out that HGM in a coating can create a physical barrier against the corrosive electrolyte, which increases the corrosion protection of the coating [94]. Results from the cataplasma test showed that HGM can significantly decrease delamination under anodic conditions, while HGM increase cathodic delamination rates and trigger blistering. The reason for the lower delamination under anodic conditions could be that HGMs act as water traps that slow down the delamination process. However, in the case of the epoxy coated ZE surfaces, where cathodic delamination is assumed to be the dominant delamination process, it was found that the number of blisters formed by the hollow glass beads increased significantly during the cataplasma test. As mentioned earlier, the reason for this is that the hollow glass microspheres cause more defects in the coating where cathodic oxygen reduction and anodic metal dissolution can occur, leading to blistering.
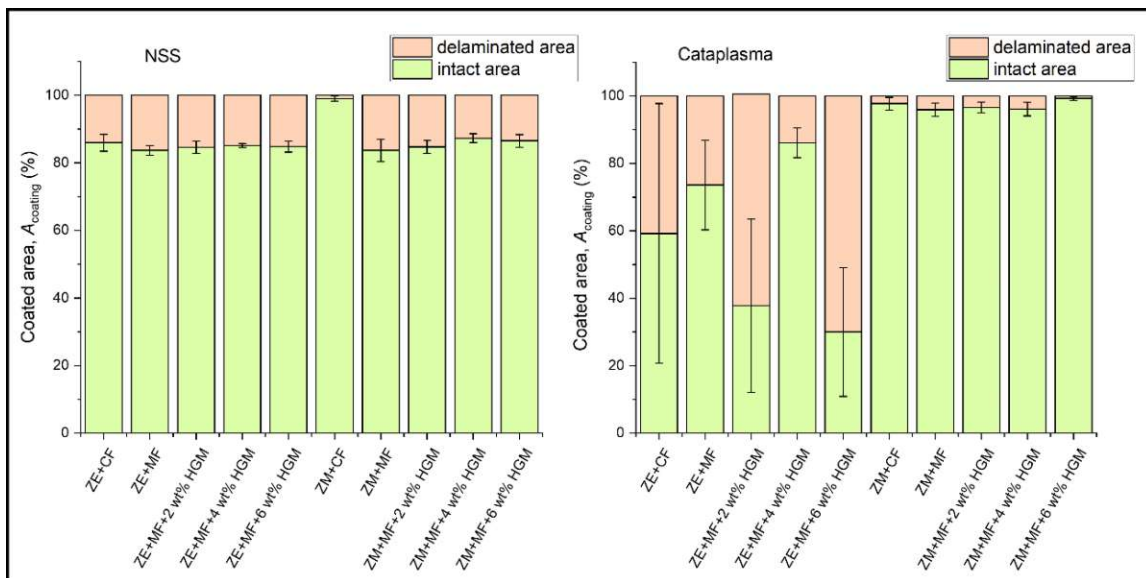
Figure 3.8: Percentage of the intact area (green) to the delaminated area (red) after 480 h in the NSS and 504 h in the cataplasma test.

3.3.3 Determination of the interfacial delamination process on epoxy coated ZE and ZM surfaces

In order to further confirm the delamination process another more simplified model formulation was used which only consisted of the hardener Jeffamine D400 and the epoxy resin D.E.R. 331P. Fig. 3.9a and b demonstrate the potential profiles of JF coated ZE and ZM samples in humid oxygen flushed atmosphere at 25 °C after 0.5 M NaCl was added to the artificial defect, obtained by HR-SKP measurements. SKP line scans at a fix position were chosen out of an area scan to ensure that no additional defects within the zinc coating disturb the delamination process. SKP line scans at different exposure times with 0.5 M NaCl electrolyte were plotted against the distance $x\text{-}x_0$ away from the artificial defect, subsequently. The JF coated ZE in Fig. 3.9a was exposed to 0.5 M NaCl for up to 22 h whereas the exposure time of JF coated ZM shown in Fig. 3.9b was up to 200 h. The potential profile in Fig. 3.9a shows characteristics of cathodic delamination which can be divided into three parts. The first part is the defect where oxidation of the metal takes place and is defined as local anode. It is followed by the delamination front, which is marked as an inflection point in the potential profile and which shifts further to longer distances as the exposure time progresses. At the delamination front, which is the local cathode, oxygen is reduced to hydroxide ions and the pH value rises. Due to an excess of negative charge under the coating, hydrated sodium ions migrate, leading to a galvanic coupling between local anode and local cathode. Plotting the shift of the inflection point against the square root of time allows to determine the diffusion coefficient of the hydrated cations [118–120]. Therefore, the diffusion of hydrated Na$^+$-ions along the buried JF-ZE interface was estimated to be 8.4 x 10^{-10} m^2 s^{-1}, which is in good agreement with values found in literature [121]. Near the defect, the potential is around -0.45 V, as a result of metal dissolution within the defect and increases with expanding distance from the defect. In literature the same effect was found and explained by an ohmic potential drop, which occurs because of the ionic current at the delaminated interface [122]. Leng et al. reported that the highly anodic shifted potential of the intact

polymer/metal interface is due to the absence of anodic current which occurs if metal dissolution was not inhibited and the oxygen reduction reaction was not reduced [119,122].

Comparing, the SKP line scans of JF coated ZE with the line scans of the ZM surface with the same adhesive in Fig. 3.9b, no cathodic potential shift next to the defect due to cathodic delamination was detected, although the exposure time of 0.5 M NaCl was nearly 10 times longer with up to 200 h. The intact polymer/metal region has lower potential values than the region next to the defect, which indicates that an inversion of the local anode and local cathode was observed compared to the ZE surface where cathodic delamination was identified as the interfacial delamination process. As mentioned above, it is known that ZM preferentially undergoes anodic delamination, because Mg-rich phases dissolve anodically, releasing Mg^{2+} and buffering the interfacial pH to slightly alkaline pH values through the formation of $Mg(OH)_2$ with the cathodically produced OH^-. This hinders the formation of more soluble zinc species, leading to the formation of stable zinc compounds. Furthermore, the mildly alkaline pH values can cause the release of aluminates from Al-rich phases, leading to the formation of LDH with the previously formed Mg^{2+}. The presence of LDH and the stable zinc compounds stabilize the passive layer, which impedes the cathodic oxygen reduction reaction that would lead to cathodic delamination [48,49,106–109].
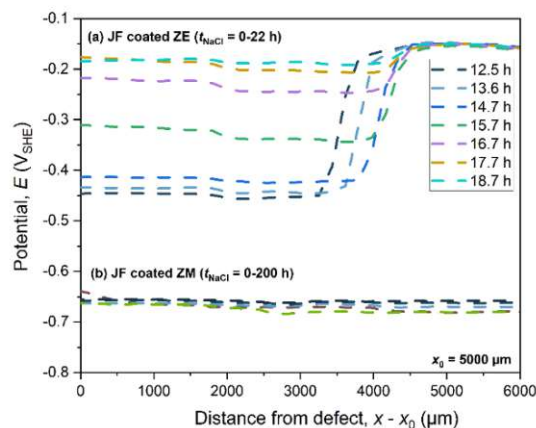
Figure 3.9: Potential profiles of JF coated ZE (a) and ZM (b) in humid atmosphere with increased oxygen concentration at 25 °C after adding 0.5 M NaCl to the artificial defect.

3.4 Conclusion

The different water absorption behavior of CF and MF could be explained by admixing different amounts of HGM to MF. Water diffused first into the adhesive, and after saturation of the adhesive with water, diffused into HGM. Evidence that HGM absorbs water could be shown, because with increasing amounts of HGM the water absorption increases. Subsequently, CF contains 4.6-4.7 wt% HGM, which was calculated through the linear relation between the additional water uptake by HGM and the concentration of HGM. EIS measurements allowed to estimate the effective diffusion coefficients of water into CF, MF and HGM. Additionally, the calculation of the water uptake via LC equation showed less deviation from the gravimetric determined total water uptake than using B-K equation. Corrosion test showed that during the NSS, no influence of the HGM on the delamination process could be found. In contrast, during the cataplasma aging, cathodic delamination and blistering took place on the coated ZE substrates and filiform corrosion could be detected on coated ZM samples. HGM increased blistering during cataplasma aging on coated ZE surfaces due to the more defect-rich coating. Concentrations above 6 wt% HGM seem to improve the resistance against anodic delamination on coated ZM samples during the cataplasma test and comprise less delaminated area. HR-SKP measurements allowed to confirm that coated ZE samples preferentially undergo cathodic delamination while coated ZM surfaces tend to undergo anodic delamination which was also seen during the corrosion tests. In summary, HGM in coatings are good for ZM which preferentially delaminates anodically whereas HGM triggers blistering and increases the delamination rate on cathodic delaminated samples as seen on coated ZE surfaces.

Chapter 4

Systematic variation of inorganic additives and their impact on interfacial delamination processes of automotive coating systems

The following chapter is based on the article published under the same title in Progress in Organic Coatings (see [123]) and reproduced under the corresponding copyright agreement. This study was performed since inorganic fillers in adhesives for the automotive industry allow both functional and mechanical adjustment of the adhesive properties. Although the integral effects of additives are well known, the individual effects of each component and how they can lead to synergistic and antagonistic effects are less well studied. Therefore, we systematically vary calcium oxide (CaO), calcium carbonate ($CaCO_3$) and hydrophobic fumed silica (SiO_2) to understand individual and combined effects. For example, our study allowed to determine the origin of blistering on ZE surfaces and the delamination process on ZM surfaces, as well as the influence of the inorganic components in the adhesive on the delamination resistance by performing cataplasm tests in several environments.

The majority of the experiments were carried out by the author herself. With the exception of the SEM images, which were carried out by voestalpine Stahl GmbH, and the cataplasma tests, which were conducted with the help of Philipp Ricopuerto.

49

Inorganic fillers incorporated in adhesives for the automotive industry enable both functional and mechanical tuning of adhesive properties. While integral effects of additives are well understood, the individual effects of single components and how they may lead to synergies as well as antagonistic effects remain unclear. Here, we systematically vary the concentration of CaO, $CaCO_3$ and hydrophobic fumed SiO_2 to understand individual and combined effects. For this purpose, the inorganic additives were mixed into a model formulation without inorganic additives and compared with a close to real application one-component epoxy adhesive, which also contained these fillers. The water uptake of the filled adhesives was measured with EIS and the results were compared with findings from cataplasma tests under atmospheric conditions. These results indicated that hydrophobic SiO_2 can result in accelerated water uptake, although the opposite would be expected due to the more hydrophobic surface coating. In addition, blistering was observed on all galvanized surfaces, while filiform corrosion was observed on all hot-dip galvanized Zn-Al-Mg steels. Cataplasma tests in oxygen-depleted and oxygen-rich atmospheres allowed to identify interfacial delamination processes. Our results showed that CaO can cause osmotic blistering and accelerate the diffusion of water into the adhesive due to a local increase in pH near the hydrated CaO particles, while $CaCO_3$ reduces water diffusion. However, coating defects may occur due to the addition of $CaCO_3$, leading to increased cathodic blistering. A strategy for improving beneficial and synergistic effects is discussed.

4.1   Introduction

Adhesive bonding established as a central joining process in the automotive industry due to the increasing importance of lightweight construction and the use of multi-material designs [75–77]. However, water can have a detrimental effect on adhesives, as it easily diffuses into the adhesive and causes damage at the interface between the adhesive and the adherend [13,124]. Typical mechanisms for adhesive displacement are hydrolysis and bond breakage at the interface [125]. Another well-known form of failure in structural adhesives is blister formation [126,127]. Here,

the diffused water is assumed to condense in micropores, especially at the polymer/metal interface, leading to partial dissolution of the adhesive, e.g. inorganic fillers, at the interface and creating an osmotic pressure leading to osmotically induced blistering [128,129]. In contrast, to osmosis, being primarily responsible for blistering, Leng, Streckl, and Stratmann argued that cathodic delamination is the main cause of blistering [130].

Since the use of inorganic fillers is common practice to adjust adhesive properties and reduce costs, understanding their influence on delamination processes such as osmotically induced blistering, cathodic and anodic delamination is crucial. CaO, for example, has a very reactive surface that forms $CaCO_3$ with atmospheric CO_2 and calcium hydroxide ($Ca(OH)_2$) with H_2O. For this reason, CaO serves as a water scavenger in polymers such as epoxy adhesives [131,132]. On the other hand, $CaCO_3$ is added to adhesives as an inert filler. A major advantage of this inorganic filler is its capability to improve the hardness, scratch resistance and thermal stability of epoxy coatings. Moreover, $CaCO_3$ improves the toughness and wear resistance of epoxy adhesives and composites [133–136]. Another benefit of adding inert additives such as $CaCO_3$ to adhesives is that these fillers can physically prevent the penetration of water into the adhesive and thus provide better delamination resistance [137,138]. A further frequently used inorganic additive in the adhesives industry is fumed silica, which is used to improve rheological properties, for example to achieve stable thickening and thixotropy of epoxy and polyurethane adhesives [139,140]. The hydrophilic surface of fumed silica can be modified with organic trimethylsiloxyl groups making it hydrophobic. If hydrophobic fumed SiO_2 is then used as an additive, the resulting film is expected to be both water and moisture repellent, with enhanced hardness and strength [141,142].

Since it is now known that inorganic components in adhesives can partially dissolve due to water absorption and lead to increased blistering, the aim of this study is to comprehensively investigate the water absorption behaviour of commonly used inorganic additives in the adhesive industry and their influence on the delamination process. For this purpose, inorganic additives CaO, $CaCO_3$ and hydrophobic fumed SiO_2 were individually mixed into model formulations without inorganic additives

(MF_{without inorganic additives}) and compared with a close to application one-component epoxy adhesive, which contained all inorganic additives, similar to 1K epoxy structural adhesives for automotive body-in-white (BIW) application. Furthermore, two metal substrates were used, where it was shown in a previous study that epoxy adhesive coated electrogalvanized steel (ZE) preferentially undergoes cathodic delamination, while epoxy adhesive coated hot-dip galvanized Zn-Al-Mg steel is prone to undergo anodic delamination [13]. EIS measurements were carried out to determine the water uptake and diffusion of water in all adhesive formulations. Finally, cataplasma tests were conducted in oxygen-depleted, atmospheric, and oxygen-rich environments to identify the mechanism of coating blistering on ZE surfaces and to confirm the delamination process on coated ZM surfaces, as well as the delamination resistance of the structural adhesives filled with CaO and CaCO$_3$.

4.2 Materials and Methods

4.2.1 Materials

Electrogalvanized steel and hot-dip galvanized Zn-Al-Mg steel were provided by voestalpine Stahl GmbH for performing this study. ZE samples consisted of a 0.76 mm thick CR4 mild steel sheet and a 7 μm thick Zn coating with an average coating weight of 100 g/m² on both sides. The composition of the ZM coating was about 96 wt% Zn, 2.5 wt% Al and 1.5 wt% Mg ± 0.25 wt% with an average coating weight of 70 g/m² on both sides. The ZM coating had a coating thickness of 5.5 μm, while the steel substrate, also a CR4 mild steel, had a thickness of 0.71 mm. The thickness of the zinc layer of ZM is 1.5 μm thinner than that of ZE, as industrial samples were used for this study.

For the water absorption study, ZE substrates were coated with close to reality one-component (1K) epoxy adhesive containing CaO as water scavenger, CaCO$_3$ as inert filler and hydrophobic fumed SiO$_2$ as rheological additive (MF), which was used in a previous study [13], and a model formulation (MF_{without inorganic additives}) free from inorganic additives. Our previous study also showed that the water absorption of the adhesive is almost identical regardless of

whether the adhesive is applied on the ZE or ZM surface. Therefore, the EIS measurements were only carried out on the ZE substrate [13]. The coating was applied by using a doctor blade. Besides the inorganic additives, the epoxy adhesives contained D.E.R. 331 epoxy resin, dicyandiamine as curing agent and several additional additives like polyurethane prepolymer flexibilizers, core shell rubber tougheners, an accelerator and purple dioxazine pigments. Both model formulations were provided by Henkel AG & Co. KGaA and the exact compositions are shown in Table 4.1. In order to investigate the influence of inorganic additives on the water-uptake of the adhesive and on the delamination process, Henkel AG & Co. KGaA also provided CaO, $CaCO_3$ and hydrophobic fumed SiO_2 from Teroson, which were mixed in different concentrations into $MF_{without\ inorganic\ additives}$.

Table 4.1: A detailed description of all concentrations and components used to prepare MF and $MF_{without\ inorganic\ additives}$.

Substance name	wt_{MF} (%)	$wt_{MF_{without\ inorganic\ additives}}$ (%)
D.E.R. 331 epoxy resin	40.00	50.00
DGEBA with core shell particles	10.00	13.00
Flexibilizers	10.00	13.00
CTBN modified epoxy resin	10.00	13.00
Hydrophobic fumed silica	3.00	-
Dicyandiamide	5.60	7.50
Accelerator	0.35	0.46
$CaCO_3$	16.00	-
CaO	5.00	-
Dye, violet	0.05	0.07

4.2.2 SEM

Scanning electron microscopy, used to image the microstructure of MF coated on ZE and ZM surfaces, was performed on Carl Zeiss AG-SUPRA 35 with an acceleration voltage of 5 kV.

4.2.3 Electrochemical impedance spectroscopy

For the sample preparation, ZE was ultrasonically cleaned with benzine and

acetone. Subsequently, the cleaned metal surfaces were coated with neat MF or MF$_{\text{without inorganic additives}}$. In addition, MF$_{\text{without inorganic additives}}$ coated ZE samples were prepared with different amounts of CaO, CaCO$_3$ and hydrophobic fumed SiO$_2$. For this purpose, either 5 wt% CaO, 10 wt% CaO, 16 wt% CaCO$_3$, 32 wt% CaCO$_3$, 3 wt% SiO$_2$ or 6 wt% SiO$_2$ were added to the uncured MF$_{\text{without inorganic additives}}$ and mixed using a dual asymmetric centrifuge of the SpeedMixer. After coating, the samples were cured at 180 °C for 0.5 h and the thickness of the adhesive layer was measured using a Fisher PHASCOPE PMP10 DUPLEX portable coating thickness gauge. In order to prepare homogeneous coatings, a larger metal surface area than required for the EIS measurements was coated. Afterwards, the thickness of the coating was measured with the portable coating thickness gauge and the samples were cut into 45 x 45 mm^2 pieces where the coating exhibited the desired homogeneity. The dry film thickness d was 95 ± 30 μm for the EIS measurements. Here, Fig. 4.1a and b illustrate SEM images of the MF coated ZE and ZM samples, where the filler CaO and CaCO$_3$ in the adhesive are displayed as well as the microstructure of the different zinc coatings on ZE and ZM substrates. At least, three parallel samples of each coating were measured to obtain a representative set of results.

A three-electrode cell arrangement was used for the EIS measurements with the coated sample as the working electrode, a dimensionally stable anode as the counter electrode and an Ag/AgCl (3 M KCl) electrode as the reference electrode. The electrolyte for all measurements was a 3.5 wt% NaCl solution. The measurements were conducted using a CompactStat from IVIUM technologies. The spectra were analyzed using ZView and IVIUM soft software. Measurements were performed in a frequency range of 10^3-$10^{4.5}$ Hz using an AC perturbation of 10 mV with respect to the open circuit potential of the system at room temperature. The small frequency range was chosen because the water uptake into the coating is very fast at the beginning and follows Fick's law, it is necessary to record the impedance spectra in very short intervals to obtain the water absorption curves. The active electrode area was 12.5 cm^2 and the electrochemical cell mounted on the working electrode was sealed with an O-ring. Fig. 4.1c and d show a schematic of the setup for measuring the water

absorption of organic coatings on metal substrates via EIS and an equivalent circuit suitable for describing epoxy-coated metal surfaces. In the equivalent circuit, R_s, R_p and R_{ct} are the electrolyte solution, pore and charge transfer resistances, respectively, while CPE_c and CPE_{dl} are the constant phase elements of the coating and double layer. Due to the non-ideal capacitance behavior of the coating and double layer, constant phase elements are used instead of capacitors in this equivalent circuit. The impedance of CPE is given by Eq. (4.1) [94,95].

$$Z(j\omega) = (Y_0)^{-1}\,(j\omega)^{-n} \tag{4.1}$$

where Y_0 represents the CPE constant, j the imaginary unit, ω the angular frequency and n the power of CPE. The CPE is a pure capacitor if n equals 1 and a pure resistor if n equals 0 [95].

The calculation of the water uptake ϕ from the resulting EIS data using the linear combination method has been applied in previous studies and is described in detail elsewhere [13]. Eq. (4.2) can be used to determine the effective water diffusion coefficient D_{eff,H_2O}, if the possible swelling of the epoxy adhesives is ignored [86,95,99].

$$\frac{\ln C_t - \ln C_0}{\ln C_s - \ln C_0} = \frac{2\sqrt{t}}{d\sqrt{\pi}}\sqrt{D_{eff}} \tag{4.2}$$

where C_t is the capacitance of the time t , C_0 is the dry coating capacitance, C_s is the coating capacitance when the coating is saturated with water and d is the coating thickness [95].
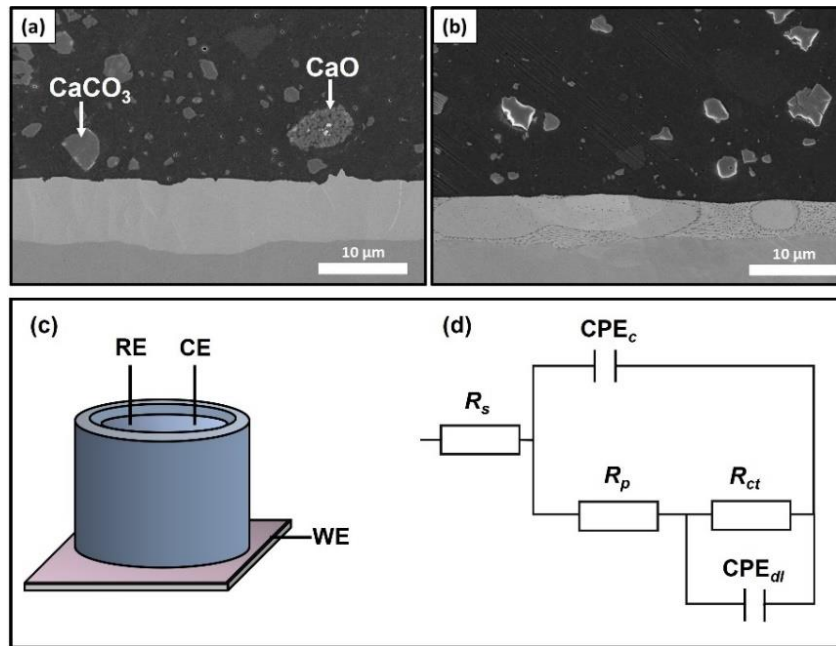
Figure 4.1: SEM images of MF coated ZE (a) and ZM (b) surfaces as well as a schematic of the setup for measuring the water absorption of organic coatings on metal substrates by means of EIS (c) and an equivalent circuit for describing epoxy-coated metal surfaces (d).

4.2.4 Cataplasma tests performed in atmospheric conditions, oxygen-depleted and oxygen-rich atmospheres

To investigate the impact of CaO, $CaCO_3$ and hydrophobic fumed SiO_2 on the delamination resistance of the epoxy adhesives, cataplasma tests according to EN ISO 9142 were carried out. For this purpose, ZE and ZM steel sheets were cut into 80 x 150 mm² pieces and cleaned ultrasonically with benzine and acetone. The sample surfaces were then knife coated with MF, MF$_{\text{without inorganic additives}}$ and MF$_{\text{without inorganic additives}}$ mixed with either 5 or 10 wt% CaO, 16 or 32 wt% $CaCO_3$ and 3 or 6 wt% hydrophobic fumed SiO_2. The coatings were cured at 180 °C for 0.5 h and the thickness of the adhesive layer was measured using a Fisher PHASCOPE PMP10 DUPLEX portable coating thickness gauge. The dry film thickness d was 135 ± 20 µm for all cataplasma tests. Afterwards, a 1 mm wide and 70 mm long defect was scratched with a Sikkens scratching tool through the polymer coating into the metal coating of each sample. In order to

prevent edge corrosion, the sample edges were covered with tape. For the cataplasma test, samples were soaked at 70 °C in a water saturated atmosphere. To reach this environment, samples were individually wrapped in cotton wool and soaked in deionized water. The cotton wool wrapped samples were then placed in sealable polyethylene bags and the samples were placed in an oven at 70 °C. Ageing of the samples took place over 3 weeks. Before the delaminated coating was removed, the samples were cooled at -20 °C for at least 2 hours. For the evaluation of the results, an area of interest of 40 x 70 mm² was determined for all samples, including the 70 mm long artificial defect in the middle of the shorter side. Subsequently, the delaminated area of each sample was removed with a scalpel and its extent was determined with ImageJ.

To understand the different delamination mechanisms of CaO and $CaCO_3$ filled coatings compared to MF coatings during cataplasma aging, further cataplasma tests with oxygen-depleted and oxygen-rich atmospheres were performed. Here, the samples were prepared in the same way as for the previously performed cataplasma tests. In contrast to the previous cataplasma tests, cataplasma aging was performed in climate chambers that were regularly flushed with either argon or oxygen. The evaluation of the results was identical to the first cataplasma tests.

4.3   Results and Discussion

In this work, the influence of commonly used inorganic fillers in adhesives for the automotive industry in form of CaO, $CaCO_3$ and hydrophobic fumed SiO_2 was investigated systematically. Therefore, the inorganic additives were mixed into a model formulation without inorganic additives and compared with a realistic one-component epoxy adhesive that already contained CaO, $CaCO_3$ and hydrophobic fumed SiO_2. EIS measurements were conducted to determine the water absorption and diffusion of water in

all adhesive formulations. Cataplasma ageing in various atmospheres allowed the different delamination processes at the inorganic additive-filled coating/metal interface to be elucidated.

4.3.1 Water uptake behavior of inorganic additives filled structural adhesives using EIS

EIS measurements were carried out to determine the water absorption next to the effective water diffusion coefficient in the adhesive and to investigate the influence of inorganic components in MF$_{without\ inorganic\ additives}$ on the additional water uptake. It was therefore necessary to determine the coating capacitance C_t, which was calculated from the EIS data according to Eq. 4.3 at a fixed frequency [97].

$$C_t = \frac{1}{2\pi f Z''} \tag{4.3}$$

where f is the frequency and Z'' is the imaginary part of the impedance at f.

The frequency chosen was 4.0 kHz (0-160 h) for epoxy coatings with 6 wt% SiO$_2$ and 5 wt% CaO, while for coatings with 3 wt% SiO$_2$ the frequencies were 4.0 kHz (0-2 h) and 6.3 kHz (2-160 h), as the total impedance of the system in this high frequency region was determined by the coating capacitance. For MF, MF$_{without\ inorganic\ additives}$ and coatings with 10 wt% CaO, the frequency 6.3 kHz (0-160 h) was selected. For MF$_{without\ inorganic\ additives}$ with 16 wt% or 32 wt% CaCO$_3$, the frequencies 4.0 kHz (0-80 h) and 6.3 kHz (80-160 h) were chosen to calculate the coating capacitance. All selected frequencies were in a frequency range where the phase angle θ was close to -90 degrees.

Figs. 4.2a-c compare one of the obtained water uptake curves of MF$_{without\ inorganic}$ $_{additives}$, MF$_{without\ inorganic\ additives}$ mixed with CaO, CaCO$_3$, hydrophobic fumed SiO$_2$, and MF coated ZE samples from at least three measurements. The mean values of all measurements can be found in Table 4.2. On the right side of each water uptake curve, a close-up of the water uptake curves during the initial exposure time and the linear regression of each water uptake curve are

presented to show the linear water uptake when the coating was first exposed to the electrolyte. All EIS measurements were performed on ZE surfaces, as previous studies showed that there are no significant differences between the water uptake on epoxy coated ZE and ZM surfaces [13]. In order to eliminate the thickness effect of the coatings, all water uptake curves were plotted as a function of reduced time $\tau = \sqrt{t}/d$, where t is the immersion time and d the coating thickness [100]. As expected and shown in Fig. 4.2a, mixing CaO in MF$_{without\ inorganic\ additives}$ attracted water because CaO has a reactive surface and thermodynamic driving force to hydrate to $Ca(OH)_2$, a more stable compound [143]. A non-linear water uptake behaviour was observed when twice the amount of CaO was added. This might indicate that not only CaO was converted to $Ca(OH)_2$, but also other processes took place in the adhesive leading to an increased water uptake. One reason for the non-linear water absorption could be that the formed $Ca(OH)_2$ was partially washed out of the adhesive due to its very low water solubility, resulting in holes in the coating [144]. In addition, a saturated $Ca(OH)_2$ solution can form around the $Ca(OH)_2$ particle with a pH between 12 and 12.5. The local alkaline pH value at the adhesive/zinc interface can lead to dissolution of the zinc layer and form corrosion products such as calcium hydroxyzincate $(Ca[Zn(OH)_3]_2 \cdot 2H_2O)$, zinc oxides (ZnO) or zinc hydroxides $(Zn(OH)_2)$ [145–148]. An additional water uptake was also observed by adding $CaCO_3$ to the adhesive as demonstrated in Fig. 4.2b, while no additional water absorption was recorded in coatings that were filled with hydrophobic fumed SiO_2 which is shown in Fig 4.2c. Prevention of water transport into the adhesive by adding hydrophobic additives was not observed. Comparing the water uptake curves of the coatings filled with 16 wt% and 32 wt% $CaCO_3$, it can be noticed that the more $CaCO_3$ was added to the adhesive, the lower the additional water uptake due to the addition of $CaCO_3$. As previously mentioned, $CaCO_3$ is an inert filler which hardly reacts with water. In the literature, it is described that inert fillers are capable to physically prevent penetration of water into the adhesive, and to slow its kinetics by blocking and/or extending diffusion pathways [137,138].

However, this applies more to inert fillers that have a high diameter-to-thickness ratio, such as 2D nanomaterials like graphene, graphene oxide, boron nitride, mica, and zirconium phosphate. In the case of $CaCO_3$, the physical barrier effect plays a rather minor role, since the 5-10 µm particles are relatively small and have a low diameter-thickness ratio, which was later shown by the determined diffusion coefficients in Fig. 4.3 [149–151]. To conclude, the water uptake curves showed that the water uptake of MF compared to MF_{without inorganic additives} was due to the added CaO and $CaCO_3$, while hydrophobic fumed SiO_2 had no effect on the water uptake behavior, as shown in Fig. 4.2 a-c.
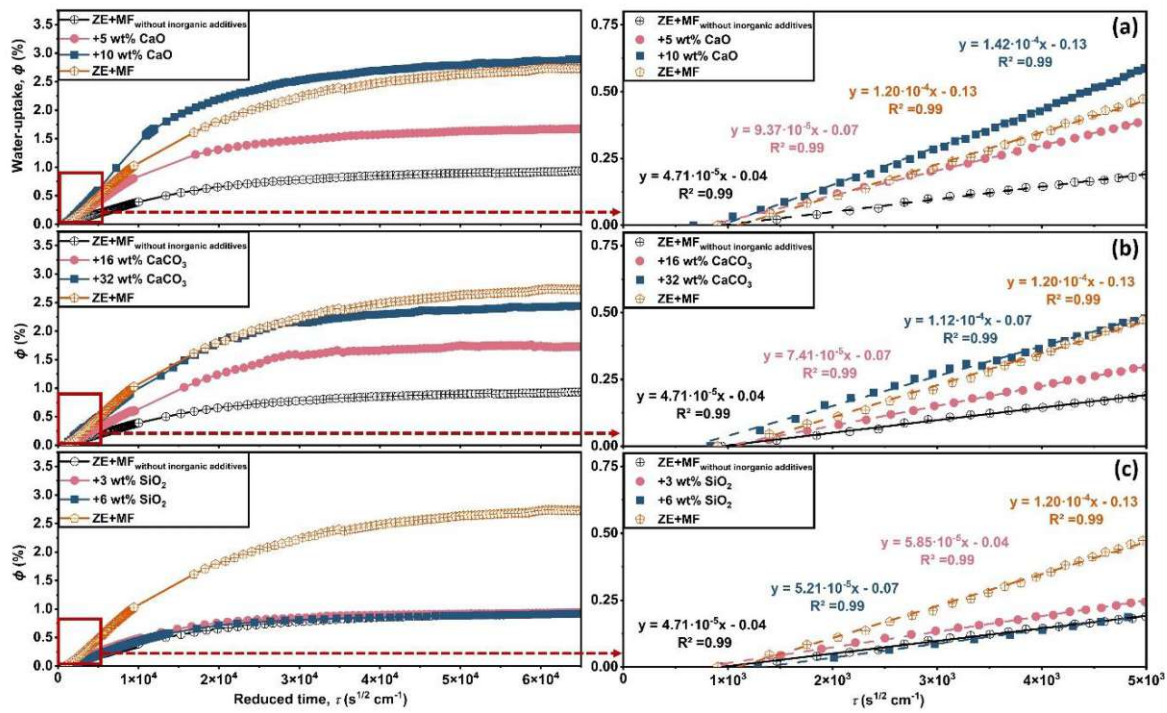
Figure 4.2: Comparison of water uptake curves of MF_{without inorganic additives}, MF_{without inorganic additives} mixed with CaO (a), $CaCO_3$ (b), hydrophobic fumed SiO_2 (c) and MF coated ZE samples determined by EIS (left), with a close-up of the water uptake curves during the initial exposure time and linear regression of each water uptake curve to show the linear water uptake when the coating was first exposed to the electrolyte (right).

Fig. 4.3 illustrates the effective water diffusion coefficients of MF_{without inorganic}

additives and with a defined concentration of CaO, CaCO$_3$ and hydrophobic fumed SiO$_2$. It was found that all measured diffusion coefficients only differ slightly from each other and were in a similar range of 10^{-13} m² s^{-1}. The effective water diffusion coefficients agreed well with values found in literature [11,102,103]. Here, Fig. 4.3 shows that water molecules diffused slightly slower in MF than in MF$_{without\ inorganic\ additives}$. Differences in water diffusion coefficients were only observed when different inorganic fillers were mixed in MF$_{without\ inorganic\ additives}$, whereas minimal to no differences were found when the amount of a particular inorganic filler was varied. This suggests that the presence of a filler can trigger certain damage mechanisms as assumed for the CaO filled coatings when in contact with water, which then leads to an increase in the water diffusion rate. Another reason for the increased D_{eff,H_2O} could be the reactivity of the CaO surface with water, which pulls water molecules into the coating and immediately converts CaO to Ca(OH)$_2$. Comparing CaO filled coatings with CaCO$_3$ filled coatings, the addition of CaCO$_3$ resulted in a decrease of D_{eff,H_2O}. Since the diffusion rate did not change significantly when the amount of CaCO$_3$ was doubled, it can be assumed that no path lengthening of the diffused water molecules was responsible for the lower diffusion coefficient. Studies have shown that the addition of certain inorganic additives, for example CaCO$_3$ or BaSO$_4$, to organic coatings may change the morphology of the polymer, which could explain the lower diffusion coefficient. For example, the addition of nano-BaSO$_4$ particles to neat epoxy resin resulted in a higher cross-linking density [152,153]. It could also be seen that hydrophobic fumed SiO$_2$ slightly increased D_{eff,H_2O}. In contrast to previous work, our data suggests that hydrophobized SiO$_2$ can lead to accelerated water absorption, which is likely due to more defects at the metal/coating interface [154–156]. Our observations are also consistent with work by Dolatzadeh *et al.* (2013), where they showed that the addition of hydrophobic fumed silica to the uncured polyurethane matrix can negatively affect the curing process, leading to a lower degree of curing and thus accelerating water diffusion [157]. Comparing the slightly increased effective water diffusion coefficient with the results from Fig. 4.2c, where the amount of water absorbed did not change

when hydrophobic fillers were added to MF$_{\text{without inorganic additives}}$. It seems that a more wide-meshed network was created, leading to faster water diffusion. The amount of water absorbed is assumed not to have changed compared to MF$_{\text{without inorganic additives}}$, because the wider-meshed network was able to absorb more water, but not in the areas around the hydrophobic fillers. As a result of both effects, the water uptake was compensated in such a way that the hydrophobic fumed SiO_2 apparently had no influence on the amount of water absorbed by the coating, but only affected the diffusion rate.
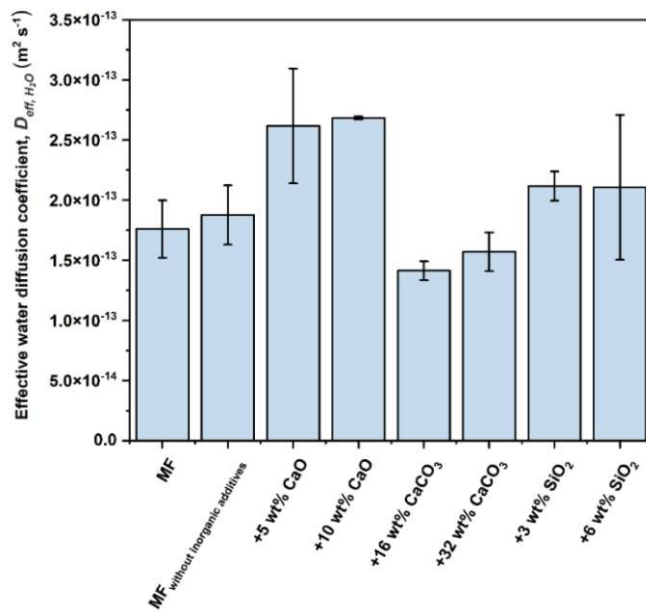
Figure 4.3: Effective water diffusion coefficients of MF, MF$_{\text{without inorganic additives}}$ and MF$_{\text{without inorganic additives}}$ mixed with a defined concentration of CaO, $CaCO_3$ and hydrophobic fumed SiO_2.

Table 4.2 summarizes the water uptake values of MF and MF$_{\text{without inorganic additives}}$ mixed with 5 wt% CaO, 10 wt% CaO, 16 wt% $CaCO_3$, 32 wt% $CaCO_3$, 3 wt% SiO_2 and 6 wt% SiO_2 as well as the effective water diffusion coefficients measured via EIS.

Table 4.2: Water uptake of MF and MF$_{without\ inorganic\ additives}$ mixed with 5 wt% CaO, 10 wt% CaO, 16 wt% CaCO$_3$, 32 wt% CaCO$_3$, 3 wt% SiO$_2$ or 6 wt% SiO$_2$ on ZE surfaces as well as effective water diffusion coefficient measured via EIS.

Adhesive	wt$_{CaO}$ (%)	wt$_{CaCO_3}$ (%)	wt$_{SiO_2}$ (%)	ϕ_{H_2O} (%)	$D_{eff,\,H_2O}$ (m^2 s^{-1})
MF$_{without\ inorganic\ additives}$	0	0	0	1.05 ± 0.13	1.88 x 10^{-13} ± 2.48 x 10^{-14}
MF$_{without\ inorganic\ additives}$	5	0	0	1.57 ± 0.19	2.62 x 10^{-13} ± 4.76 x 10^{-14}
MF$_{without\ inorganic\ additives}$	10	0	0	2.60 ± 0.30	2.68 x 10^{-13} ± 1.25 x 10^{-15}
MF$_{without\ inorganic\ additives}$	0	16	0	1.85 ± 0.06	1.41 x 10^{-13} ± 7.93 x 10^{-15}
MF$_{without\ inorganic\ additives}$	0	32	0	2.35 ± 0.16	1.57 x 10^{-13} ± 1.60 x 10^{-14}
MF$_{without\ inorganic\ additives}$	0	0	3	0.97 ± 0.01	2.12 x 10^{-13} ± 1.22 x 10^{-14}
MF$_{without\ inorganic\ additives}$	0	0	6	0.96 ± 0.15	2.11 x 10^{-13} ± 6.02 x 10^{-14}
MF	5	16	3	2.54 ± 0.24	1.76 x 10^{-13} ± 2.39 x 10^{-14}

4.3.2 Impact of inorganic fillers in adhesives on delamination process as well as on their delamination resistance

Cataplasma tests according to EN ISO 9142 were chosen to evaluate the influence of coatings with different amounts of CaO, CaCO$_3$ and hydrophobic fumed SiO$_2$ on the delamination process at the interface of ZE and ZM surfaces. The cataplasma test was chosen even though it is known that the cataplasma test may not be fully representative of real automotive environmental conditions. Cyclic corrosion tests proved to be more reliable for the classification of the coating performance. However, cyclic corrosion tests often require the use of NaCl solutions. Studies have shown that the NaCl concentration has a great influence on the coating degradation [158,159]. In order to neglect this influence and evaluate only the influence of the inorganic additive filled coated sample systems on the delamination behaviour, the cataplasma test was chosen, using deionized water as electrolyte instead of NaCl solutions. It should also be noted that this study uses an open sample geometry approach instead of closed joints. This sample geometry is more frequently used when evaluating the delamination behaviour of coatings such as paints and rarely for adhesives. It is important to note that this allows both water and atmospheric gases to reach the interface through the coating as well

and not just through the exposed edges as would be the case with a closed joint geometry. Andreon *et al.* performed in-situ SKP measurements on an open and a closed sample geometry and found, for example, that cathodic delamination is significantly slowed down due to less available oxygen in closed joint geometry compared to an open sample geometry [160]. Although the sample geometry does not change the electrochemical delamination process, as shown by Andreon *et al.*, the results do not fully translate to adhesive performance, but more so to coatings such as paints. However, the sample geometry was relevant for assessing and visualizing the delamination process at polymer/metal interface when inorganic additives were added. Although the same coatings were used for cataplasma aging, two different delamination processes were observed on the ZE and ZM surfaces as shown in Fig. 4.4 where optical images of cataplasma aged ZE surfaces (a) coated with MF, MF$_{\text{without inorganic additives}}$ and mixed with 5 and 10 wt% CaO and cataplasma aged ZM surfaces (b) coated with MF, MF$_{\text{without inorganic additives}}$ and mixed with 5 and 10 wt% CaO, where the cataplasma tests were conducted in oxygen-depleted environment, are illustrated. During the cataplasma test, blisters, partially filled with an electrolyte, were formed on ZE substrates, whereas no blistering was observed on ZM surfaces. The delamination process on ZM surfaces was similar to filiform corrosion in appearance. This result indicates that the different composition of the two zinc coatings had a profound influence on the delamination behavior of the adhesive during cataplasma aging, which was also shown in a previous study where the delamination processes were investigated with scanning Kelvin probe measurements.

In our study, it was confirmed that epoxy coated ZE surfaces preferentially undergo cathodic delamination, while epoxy coated ZM surfaces are prone to delaminate anodically [13]. Due to the different delamination processes on ZE and ZM surfaces, the blister area was used to evaluate the delamination resistance of epoxy coated ZE surfaces. On ZM the extent of filiform corrosion on ZM surfaces was used for evaluation.
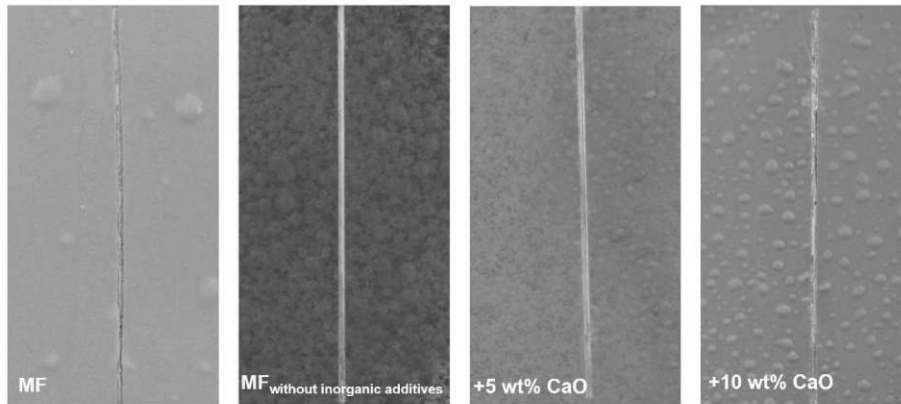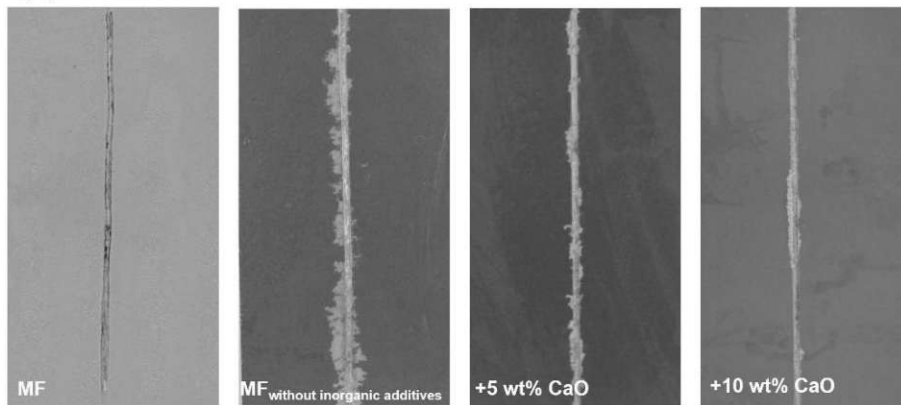
Figure 4.4: Optical images of cataplasma aged ZE surfaces (a) coated with MF, MF$_{\text{without inorganic additives}}$ and mixed with 5 and 10 wt% CaO, and cataplasma aged ZM surfaces (b) coated with MF, MF$_{\text{without inorganic additives}}$ and mixed with 5 and 10 wt% CaO where the cataplasma tests were conducted in an oxygen-depleted environment.

Fig. 4.5 demonstrates the influence of hydrophobic fumed SiO$_2$ embedded in MF$_{\text{without inorganic additives}}$ compared to MF and MF$_{\text{without inorganic additives}}$ on ZE and ZM surfaces after cataplasma aging in atmospheric environment. Results showed that hydrophobic fumed SiO$_2$ filled MF$_{\text{without inorganic additives}}$ coatings on ZE surfaces had an equally large blister area of approximately 40 % as MF$_{\text{without inorganic additives}}$ on the ZE surface. In contrast to blistering which occurred on ZE surfaces, filiform corrosion was observed under the SiO$_2$ filled coatings on ZM surfaces. In comparison, coatings filled with SiO$_2$ behaved in the same way as

the MF_{without inorganic additives} coated ZM substrates. Differences were only noticed on MF coated metal substrates.
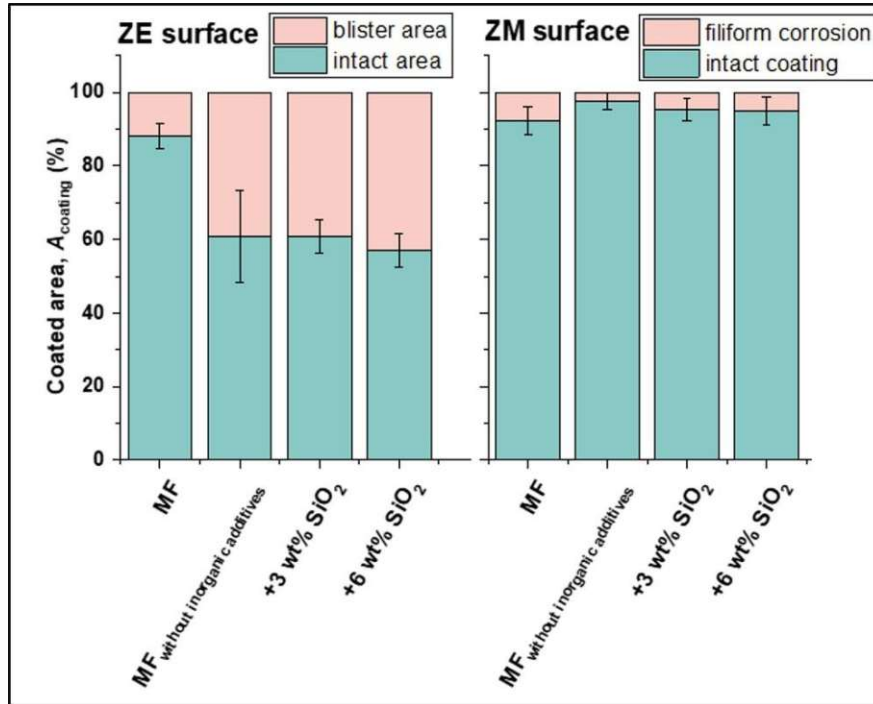
Figure 4.5: Influence of hydrophobic silica mixed to MF$_{\text{without inorganic additives}}$ compared to MF and MF$_{\text{without inorganic additives}}$ on ZE and ZM surfaces after the cataplasma test in atmospheric environment.

Compared to SiO$_2$ filled coatings, MF coated ZE samples were more delamination resistant during cataplasma aging. In contrast, deteriorated delamination resistance was detected on MF coated ZM surfaces. One reason for this could be the addition of CaO and CaCO$_3$ in MF, which are not present in MF$_{\text{without inorganic additives}}$ and which may provide better adhesion to the zinc surface. In contrast to SiO$_2$ filled coatings, CaO and CaCO$_3$ filled coatings exhibited different water absorption and delamination behavior than metal surfaces coated with MF$_{\text{without inorganic additives}}$ during cataplasma aging in an atmospheric environment, as shown in Fig. 4.6b. For this purpose, cataplasma tests were performed in climate chambers that were regularly purged with

argon or oxygen. The results of these cataplasma tests on ZE and ZM surfaces coated with MF, MF$_{without\ inorganic\ additives}$ mixed with/without CaO and CaCO$_3$ in atmospheres with different oxygen concentrations are displayed in Fig. 4.6a-c. Fig. 4.6a illustrates the results of the cataplasma test in a low-oxygen environment, while the results of the cataplasma test under atmospheric conditions are displayed in Fig. 4.6b and in an oxygen-rich environment on ZE and ZM surfaces in Fig. 4.6c. These experiments were done to distinguish between osmotically induced blistering and blister formation due to cathodic delamination. If looking at the results of the CaCO$_3$ filled coatings on ZE, it can be seen immediately that almost no blisters were formed in an oxygen-depleted environment, which indicates that the blisters formed during cataplasma aging were not due osmosis. Another indication of this assumption is that blistering increased with higher oxygen concentration, suggesting that blistering was caused by cathodic delamination rather than osmotic blistering. As mentioned above, CaCO$_3$ is an inert filler. Due to its inertness, CaCO$_3$ hardly reacts with other additives in the adhesives or environmental components such as moisture or CO$_2$. Therefore, no concentration gradient was created in the coating that allowed the generation of osmotic pressure, which can then cause blistering [137,138]. However, if inert fillers with a low diameter-to-thickness ratio are added, water diffusion is not blocked. Due to additional defects such as micropores that may occur due to the addition of such additives in the adhesive during curing, the electrolyte can still penetrate into the polymer/metal interface where electrochemical processes such as cathodic delamination can occur, as observed with coatings mixed with CaCO$_3$ on ZE surfaces and demonstrated in a previous study [13,111,111]. Considering the CaO filled MF$_{without\ inorganic\ additives}$, it was found that the extent of blister formation during cataplasma aging was the same in oxygen-depleted and atmospheric environments. The blister area increased just in an oxygen-rich atmosphere. Only when the oxygen content was greatly increased, additional blisters were formed due to cathodic delamination in addition to those produced by osmosis. Therefore, it can be concluded that CaO in MF$_{without\ inorganic\ additives}$ can cause

osmotic blistering during cataplasma aging. Whereas osmotic blistering was not observed in $CaCO_3$ filled coatings applied on ZE surfaces. However, coating defects occur on ZE surfaces, leading to increased blistering due to cathodic delamination.

Further evidence for this assumption can be found in Fig. 4.7, where optical images of two delaminated ZE surfaces coated with CaO and $CaCO_3$ filled MF$_{without\ inorganic\ additives}$ after cataplasma aging in an oxygen-depleted environment are shown. Dissolution of the zinc layer under the blisters was observed on the ZE surface under the delaminated CaO filled coating. When water penetrates the CaO filled coating, the contained CaO is hydrated to $Ca(OH)_2$. Even though it is poorly soluble in water, a $Ca(OH)_2$ solution will be formed around the $Ca(OH)_2$ particle with a pH of up to 12.5. This can lead to dissolution of the zinc coating and corrosion products such as $Ca[Zn(OH)_3]_2 \cdot 2H_2O$, ZnO or $Zn(OH)_2$ are formed [145–148]. Due to the reactions at the interface, a concentration gradient is formed, which leads to osmotic blister formation. The dissolution of the zinc coating is characterized by the dark spots on the ZE surface formed under the blisters when the coating was filled with CaO. On the other hand, no dark spots or blisters were observed during cataplasma tests under oxygen-depleted atmosphere when the coating was filled with $CaCO_3$, indicating that osmotic blistering is not induced by the addition of $CaCO_3$ to the adhesive.
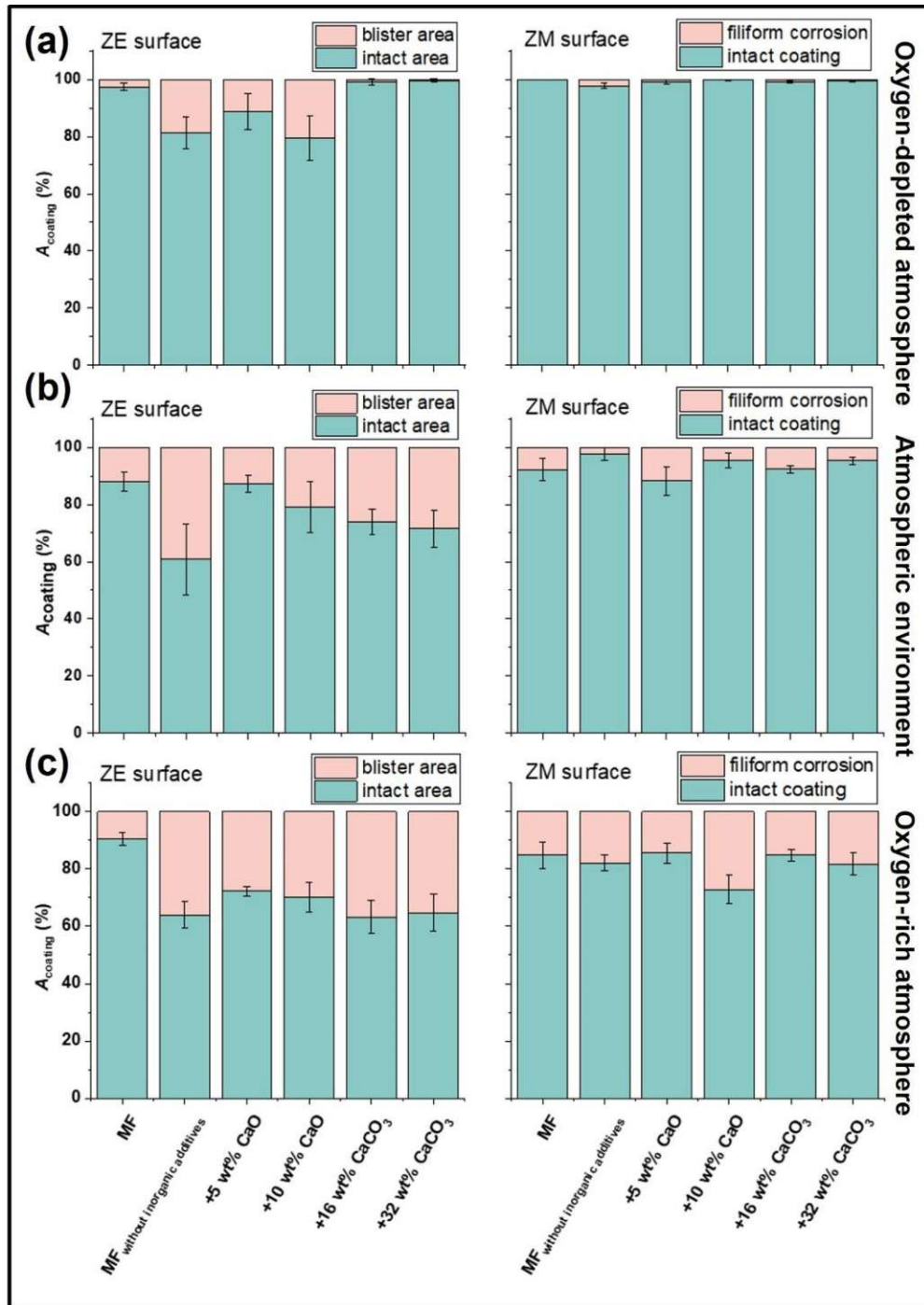
Figure 4.6: Results of the cataplasma test on ZE and ZM surfaces coated with MF, MF$_{\text{without}}$ $_{\text{inorganic additives}}$ mixed with/without CaO and CaCO$_3$ in oxygen-depleted atmosphere (a), atmospheric environment (b) and oxygen-rich atmosphere (c).
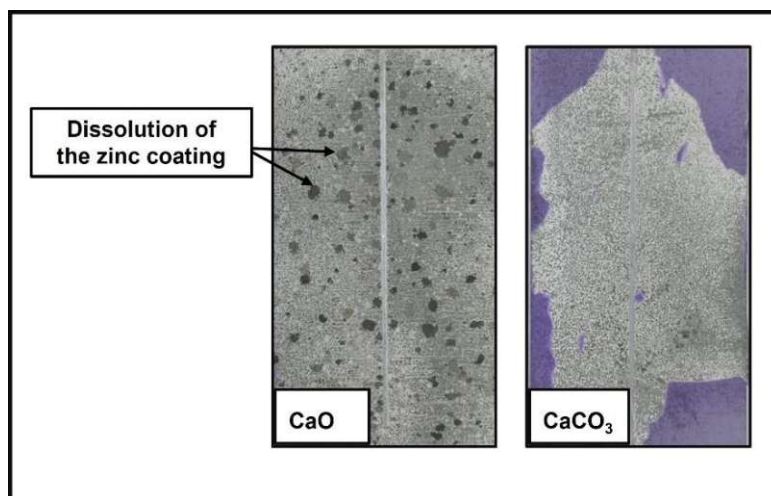
Figure 4.7: Optical images of two delaminated ZE surfaces after cataplasma aging in an oxygen-depleted environment when coated with CaO and CaCO$_3$ filled MF$_{without\ inorganic\ additives}$, where dissolution of the zinc coating under the blisters was noticed on the ZE surface under the delaminated CaO filled coating.

4.4 Conclusion

EIS was used to measure the water uptake of inorganic additives. Results suggested that hydrophobic SiO$_2$ may lead to accelerated water uptake. Our data indicate that water transport in the adhesive was not prevented by the addition of hydrophobic additives. Additional cataplasma tests in different environments allowed to distinguish whether blistering on ZE surfaces was caused by osmosis or cathodic delamination. It was confirmed that CaO caused osmotic blistering and accelerated the diffusion of water into the adhesive. In contrast, no osmotic blister formation was observed on CaCO$_3$ filled coatings applied on ZE surfaces. However, coating defects do occur on ZE surfaces, leading to increased cathodic blister formation. It was also confirmed that oxygen accelerated the delamination process on CaO and CaCO$_3$ filled coatings on ZM surfaces.

Chapter 5

Versatile, low-cost, non-toxic potentiometric pH-sensors based on niobium

The following chapter is based on the article published under the same title in the journal Sensing and Bio-Sensing Research (see [161]) and reproduced under the corresponding copyright agreement. The pH value is an important parameter in corrosion research, as it can provide information about corrosion mechanisms. For this reason, pH sensors based on niobium were manufactured that are inexpensive, non-toxic, easy to produce and have an excellent long-term stability. Our study shows that the electrochemical preparation method yields pH electrodes with high reproducibility and a sensitivity of about 0.04 V/pH over a pH range of 2-12. Characterisation of the fabricated NbO_x electrodes was performed by SEM, EDX and EIS. Our results show that NbO_x electrodes are robust pH sensors that allow long-term monitoring of pH changes. Thus, these sensors offer the possibility of having important implications for corrosion research.

Experiments were conducted with the help of Ines Traxler and Gabriela Schimo-Aichhorn, whereas the SEM and EDX measurements were kindly carried out by Marcus Molnar from voestalpine Stahl GmbH.

A low-cost potentiometric pH electrode based on Nb/NbO_x was developed with excellent stability over several months under various storage conditions. Three fast and simple preparation routes including thermal growth as well as

chemical and electrochemical deposition were tested. Our data demonstrates that the electrochemical manufacturing method produces pH electrodes with high reproducibility and a sensitivity of -41 mV/pH. OCP (Open Circuit Potential) measurements showed that the pH electrode can be used over a wide pH range from pH 2 to 12. Furthermore, the oxide layer of all produced electrodes was characterized and compared via SEM, EDX (Energy-Dispersive X-Ray Spectroscopy) and EIS. It was shown that the electrochemical fabrication route leads to the highest porosity, which is in turn linked to the highest sensitivity. The hysteresis of this pH sensor was determined to be 2 mV in a pH region between 4 and 10. In long-term experiments a drift of 1.1 mV/h was obtained. Negligible interference was observed with NaCl and KCl ions, whereas sensitivity and linearity were affected by Li-ions.

5.1 Introduction

One of the most important parameters in corrosion research is the pH value as it can give insights into corrosion mechanisms or indicate corrosion pathways via pH mappings [162–166]. Therefore, pH electrodes with a wide measuring rang and a high long-term stability are required. MO_x pH sensors offer these advantages and are, among other things, easy to miniaturize, mechanically and chemically stable as well as relatively stable in salt solutions, which is necessary for pH monitoring during corrosion experiments or in biological systems [167,168]. Metal oxides that have already been used to produce MO_x pH electrodes include IrO_2 [166,169–172], RuO_2 [172–174], TiO_2 [172,175], WO_3 [176], Sb_2O_3 [177], OsO_2 [172], Ta_2O_5 [172], SnO_2 [172,178], ZrO_2 [172], PdO [179], and PtO_2 [180]. Among these metal oxides, the most promising ones are IrO_2 and RuO_2 pH electrodes. RuO_2 is an electrochemically conductive oxide with a stable rutile structure. Similar to RuO_2, IrO_2 is an electrochemically conductive oxide which crystallizes in the rutile structure but has a lower catalytic activity than RuO_2. Both MO_x pH electrodes have excellent stability over a wide pH range, high sensitivity near Nernstian potential, fast response and long lifetime

[167,170,181,182]. Common fabrication methods for IrO_2 pH electrodes include electrochemical methods such as electrochemical oxidation of Ir wires [183], anodic electrodeposition [184], or reactive sputter deposition [185], as well as thermal oxidation of Ir wires in potassium nitrate or carbonate [170,186] and thermal deposition of iridium salts [187]. A variety of methods are also known for the preparation of RuO_2 pH sensors, such as screen printing [188–190], sputter deposition [191], thermal decomposition [192,193] or the Pechini method [168,181]. It is known that the performance of the MO_x pH electrode is highly dependent on the manufacturing method, the metal oxide pH sensing material as well the type of material composition, because they affect the microstructure, porosity, surface homogeneity as well as the crystal structure of the metal oxide and thus influence the sensitivity of the electrode [167]. Therefore, when developing a new MO_x pH electrode material, it is important to investigate different fabrication routes and their influence on the formed metal oxide layer. Despite the demonstrated pH sensing properties of NbO_x, there is little literature on niobium oxide used as MO_x pH sensor [194–197]. Gill et al. reported that the pH sensing properties of bismuth-niobium mixtures worked very well over a wide pH range and that pH electrodes with higher niobium content demonstrated higher stability than pH electrodes with high bismuth concentrations [198]. For this reason, we investigated whether NbO_x would be suitable as MO_x pH electrodes for corrosion research. Besides RuO_2 and IrO_2, NbO_x could be another promising pH sensor material for monitoring corrosion processes as it is easily available, inexpensive, chemically very stable and non-toxic [199]. In literature, it is described that Nb forms a porous Nb_2O_5 film upon anodic polarization, which is used for catalytic applications, batteries, hydrogen sensors and solar cells [200–202]. In contrast to RuO_2 and IrO_2, Nb_2O_5 is not a conductor but a n-type transition metal oxide semiconductor with a wide band gap of about 3.2 eV [199,201]. The pH sensing mechanism of semiconductors including the reaction mechanisms between solution and metal oxide is currently still under investigation. However, adsorption of hydronium and hydroxide ions and resulting change of the electrical characteristics of the oxide

film are a central explanatory approach [198].

In this work various preparation techniques for niobium pH electrodes are tested and their pH sensing properties are investigated, as well as their long-term stability. Furthermore, the oxide layer of the electrodes was characterized by means of SEM, EDX and EIS. In addition, the sensor properties such as drift, hysteresis and interferences with LiCl, KCl and NaCl were determined on the electrochemically produced NbO_x electrodes.

5.2 Materials and Methods

5.2.1 Preparation of NbO_x electrodes

For the preparation of the NbO_x electrodes, a 1 mm thick niobium wire (99.8 %, Alfa Aesar, Germany) was used. The Nb wire was cut into 2 cm long pieces and ultrasonically cleaned in ethanol (per analysis, Carl Roth, Germany) for 5 min. Then three different preparation routes for the formation of the desired Nb oxides on the Nb wire were tested: the first was a thermal treatment, the second a chemical preparation and the third an electrochemical preparation method. For the thermal preparation the Nb wire was heated in a drying cabinet (ED115, Binder, Germany) at 250 °C for 10 min to form the wanted oxide layer. The chemical preparation route consisted of immersing 1 cm of the Nb wire for 24 h at room temperature in a 0.1 wt% potassium permanganate solution (99 %, Carl Roth, Germany), followed by rinsing with ethanol. For the electrochemical method, 1 cm of the Nb wire was positioned in a 0.1 M hydrochloric acid solution (37 %, per analysis, Carl Roth, Germany) at room temperature and a cyclic voltammogram from -0.5 to 2.2 V (vs. SHE) was carried out followed by polarization at 1.7 V (vs. SHE) for 1 h. All electrochemical measurements were carried out using a CompactStat.h potentiostat (Ivium Technologies, Netherlands), a Ag/AgCl/3 M KCl electrode (Metrohm, Switzerland) as reference electrode and a platinum electrode as counter electrode. After oxidation of the Nb wire, the electrode was insulated with Teflon at the area

where the Nb wire was not oxidized to obtain a defined electrode area, as shown in Fig. 5.1.
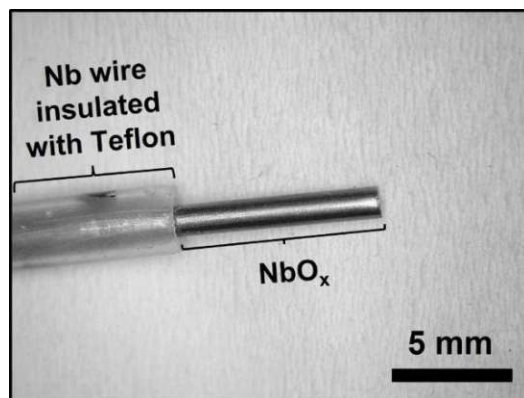
Figure 5.1: Image of NbO_x pH electrode.

5.2.2 pH response measurements and storage conditions

To investigate the pH dependency of the sensor response, OCP measurements were carried out. The OCP measurements were done in commercially available pH buffer solutions (pH 1, 1.7, 4, 5, 7, 9, 10, 11 and 13, pH ± 0.02 (20 °C), Carl Roth, Germany) starting from pH 13 to 1. The electrodes were preconditioned for 15 min in pH 13 buffer solution. The same conditions and buffer solutions were used for the hysteresis, drift and ion interference measurements. The evaluation of the drift effect was carried out in the pH 7 buffer solution for 24 h. For the determination of the interference with alkali metal ions aqueous solutions of LiCl, NaCl and KCl (per analysis, Carl Roth, Germany) were added to the buffer solutions in order to reach a concentration of 0.1 mol l^{-1}.

The time-dependent pH response of the electrochemically prepared electrodes was examined by titration of the NbO_x electrode with 1 M sodium hydroxide solution (>99 %, Carl Roth, Germany) and 1 M hydrochloric acid solution from pH 13 to 1. Here, the electrode was also preconditioned for 15 min in pH 13 and the pH value of the solution was controlled with a pH meter (pH 70, XS

Die approbierte gedruckte Originalversion dieser Dissertation ist an der TU Wien Bibliothek verfügbar.

The approved original version of this doctoral thesis is available in print at TU Wien Bibliothek.

TU Bibliothek
Your knowledge hub

Instruments, Italy) connected to a PC. The response time of the fabricated pH electrode was determined as described elsewhere [167].

5.2.3 NbO$_x$ electrode characterization

The characterization of the oxide layer of the differently prepared NbO$_x$ electrodes was done with SEM (Zeiss Ultra 55). Cross-sections of the electrodes were prepared by cold embedding to determine the oxide layer thickness. EDX mappings of the oxide layer were recorded with a Zeiss Ultra 55 with an X-Max 50mm^2 detector an acceleration voltage of 15 kV. In order to determine the porous area fraction optically from the SEM images which is defined by the area of pores divided by the total area of the investigated image region the ImageJ software was used [203].

EIS was done for characterization of the oxide layers and for determination of the porosity. A three-electrode cell arrangement consisting of a DSA as counter electrode, a Ag/AgCl/3 M KCl electrode as reference electrode and the NbO$_x$ electrode as working electrode were employed. The measurements were performed at room temperature in a 3.5 wt% NaCl solution and with a frequency range of 10^{-2}-10^4 Hz using a 10 mV AC perturbation at OCP, which was determined prior to the EIS. The EIS spectra were fitted with ZView software (Scribner Associates, United States).

5.3 Results and Discussion

In this work, NbO$_x$ electrodes were prepared in a thermal, chemical and electrochemical approach. The pH response of each electrode was examined in pH buffer solutions over a pH range of 1-13. The response time was evaluated via acid-base titration. Long-term stability was tested for different storage conditions over several months. For the investigation of the oxide layer, SEM, EDX and EIS measurements were carried out.

5.3.1 Comparison of chemically, thermally and electrochemically produced NbOₓ electrodes

Fig. 5.2 illustrates the OCP measurements of the three preparation approaches directly after manufacturing. The electrochemically produced NbO_x electrode revealed the highest sensitivity with -41 mV/pH, followed by the chemical pH electrode with -38 mV/pH. The NbO_x electrode with the thermally formed oxide layer showed the lowest sensitivity and poorest linearity in OCP values over the pH range. Thus, this preparation method was rejected. Directly after preparation, the electrochemical and chemical electrodes demonstrated excellent linearity over the whole investigated pH range. Since the electrochemical approach displayed the highest sensitivity and linearity, as well as the shortest preparation route, this preparation method was chosen for further experiments.
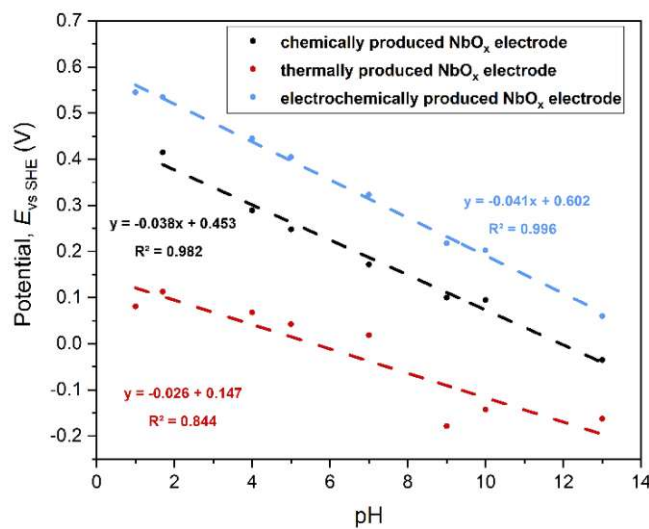
Figure 5.2: OCP measurements (electrode potential versus standard hydrogen electrode (SHE)) of chemically (black), thermally (red) and electrochemically (blue) produced NbO_x electrodes in pH-buffer solutions with pH 1, 1.7, 4, 5, 7, 9, 10 and 13.

The sensitivity of the fabricated electrodes deviates from the ideal Nernstian response. This sub-Nernstian behavior is commonly observed for several (semiconducting) metal oxides and we similarly attribute this effect to electric double layer (e.g. local pH) and electronic structure modulation of the semi-conducting oxide due to proton adsorption at the surface [167,204,205].

It is assumed that the different pH sensing performance is caused by the structure and the thickness of the artificially grown oxide layer on the Nb wire. Therefore, SEM measurements were used to characterize the surface constitution of the different electrodes. Fig. 5.3a-c illustrates the texture of the oxide layer of the three electrodes. The SEM images revealed that the electrochemically produced electrodes (c) show the highest porosity, followed by the chemical one (b), whereas the thermally produced electrode (a) shows the densest oxide layer only a few, shallow cracks. The porous area fraction was determined optically and revealed that the electrochemical NbO_x electrode has the largest porous area fraction with 30 %, followed by the chemically produced NbO_x layer with 20 % and the thermally produced NbO_x layer with 6.5 %. The dense oxide layer of the thermally produced electrode causes a poor pH sensitivity of this electrode [206]. The investigations showed a correlation between the electrode performance and the texture of the NbO_x layer. This assumption is supported by the results of the electrochemical electrode, as it shows the best agreement between electrode sensitivity and oxide layer porosity.
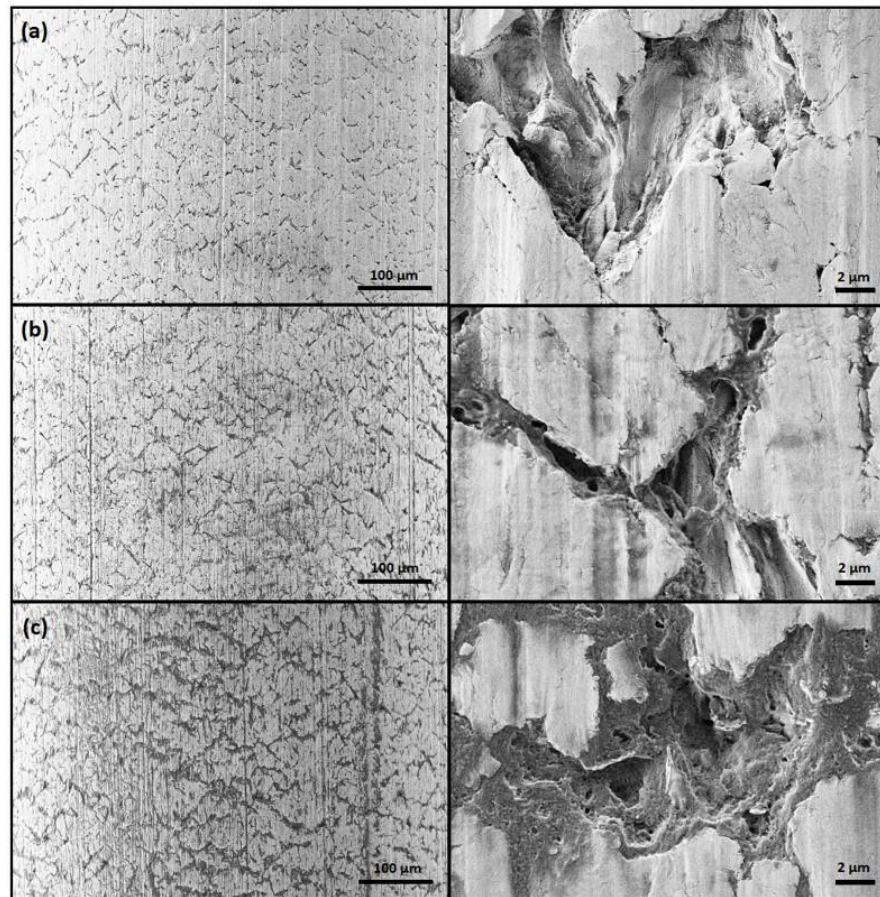
Figure 5.3: SEM images of a (a) thermally, (b) chemically and (c) electrochemically produced NbO$_x$ electrode surface.

In order to estimate the thickness of the oxide layer, SEM cross section measurements were carried out which are depicted in Fig 5.4a-c. The SEM cross section image of the thermally manufactured electrode (a) exhibits a dense oxide layer with a thickness variation of 3.4-5.0 µm. A thinner, but also dense oxide layer with a thickness of 1.0-2.0 µm grows on the Nb wire during the immersion in potassium permanganate shown in Fig. 5.4b. For the electrochemical variant (c), it can be seen that the oxide film does not grow continuously and is much thinner (0.2-1.0 µm).
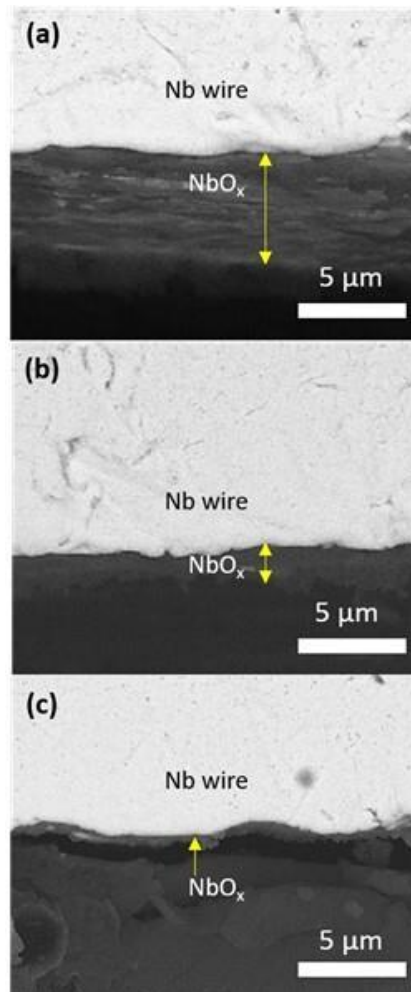
Figure 5.4: SEM cross section images of a (a) thermally, (b) chemically and (c) electrochemically produced NbO_x electrode.

In Table 5.1 the EDX results of the electrodes are summarized. EDX measurements showed that the oxygen and carbon content is higher for the electrochemically prepared electrode compared to the other two electrodes. The carbon content can be explained due to the formation of niobium carbides, whereas the oxygen resulted from the formation of NbO_x. In literature, it is described that Nb electrodes form in most aqueous solutions a Nb_2O_5 film during anodic polarization, which can be used for dielectric applications [200].

Furthermore, Teixeira da Silva *et al.* showed that the formed Nb_2O_5 tends to be

80

converted into conductive niobium carbides, which explains the high carbon concentrations detected in EDX measurements [207,208]. The zirconium and tantalum values emerge from the extraction process of pure niobium, as these occur as accompanying elements [209,210].

Table 5.1: EDX results of the three electrodes.

Element	Thermal NbO_x layer (wt%)	Chemical NbO_x layer (wt%)	Electrochemical NbO_x layer (wt%)
Nb	85.9	82.0	72.1
C	7.5	11.7	20.1
O	4.6	4.2	5.9
Zr	1.6	1.6	1.4
Ta	0.3	0.3	0.4

Additionally to SEM characterization of the oxide layer, EIS measurements were carried out. The results as well as the equivalent circuit for curve fitting are presented in Fig. 5.5. The equivalent circuit consisting of R_s, R_p and R_{ct} which are the resistances of the electrolyte solution, the pore and the charge transfer are illustrated. In addition, CPE_0 and CPE_{dl}, which are the constant phase elements of the oxide layer and the double layer are included in the equivalent circuit. To fit the EIS spectra, CPE were used instead of capacitors due to the non-ideal capacitance behaviours of the oxide film and the double layer [211,212]. Curve fitting allowed to estimate the pore resistance of each electrode. Fig. 5.5 (green curves) illustrates the EIS curve of the electrochemical electrode as well as the fitting result with a pore resistance of 2.65 x 10^5 Ω. The EIS curve of the thermal electrode (red curve) has a similar shape but with a much higher pore resistance of 1.90 x 10^6 Ω, which confirms a less porous oxide layer of the thermal electrode. The porosity of the chemical electrode (in purple in the EIS plot) with a pore resistance of 3.90 x 10^5 Ω is in between the two other electrode types, confirming the trend in porosity as observed in the SEM analyses. The values for the pore resistance of the oxide layers are generally in good agreement with values found in literature [213,214]. Generally, it was

observed that a higher porosity with a higher surface to volume ratio has an effect on the sensitivity of pH electrodes [167]. A similar effect could be found in the present study.
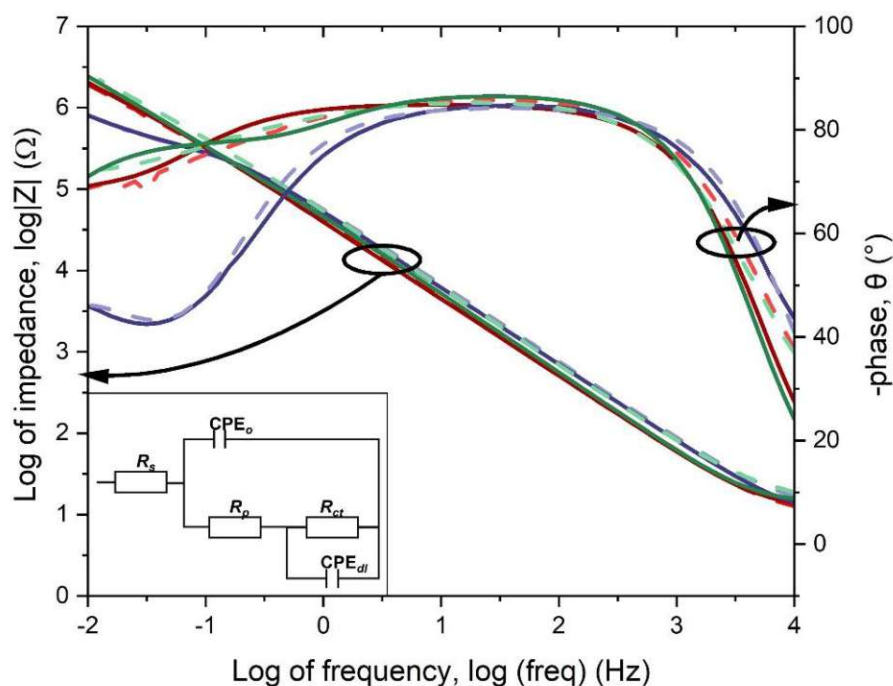
Figure 5.5: EIS measurements of (green) electrochemically, (red) thermally and (purple) chemically produced NbO_x electrodes with the equivalent circuit for curve fitting.

5.3.2 pH response

In order to investigate the pH sensing performance of the electrochemically produced NbO_x electrode, acid-base titration was done. Experiments proofed that preconditioning of the electrode in alkaline solution is necessary for faster response. In Fig. 4.6a the titration curve from pH 12 to 1 is depicted. pH 13 is not included because the reaction times and stability varied widely. Good response times, for about several seconds could be achieved for pH 1.0, 9.0 and 11.8. pH 4.0 and 11.0 were reached in 1.5 min, pH 1.8, 3.0 and 9.9 in less than 3 min. Longer response times were recorded in the near-neutral region with up

to 7 min for pH 7 and 7.8. Reaching pH 5.0 and 6.1 took up to 12.5 min, which were the maximum in response time observed. As illustrated in Fig. 5.6b, good linearity was reached in pH range 1-12 despite the longer response times of the previous mentioned pH values.
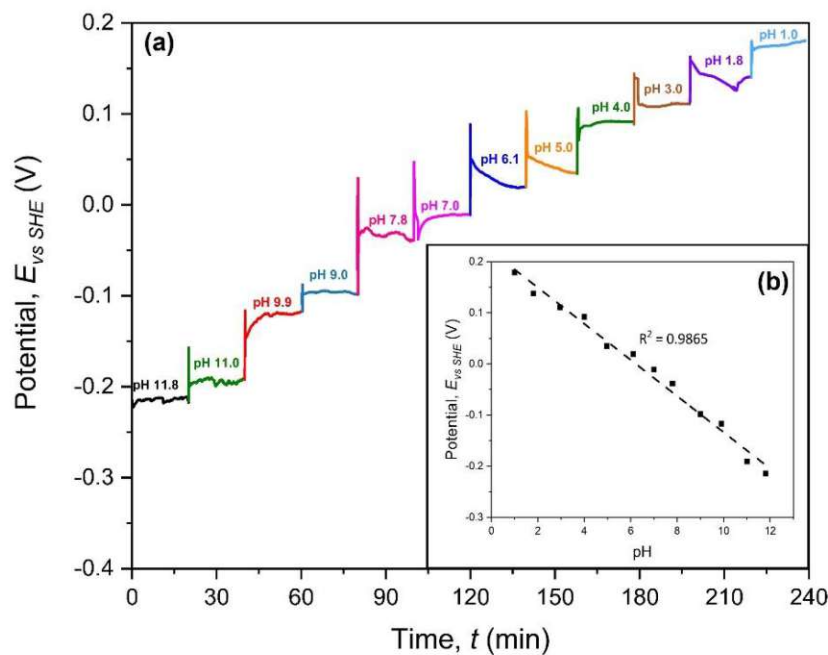
Figure 5.6: Titration curve of 1 M NaOH with 1 M HCl using an electrochemically produced NbO$_x$ electrode, (a) titration curve from pH 12-1 and (b) electrode potential versus pH obtained from the titration curve.

The Pourbaix diagram of the niobium-water system at 25 °C describes that Nb$_2$O$_5$ should be stable and pH sensitive between pH 1-13. As previously shown in the OCP measurements, the electrodes are often unstable at pH 1 and 13, this may be due to the fact that at very low pH Nb$_2$O$_5$ can be converted to niobic acid or at very high pH to niobates [215]. In order to confirm this hypothesis further investigations are planned in the future.

Fig. 5.7 illustrates the hysteresis measurement of the electrochemically

83

produced NbO$_x$ pH electrode with a pH loop of pH 7-4-7-10-7 for up to 1500 s. The obtained hysteresis voltage was very low with 2 mV.
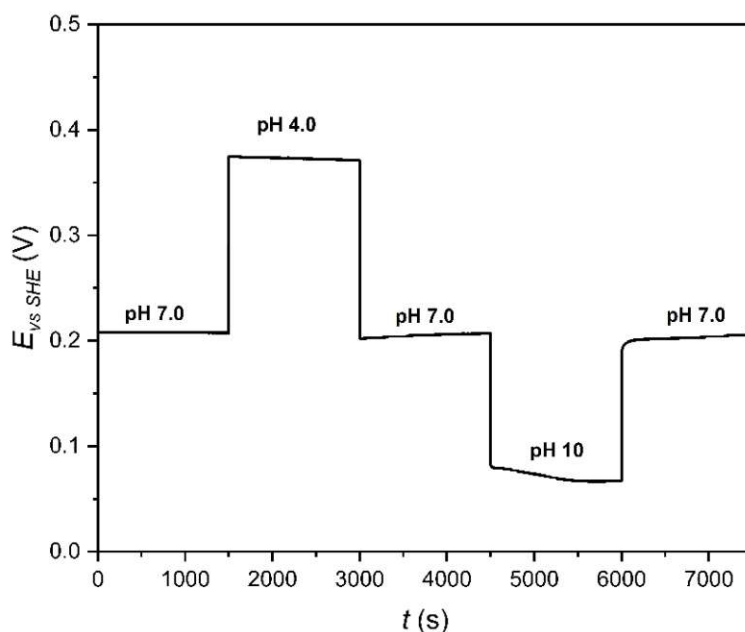
Figure 5.7: Hysteresis measurement of the electrochemically produced NbO$_x$ pH electrode with a pH loop of pH 7-4-7-10-7.

In a long term OCP measurement in pH 7 buffer solution the potential drift of the pH sensor was determined to 1.1 mV/h, which is in a similar region as several other metal oxide pH sensors described in literature [167].

Additionally, the effect of alkali metal ions was analyzed by adding either LiCl, NaCl or KCl to the buffer solutions with pH 4, 7 and 10. For NaCl and KCl containing solutions, the linearity and response of the pH electrode was not affected. The slopes of the calibration curves were -49.7 mV/pH for NaCl containing solutions and -50.2 mV/pH for KCl containing solutions. In case of LiCl slight interference was observed causing deviation from linear behavior and decreased sensitivity of -32.7 mV/pH. This can be due to interaction of Nb$_2$O$_5$ with Li ions [216].

5.3.3 Evaluation of different storage conditions and their influence on the stability of NbO$_x$ electrodes

Since it is important to produce reliable and robust electrodes, the stability over several months of the electrochemically produced electrodes was evaluated. Furthermore, different storage conditions were tested including dry storage over silica gel, storage in laboratory air, in 3 M KCl solution and 5 wt% NaCl solution. In Fig. 5.8 the OCP results over four months for the four different storage methods are summarized and compared. Keeping the electrode dry, Fig. 5.8a, revealed that for the first three months the sensitivity of the electrode remained stable with a sensitivity between -40 and -50 mV/pH. Afterwards, the slope of the curve decreased and the sensitivity halved compared to the initial values and was not stable anymore. The behavior of the electrode, which was stored under laboratory conditions, Fig. 5.8b, was better compared to the first storage method, because the decline in sensitivity was less compared to the first storage method. Immersing the electrode in 3 M KCl and 5 wt% NaCl, as shown in Fig. 5.8c and d, illustrates that the electrode is still stable after four months with almost no change in sensitivity. An advantage of the stability in NaCl solution is, that a lot of corrosion tests are performed in NaCl environment. Therefore, one possible application of this electrode can be the monitoring of pH changes during corrosion processes. The results indicate that the electrodes can be stored either under laboratory conditions or immersed in salt solutions like 3 M KCl and 5 wt% NaCl over several months. Whereas the storage under dry conditions only allows a storage for three months.
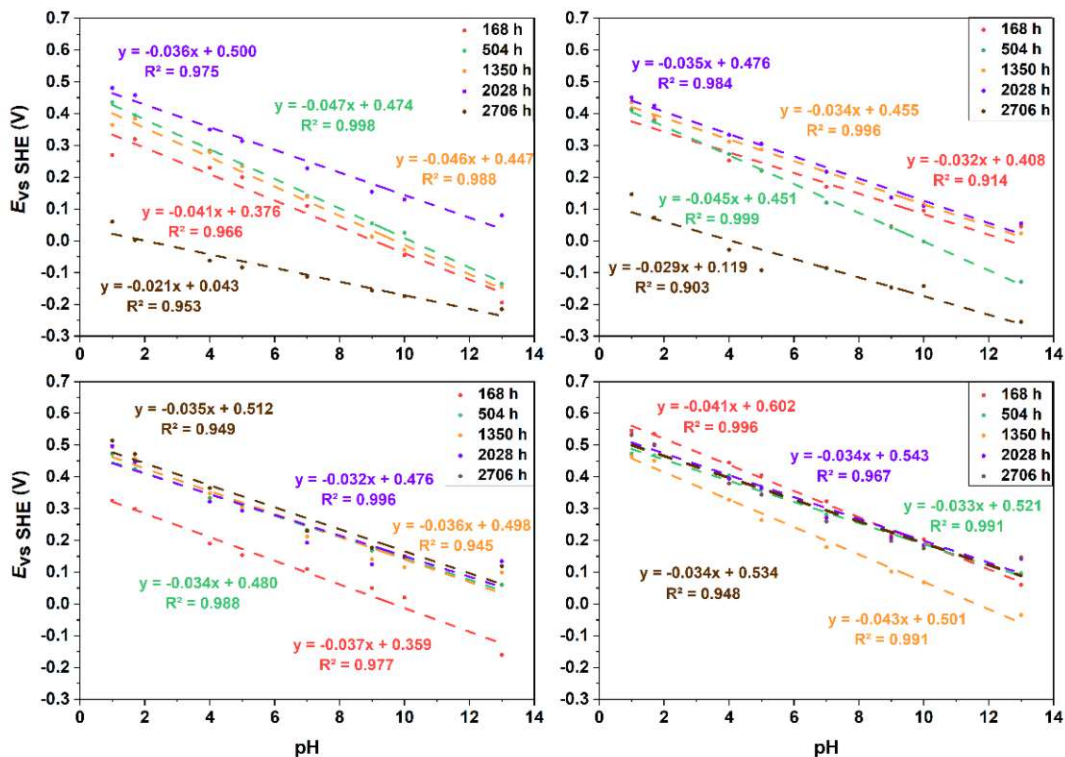
Figure 5.8: Potential-pH dependency of four different electrochemically produced NbO$_x$ electrodes stored dry over silica gel (a), under laboratory conditions (b), in 3 M KCl solution (c) or in 5 wt% NaCl solution (d) for up to 4 months.

5.4   Conclusions

In the present study, a robust, low-cost pH sensor based on niobium/niobium oxide was developed. Different manufacturing routes were examined, revealing the electrochemical production variant, involving anodic polarization, as optimum to produce electrodes with a linear potential-pH correlation in a wide pH range from pH 2-12 in buffer solutions with a sensitivity of -41 mV/pH. The superior sensitivity of these electrodes compared to the chemically and thermally produced niobium oxide electrodes could be linked to the highest porous area fraction of 30 % (versus 20 % chemical route, 7 % thermal oxidation). The storage stability of the electrodes was tested under various conditions and over a period of several months. It was

shown that the electrodes can be stored in KCl, NaCl or even dry in laboratory air over 3 months without a noticeable drop in sensitivity. Long-term measurements showed a drift at pH 7 of 1.1 mV/h.

Our results demonstrate that the produced niobium/niobium oxide sensor, which is chemically stable at various conditions and physiologically inert, can be used as a pH electrode and is a promising sensor material for many applications, such as in situ pH monitoring in corrosion testing or biological systems.

88

Chapter 6

Conclusion and Outlook

> The conclusions mentioned in this section are of general nature. The more specific findings from each study can be found at the end of the related chapters.

In this work, a comprehensive approach is taken involving electrochemical techniques, corrosion tests and the invention of a suitable MO_x pH sensing material to investigate the pH values at the interface between adhesive and galvanized steel surfaces or for in-situ corrosion monitoring. EIS and HR-SKP were found to be excellent for studying commercial adhesives as well as model formulations and were therefore used throughout this thesis.

EIS proved to be an excellent method for our sample systems and for addressing the questions of this dissertation and thus became a key method. An extensive literature review revealed numerous publications investigating water uptake in epoxy coatings and its effects on interfacial delamination processes via EIS. In contrast to previous publications, in this PhD thesis it was shown for the first time that EIS can be used to study commercially available adhesives with additives and not only simplified adhesive systems without additives. For example, with EIS the water uptake in HGMs, which are important lightweight fillers for structural adhesives, could be estimated. At a later stage, EIS, in particular the effective water diffusion coefficient obtained from these measurements, was used to assess the influence of commonly used inorganic additives in the adhesive on interfacial delamination processes. To sum up, it could be shown that EIS is deservedly

a fundamental method for investigating organic coated metals. One disadvantage of EIS, however, is that an open sample geometry is used instead of closed joints. This sample geometry is more commonly used when assessing the delamination behaviour of coatings such as paints and less often for adhesives. It is important to note therefore that this allows both water and atmospheric gases to reach the interface through the coating and not just through the exposed edges as would be the case with a closed joint geometry. To measure water that only penetrates from the side, SKP measurements are suitable, as shown in Chapter 3. In the course of this PhD thesis, however, the determination of the water diffusion coefficient was not performed due to time constraints. Here, the SKP was only used to measure the electrochemical delamination processes on different galvanized steel samples. Another advantage of the SKP is that this method is non-destructive and the interface could be measured without exposing it to the environment. The knowledge gained from the measurements helped to gain a better understanding of the interfacial processes between and to assess the results of numerous corrosion and ageing tests done during the PhD thesis.

Finally, to complete the work and obtain more information in future studies about the reactions taking place at the interface, a pH sensor material was searched that was stable enough to be embedded in the adhesive later on. Within the framework of the PhD thesis, a robust, low-cost pH sensor based on niobium/niobium oxide was successfully developed. In order to be able to determine the pH value at the interface, the electrode must be scaled down to a micro pH electrode and cured together with the adhesive. Promising preliminary work was done in this dissertation. However, the fabrication of micro pH electrodes could not be completed in time and is planned for future work.

Bibliography

[1] G. Savage, Failure prevention in bonded joints on primary load bearing structures, Engineering Failure Analysis 14 (2) (2007) 321–348. https://doi.org/10.1016/j.engfailanal.2005.11.013.

[2] F. Cavezza, M. Boehm, H. Terryn, T. Hauffman, A review on adhesively bonded aluminium joints in the automotive industry, Metals 10 (6) (2020) 730. https://doi.org/10.3390/met10060730.

[3] M.D. Banea, M. Rosioara, R.J.C. Carbas, L.F.M. da Silva, Multi-material adhesive joints for automotive industry, Composites Part B: Engineering 151 (2018) 71–77. https://doi.org/10.1016/j.compositesb.2018.06.009.

[4] U.T. Kreibich, A.F. Marcantonio, New developments in structural adhesives for the automotive industry, The Journal of Adhesion 22 (2) (1987) 153–165. https://doi.org/10.1080/00218468708074998.

[5] B. Täljsten, The importance of bonding — A historic overview and future possibilities, Advances in Structural Engineering 9 (6) (2006) 721–736. https://doi.org/10.1260/136943306779369509.

[6] A.L. Loureiro, L.F.M. da Silva, C. Sato, M.A.V. Figueiredo, Comparison of the mechanical behaviour between stiff and flexible adhesive joints for the automotive industry, The Journal of Adhesion 86 (7) (2010) 765–787. https://doi.org/10.1080/00218464.2010.482440.

[7] A. Mubashar, I.A. Ashcroft, G.W. Critchlow, A.D. Crocombe, Moisture absorption–desorption effects in adhesive joints, International Journal of Adhesion and Adhesives 29 (8) (2009) 751–760. https://doi.org/10.1016/j.ijadhadh.2009.05.001.

[8] M.R. Bowditch, The durability of adhesive joints in the presence of water, International Journal of Adhesion and Adhesives 16 (2) (1996) 73–79. https://doi.org/10.1016/0143-7496(96)00001-2.

[9] T.S. Ellis, F.E. Karasz, Interaction of epoxy resins with water: the depression of glass transition temperature, Polymer 25 (5) (1984) 664–669. https://doi.org/10.1016/0032-3861(84)90034-X.

[10] A.W. Momber, L. Fröck, T. Marquardt, Effects of accelerated ageing on the mechanical properties of adhesive joints between stainless steel and polymeric top coat materials for marine applications, International Journal of Adhesion and Adhesives 103 (2020) 102699. https://doi.org/10.1016/j.ijadhadh.2020.102699.

[11] G.Z. Xiao, M.E.R. Shanahan, Swelling of DGEBA/DDA epoxy resin during hygrothermal ageing, Polymer 39 (14) (1998) 3253–3260. https://doi.org/10.1016/S0032-3861(97)10060-X.

[12] R. Posner, K. Wapner, S. Amthor, K.J. Roschmann, G. Grundmeier, Electrochemical investigation of the coating/substrate interface stability for styrene/acrylate copolymer films applied on iron, Corrosion Science 52 (1) (2010) 37–44. https://doi.org/10.1016/j.corsci.2009.08.038.

[13] T.D. Singewald, T.M. Bruckner, R. Gruber, G. Schimo-Aichhorn, L. Hader-Kregl, S. Pöller, M. Müller, C. Kern, G. Luckeneder, K.-H. Stellnberger, B. Strauß, M. Hafner, M. Valtiner, Water-uptake in hollow glass microspheres and their influence on cathodic and anodic delamination along the polymer/metal-interface, Corrosion Science 196 (2022) 110045. https://doi.org/10.1016/j.corsci.2021.110045.

[14] M.K. Budzik, M. Wolfahrt, P. Reis, M. Kozłowski, J. Sena-Cruz, L. Papadakis, M. Nasr Saleh, K.V. Machalicka, S. Teixeira de Freitas, A.P. Vassilopoulos, Testing mechanical performance of adhesively bonded composite joints in

engineering applications: an overview, The Journal of Adhesion (2021) 1–77. https://doi.org/10.1080/00218464.2021.1953479.

[15] S. Deng, L. Djukic, R. Paton, L. Ye, Thermoplastic–epoxy interactions and their potential applications in joining composite structures – A review, Composites Part A: Applied Science and Manufacturing 68 (2015) 121–132. https://doi.org/10.1016/j.compositesa.2014.09.027.

[16] K.W. Allen, A review of contemporary views of theories of adhesion, The Journal of Adhesion 21 (3-4) (1987) 261–277. https://doi.org/10.1080/00218468708074974.

[17] F. Awaja, M. Gilbert, G. Kelly, B. Fox, P.J. Pigram, Adhesion of polymers, Progress in Polymer Science 34 (9) (2009) 948–968. https://doi.org/10.1016/j.progpolymsci.2009.04.007.

[18] W.C. Wake, Theories of adhesion and uses of adhesives: a review, Polymer 19 (3) (1978) 291–308. https://doi.org/10.1016/0032-3861(78)90223-9.

[19] D.E. Packham, C. Johnston, Mechanical adhesion: were McBain and Hopkins right? An empirical study, International Journal of Adhesion and Adhesives 14 (2) (1994) 131–135. https://doi.org/10.1016/0143-7496(94)90008-6.

[20] S.J. Marshall, S.C. Bayne, R. Baier, A.P. Tomsia, G.W. Marshall, A review of adhesion science, Dental Materials 26 (2) (2010) e11-e16. https://doi.org/10.1016/j.dental.2009.11.157.

[21] D.E. Packham, The mechanical theory of adhesion—Changing perceptions 1925-1991, The Journal of Adhesion 39 (2-3) (1992) 137–144. https://doi.org/10.1080/00218469208026545.

[22] C.M.H. Hagen, A. Hognestad, O.Ø. Knudsen, K. Sørby, The effect of surface

93

roughness on corrosion resistance of machined and epoxy coated steel, Progress in Organic Coatings 130 (2019) 17–23. https://doi.org/10.1016/j.porgcoat.2019.01.030.

[23] V.E. Basin, Advances in understanding the adhesion between solid substrates and organic coatings, Progress in Organic Coatings 12 (3) (1984) 213–250. https://doi.org/10.1016/0033-0655(84)80010-2.

[24] N. Naat, Y. Boutar, S. Naïmi, S. Mezlini, L. Filipe, Effect of surface texture on the mechanical performance of bonded joints: a review, The Journal of Adhesion (2021) 1–93. https://doi.org/10.1080/00218464.2021.2008370.

[25] W.-S. Kim, I.-H. Yun, J.-J. Lee, H.-T. Jung, Evaluation of mechanical interlock effect on adhesion strength of polymer–metal interfaces using micro-patterned surface topography, International Journal of Adhesion and Adhesives 30 (6) (2010) 408–417. https://doi.org/10.1016/j.ijadhadh.2010.05.004.

[26] G. Fourche, An overview of the basic aspects of polymer adhesion. Part I: Fundamentals, Polymer Engineering & Science 35 (12) (1995) 957–967. https://doi.org/10.1002/pen.760351202.

[27] R.D. Adams, Adhesive bonding: science, technology and applications, Woodhead Publishing, pp. 35-41, United Kingdom, 2005.

[28] C.M. Roth, B.L. Neal, A.M. Lenhoff, Van der Waals interactions involving proteins, Biophysical Journal 70 (2) (1996) 977–987. https://doi.org/10.1016/S0006-3495(96)79641-8.

[29] K.L. Mittal, The role of the interface in adhesion phenomena, Polymer Engineering & Science 17 (7) (1977) 467–473. https://doi.org/10.1002/pen.760170709.

[30] E. McCafferty, Lewis acid/lewis base effects in corrosion and polymer adhesion at aluminum surfaces, Journal of The Electrochemical Society 150 (7) (2003) B342. https://doi.org/10.1149/1.1580135.

[31] S.S. Voyutskiĭ, The diffusion theory of adhesion, Rubber Chemistry and Technology 33 (3) (1960) 748–756. https://doi.org/10.5254/1.3542193.

[32] A. Baldan, Adhesively-bonded joints and repairs in metallic alloys, polymers and composite materials: Adhesives, adhesion theories and surface pretreatment, Journal of materials science 39 (2004) 1–49. https://doi.org/10.1023/B:JMSC.0000007726.58758.e4.

[33] F. Jörg, Metal-polymer systems: interface design and chemical bonding, John Wiley & Sons, pp. 52-54, Germany, 2017.

[34] S. Morsch, S. Lyon, P. Greensmith, S.D. Smith, S.R. Gibbon, Mapping water uptake in organic coatings using AFM-IR, Faraday discussions 180 (2015) 527–542. https://doi.org/10.1039/C4FD00229F.

[35] E. McCafferty, Corrosion under organic coatings, in: Introduction to Corrosion Science, Springer Science+Buisness Media LLC, NY, 2010, pp. 403-425.

[36] N.S. Sangaj, V.C. Malshe, Permeability of polymers in protective organic coatings, Progress in Organic Coatings 50 (2004) 28–39. https://doi.org/10.1016/j.porgcoat.2003.09.015.

[37] W. Fürbeth, M. Stratmann, The delamination of polymeric coatings from electrogalvanised steel – a mechanistic approach. Part 1: delamination from a defect with intact zinc layer, Corrosion Science 43 (2) (2001) 207–227. https://doi.org/10.1016/S0010-938X(00)00047-0.

[38] K. Ogle, S. Morel, N. Meddahi, An electrochemical study of the delamination of

polymer coatings on galvanized steel, Corrosion Science 47 (8) (2005) 2034–2052.

[38] K. Ogle, S. Morel, N. Meddahi, An electrochemical study of the delamination of polymer coatings on galvanized steel, Corrosion Science 47 (8) (2005) 2034–2052. https://doi.org/10.1016/j.corsci.2004.08.017.

[39] G. Grundmeier, W. Schmidt, M. Stratmann, Corrosion protection by organic coatings: electrochemical mechanism and novel methods of investigation, Electrochimica Acta 45 (15-16) (2000) 2515–2533. https://doi.org/10.1016/S0013-4686(00)00348-0.

[40] W. Funke, Toward a unified view of the mechanism responsible for paint defects by metallic corrosion, Industrial & Engineering Chemistry Product Research and Development 24 (3) (1985) 343–347. https://doi.org/10.1021/i300019a001.

[41] H. Leidheiser, Corrosion of painted metals — a review, Corrosion 38 (7) (1982) 374–383. https://doi.org/10.5006/1.3581899.

[42] H. Leidheiser W. Wang, L. Igetoft, The mechanism for the cathodic delamination of organic coatings from a metal surface, Progress in Organic Coatings 11 (1983) 19–40. https://doi.org/10.1016/0033-0655(83)80002-8.

[43] D. Gervasio, I. Song, J.H. Payer, Determination of the oxygen reduction products on ASTM A516 steel during cathodic protection, Journal of Applied Electrochemistry 28 (1998) 979–992. https://doi.org/10.1023/A:1003451418717.

[44] P.A. Sørensen, C.E. Weinell, K. Dam-Johansen, S. Kiil, Reduction of cathodic delamination rates of anticorrosive coatings using free radical scavengers, Journal of Coatings Technology and Research 7 (2010) 773–786. https://doi.org/10.1007/s11998-010-9267-0.

[45] R. Posner, N. Fink, M. Wolpers, G. Grundmeier, Electrochemical electrolyte spreading studies of the protective properties of ultra-thin films on zinc galvanized steel, Surface and Coatings Technology 228 (2013) 286–295. https://doi.org/10.1016/j.surfcoat.2013.04.042.

[46] H. Leidheiser, Corrosion of painted metals—a review, CORROSION 38 (7) (1982) 374–383. https://doi.org/10.5006/1.3581899.

[47] A. Bautista, Filiform corrosion in polymer-coated metals, Progress in Organic Coatings 28 (1) (1996) 49–58. https://doi.org/10.1016/0300-9440(95)00555-2.

[48] N. Wint, D. Eaves, E. Michailidou, A. Bennett, J.R. Searle, G. Williams, H.N. McMurray, The kinetics and mechanism of filiform corrosion occurring on zinc-aluminium-magnesium coated steel, Corrosion Science 158 (2019) 108073. https://doi.org/10.1016/j.corsci.2019.06.028.

[49] N. Wint, Z.S. Barrett, H.N. McMurray, G. Williams, Combinatorial studies into the effect of thermally inter-diffused magnesium on the kinetics of organic coating cathodic delamination from zinc galvanized steel, Journal of the Electrochemical Society 167 (2) (2020) 21502. https://doi.org/10.1149/1945-7111/ab6289.

[50] C.F. Sharman, Filiform under film corrosion of lacquered steel surfaces, Nature 153 (1944) 621–622. https://doi.org/10.1038/153621a0.

[51] T.M. Watson, A.J. Coleman, G. Williams, H.N. McMurray, The effect of oxygen partial pressure on the filiform corrosion of organic coated iron, Corrosion Science 89 (2014) 46–58. https://doi.org/10.1016/j.corsci.2014.08.004.

[52] W. Funke, Toward a unified view of the mechanism responsible for paint defects by metallic corrosion, Industrial & Engineering Chemistry Product Research and Development 24 (3) (1985) 343–347. https://doi.org/10.1021/i300019a001.

[53] C.H. Hare, Blistering of paint films on metal, Part I: Osmotic blistering, Journal of Protective Coatings and Linings 15 (2) (1998) 45–63.

[54] F.A. Pfaff, F.S. Gelfant, Osmotic blistering of epoxy coatings on concrete, Journal of Protective Coatings and Linings 14 (1997) 52–65.

[55] S. Pletincx, L.L.I Fockaert, J.M.C. Mol, T. Hauffman, H. Terryn, Probing the formation and degradation of chemical interactions from model molecule/metal oxide to buried polymer/metal oxide interfaces, npj Materials Degradation 3 (2019) 23. https://doi.org/10.1038/s41529-019-0085-2.

[56] F. Cavezza, S. Pletincx, R.I. Revilla, J. Weaytens, M. Boehm, H. Terryn, Herman, T. Hauffman, Probing the metal oxide/polymer molecular hybrid interfaces with nanoscale resolution using AFM-IR, The Journal of Physical Chemistry C 123 (43) (2019) 26178–26184. https://doi.org/10.1021/acs.jpcc.9b04522.

[57] Y.-Y. Chen, B.-Y. Yu, W.-B. Wang, M.-F. Hsu, W.-C. Lin, Y.-C. Lin, J.-H. Jou, J.-J. Shyue, X-ray photoelectron spectrometry depth profiling of organic thin films using C60 sputtering, Analytical Chemistry 80 (2) (2008) 501–505. https://doi.org/10.1021/ac701899a.

[58] K. Marcoen, M. Gauvin, J. de Strycker, H. Terryn, T. Hauffman, Molecular characterization of bonding interactions at the buried steel oxide–aminopropyl triethoxysilane interface accessed by Ar cluster sputtering, The Journal of Physical Chemistry C 124 (24) (2020) 13150–13161. https://doi.org/10.1021/acs.jpcc.0c01523.

[59] S.J. Hinder, J.F. Watts, C. Lowe, Interface analysis and compositional depth profiling by XPS of polymer coatings prepared using ultra-low-angle microtomy, Surface and Interface Analysis 36 (8) (2004) 1032–1036. https://doi.org/10.1002/sia.1830.

[60] M.-L. Abel, J. F. Watts, Examination of the interface of a model adhesive joint by

98

surface analysis: a study by XPS and ToF-SIMS, Surface and Interface Analysis 41 (6) (2009) 508–516. https://doi.org/10.1002/sia.3055

[61] T. Greunz, B. Strauß, S. E. Schausberger, B. Heise, B. Jachs, D. Stifter, Cryo ultra-low-angle microtomy for XPS-depth profiling of organic coatings, Analytical and Bioanalytical Chemistry 405 (22) (2013) 7153–7160. https://doi.org/10.1007/s00216-013-6894-1.

[62] J. van den Brand, O. Blajiev, P.C.J. Beentjes, H. Terryn, J.H.W. de Wit, Interaction of anhydride and carboxylic acid compounds with aluminum oxide surfaces studied using infrared reflection absorption spectroscopy, Langmuir 20 (15) (2004) 6308–6317. https://doi.org/10.1021/la0496845.

[63] P. Taheri, J.H.W. Wit, H. Terryn, J.M.C. Mol, In situ study of buried metal–polymer interfaces exposed to an aqueous solution by an integrated ATR-FTIR and electrochemical impedance spectroscopy system, The Journal of Physical Chemistry C 117 (40) (2013) 20826–20832. https://doi.org/10.1021/jp409288a.

[64] M. Öhman, D. Persson, C. Leygraf, In situ ATR-FTIR studies of the aluminium/polymer interface upon exposure to water and electrolyte, Progress in Organic Coatings 57 (2006) 78–88. https://doi.org/10.1016/j.porgcoat.2006.07.002.

[65] M. Öhman, D. Persson ATR-FTIR Kretschmann spectroscopy for interfacial studies of a hidden aluminum surface coated with a silane film and epoxy II. Analysis by integrated ATR-FTIR and EIS during exposure to electrolyte with complementary studies by in situ ATR-FTIR and in situ IRRAS, Surface and Interface Analysis 44 (2012) 105–113. https://doi.org/10.1002/sia.3780.

[66] P. Nestor, Electrochemical Corrosion, in: Electrochemistry and Corrosion Science, Springer International Publishing, Cham, 2016, pp. 1–23.

[67] E. McCafferty, Getting started on the basics, in: Introduction to Corrosion Science, Springer Science+Buisness Media LLC, NY, 2010, pp. 13-31.

[68] G.A. Zhang, N. Yu, L.Y. Yang, X.P. Guo, Galvanic corrosion behavior of deposit-covered and uncovered carbon steel, Corrosion Science 86 (2014) 202–212. https://doi.org/10.1016/j.corsci.2014.05.011.

[69] Z. Ahmad, Chapter 2 - Basic concepts in corrosion, in: Zaki Ahmad (Ed.), Principles of Corrosion Engineering and Corrosion Control, Butterworth-Heinemann, Oxford, 2006, pp. 9–56.

[70] R.A.M. Anaee, Thermodynamic and kinetic study for corrosion of Al-Si-Cu/Y2O3 composites, Asian Journal of Chemistry 26 (14) (2014) 4469–4474. https://doi.org/10.14233/ajchem.2014.17005.

[71] M. Pourbaix, Atlas of electrochemical equilibria in aqueous solution, second Edition, NACE International Cebelcor, Houston, Texas, 1974.

[72] M. Rohwerder, F. Turcu, High-resolution Kelvin probe microscopy in corrosion science: Scanning Kelvin probe force microscopy (SKPFM) versus classical scanning Kelvin probe (SKP), Electrochimica Acta 53 (2) (2007) 290–299. https://doi.org/10.1016/j.electacta.2007.03.016.

[73] A. Nazarov, D. Thierry, Application of scanning Kelvin probe in the study of protective paints, Frontiers in Materials 6 (2019). https://doi.org/10.3389/fmats.2019.00192.

[74] G. Schimo, New approaches in hydrogen sensing based on electrochemical techniques, Linz, 2016.

[75] G.S. Cole, A.M. Sherman, Light weight materials for automotive applications, Materials characterization 35 (1) (1995) 3–9. https://doi.org/10.1016/1044-5803(95)00063-1.

[76] R. Avendaño, R.J.C. Carbas, F.J.P. Chaves, M. Costa, L.D. Silva, A.A. Fernandes, Impact loading of single lap joints of dissimilar lightweight adherends bonded with a crash-resistant epoxy adhesive, Journal of engineering materials and technology 138 (4) (2016). https://doi.org/10.1115/1.4034204.

[77] A.L. Loureiro, L.F.D. Silva, C. Sato, M.A.V. Figueiredo, Comparison of the mechanical behaviour between stiff and flexible adhesive joints for the automotive industry, The Journal of Adhesion 86 (7) (2010) 765–787. https://doi.org/10.1080/00218464.2010.482440.

[78] Z. Ahmadi, Nanostructured epoxy adhesives: A review, Progress in Organic Coatings 135 (2019) 449– 453. https://doi.org/10.1016/j.porgcoat.2019.06.028.

[79] J.J. Suay, M.T. Rodríguez, K.A. Razzaq, J.J. Carpio, J.J. Saura, The evaluation of anticorrosive automotive epoxy coatings by means of electrochemical impedance spectroscopy, Progress in Organic Coatings 46 (2) (2003) 121–129. https://doi.org/10.1016/ S0300-9440(02)00219-9.

[80] W. Brostow, M. Dutta, P. Rusek, Modified epoxy coatings on mild steel: tribology and surface energy, European Polymer Journal 46 (11) (2010) 2181–2189. https://doi.org/10.1016/j.eurpolymj.2010.08.006.

[81] S.-J. Park, F.-L. Jin, C. Lee, Preparation and physical properties of hollow glass microspheres- reinforced epoxy matrix resins, Materials Science and Engineering: A 402 (1-2) (2005) 335–340. https://doi.org/10.1016/j.msea.2005.05.015.

[82] J.R.M. d'Almeida, S.N. Monteiro, The effect of the resin/hardener ratio on the compressive behavior of an epoxy system, Polymer testing 15 (4) (1996) 329–339. https://doi.org/10.1016/0142- 9418(95)00037-2.

[83] V.V. Budov, Hollow glass microspheres. Use, properties, and technology, Glass and ceramics 51 (7-8) (1994) 230–235. https://doi.org/10.1007/BF00680655.

[84] H. Awais, Y. Nawab, A. Anjang, H.M. Akil, M.S.Z. Abidin, Mechanical Properties of Continuous Natural Fibres (Jute, Hemp, Flax) Reinforced Polypropylene Composites Modified with Hollow Glass Microspheres, Fibers and Polymers 21 (9) (2020) 2076–2083. https://doi.org/10.1007/s12221-020-2260-z.

[85] X. Zhang, P. Wang, Y. Zhou, X. Li, E.-H. Yang, T.X. Yu, J. Yang, The effect of strain rate and filler volume fraction on the mechanical properties of hollow glass microsphere modified polymer, Composites Part B: Engineering 101 (2016) 53–63. https://doi.org/10.1016/j.compositesb.2016.06.079.

[86] C. Fan, J. Shi, K. Dilger, Water uptake and interfacial delamination of an epoxy-coated galvanized steel: An electrochemical impedance spectroscopic study, Progress in Organic Coatings 137 (2019) 105333. https://doi.org/10.1016/j.porgcoat.2019.105333.

[87] S. Popineau, C. Rondeau-Mouro, C. Sulpice-Gaillet, M.E.R. Shanahan, Free/bound water absorption in an epoxy adhesive, Polymer 46 (24) (2005) 10733–10740. https://doi.org/10.1016/j.polymer.2005.09.008.

[88] B. de Nève, M.E.R. Shanahan, Effects of humidity on an epoxy adhesive, International Journal of Adhesion and Adhesives 12 (3) (1992) 191–196. https://doi.org/10.1016/0143-7496(92)90053-X.

[89] S.G. Prolongo, G. del Rosario, A. Ureña, Comparative study on the adhesive properties of different epoxy resins, International Journal of Adhesion and Adhesives 26 (3) (2006) 125–132. https://doi.org/10.1016/j.ijadhadh.2005.02.004.

[90] K.C. Yung, B.L. Zhu, T.M. Yue, C.S. Xie, Preparation and properties of hollow glass microsphere-filled epoxy-matrix composites, Composites Science and Technology 69 (2) (2009) 260–264. https://doi.org/10.1016/j.compscitech.2008.10.014.

[91] N. Gupta, S. Priya, R. Islam, W. Ricci, Characterization of mechanical and electrical properties of epoxy-glass microballoon syntactic composites, Ferroelectrics 345 (1) (2006) 1–12. https://doi.org/10.1080/00150190601018002.

[92] O.A. Afolabi, K. Kanny, T.P. Mohan, Processing of hollow glass microspheres (HGM) filled epoxy syntactic foam composites with improved structural characteristics, Science and Engineering of Composite Materials 28 (1) (2021) 116–127. https://doi.org/10.1515/secm-2021-0011.

[93] M. Vahtrus, S. Oras, M. Antsov, V. Reedo, U. Mäeorg, A. Lõhmus, K. Saal, R. Lõhmus, Mechanical and thermal properties of epoxy composite thermal insulators filled with silica aerogel and hollow glass microspheres, Proceedings of the Estonian Academy of Sciences 66 (4) (2017) 339–346. https://doi.org/10.3176/proc.2017.4.03.

[94] M. Bahrami, Z. Ranjbar, R.A. Khosroshahi, Sh. Ashhari, Investigating corrosion protection properties of epoxy thermal insulators through cyclic corrosion test, Progress in Organic Coatings 113 (2017) 25–30. https://doi.org/10.1016/j.porgcoat.2017.07.021.

[95] J.-T. Zhang, J.-M. Hu, J.-Q. Zhang, C.-N. Cao, Studies of water transport behavior and impedance models of epoxy-coated metals in NaCl solution by EIS, Progress in Organic Coatings 51 (2) (2004) 145–151. https://doi.org/10.1016/j.porgcoat.2004.08.001.

[96] C. Yang, X. Xing, Z. Li, S. Zhang, A comprehensive review on water diffusion in polymers focusing on the polymer-metal interface combination, Polymers 12 (1) (2020) 138. https://doi.org/10.3390/polym12010138.

[97] D.M. Brasher, A.H. Kingsbury, Electrical measurements in the study of immersed paint coatings on metal. I. Comparison between capacitance and gravimetric methods of estimating water-uptake, Journal of Applied Chemistry 4 (2) (1954) 62–72. https://doi.org/10.1002/jctb.5010040202.

[98] A.S. Nguyen, N. Causse, M. Musiani, M.E. Orazem, N. Pébère, B. Tribollet, V. Vivier, Determination of water uptake in organic coatings deposited on 2024 aluminium alloy: Comparison between impedance measurements and gravimetry, Progress in Organic Coatings 112 (2017) 93–100. https://doi.org/10.1016/j.porgcoat.2017.07.004.

[99] X. Chen, S.F. Wen, T. Feng, X. Yuan, Z.F. Yue, Investigating an effective model to estimate the water diffusion coefficient of a hybrid polymer-oxide coating, Progress in Organic Coatings 141 (2020) 105548. https://doi.org/10.1016/j.porgcoat.2020.105548.

[100] C. Vosgien Lacombre, G. Bouvet, D. Trinth, S. Mallarino, S. Touzain, Effect of pigment and temperature onto swelling and water uptake during organic coating ageing, Progress in Organic Coatings 124 (2018) 249–255. https://doi.org/10.1016/j.porgcoat.2017.11.022.

[101] D. Zhang, H. Li, H. Qian, L. Wang, X. Li, Double layer water-borne heat insulation coatings containing hollow glass microspheres (HGMs), Pigment & Resin Technology 45 (5) (2016) 346–353. https://doi.org/10.1108/PRT-04-2015-0041.

[102] E. Legghe, E. Aragon, L. Bélec, A. Margaillan, D. Melot, Correlation between water diffusion and adhesion loss: Study of an epoxy primer on steel, Progress in Organic Coatings 66 (3) (2009) 276–280. https://doi.org/10.1016/j.porgcoat.2009.08.001.

[103] D. Olmos, R. López-Morón, J. González-Benito, The nature of the glass fibre surface and its effect in the water absorption of glass fibre/epoxy composites. The use of fluorescence to obtain information at the interface, Composites Science and Technology 66 (15) (2006) 2758–2768. https://doi.org/10.1016/j.compscitech.2006.03.004.

[104] A.T.A. Jenkins, R.D. Armstrong, The breakdown in the barrier properties of

organic coatings due to filiform corrosion, Corrosion Science 38 (7) (1996) 1147–1157. https://doi.org/10.1016/0010-938X(96)00009-1.

[105] M. Van Loo, D.D. Laiderman, R.R. Bruhn, Filiform Corrosion, Corrosion 9 (8) (1953) 277–283. https://doi.org/10.5006/0010-9312-9.8.277.

[106] R. Hausbrand, M. Stratmann, M. Rohwerder, Corrosion of zinc–magnesium coatings: Mechanism of paint delamination, Corrosion Science 51 (9) (2009) 2107–2114. https://doi.org/10.1016/j.corsci.2009.05.042.

[107] T. Prosek, D. Persson, J. Stoulil, D. Thierry, Composition of corrosion products formed on Zn–Mg, Zn–Al and Zn–Al–Mg coatings in model atmospheric conditions, Corrosion Science 86 (2014) 231–238. https://doi.org/10.1016/j.corsci.2014.05.016.

[108] P. Volovitch, C. Allely, K. Ogle, Understanding corrosion via corrosion product characterization: I. Case study of the role of Mg alloying in Zn–Mg coating on steel, Corrosion Science 51 (6) (2009) 1251–1262. https://doi.org/10.1016/j.corsci.2009.03.005.

[109] T.A. Keppert, G. Luckeneder, K.-H. Stellnberger, C. Commenda, G. Mori, H. Antrekowitsch, The effect of magnesium on the corrosion of hot-dip galvanized steel in chloride containing environments, Materials and Corrosion 65 (9) (2014) 871–880. https://doi.org/10.1002/maco.201307278.

[110] R.M. Souto, D.J. Scantlebury, Cathodic delamination of coil coatings produced with different Zn-based intermediate metallic layers, Progress in Organic Coatings 53 (1) (2005) 63–70. https://doi.org/10.1016/j.porgcoat.2005.01.008.

[111] R.P. Edavan, R. Kopinski, Corrosion resistance of painted zinc alloy coated steels, Corrosion Science 51 (10) (2009) 2429–2442. https://doi.org/10.1016/j.corsci.2009.06.028.

[112] M.H. Nazir, Z.A. Khan, K. Stokes, A unified mathematical modelling and simulation for cathodic blistering mechanism incorporating diffusion and fracture mechanics concepts, Journal of Adhesion Science and Technology 29 (12) (2015) 1200–1228. https://doi.org/10.1080/01694243.2015.1022496.

[113] C. Xu, K. Ramani, G. Kumar, Thermoplastic adhesive bonding of galvanized steel to polypropylene composite and its durability, International Journal of Adhesion and Adhesives 22 (3) (2002) 187–195. https://doi.org/10.1016/S0143-7496(01)00054-9.

[114] M.A. Hernández, F. Galliano, D. Landolt, Mechanism of cathodic delamination control of zinc-aluminum phosphate pigment in waterborne coatings, Corrosion Science 46 (9) (2004) 2281–2300. https://doi.org/10.1016/j.corsci.2004.01.009.

[115] K.A. Yasakau, S. Kallip, A. Lisenkov, M.G.S. Ferreira, M.L. Zheludkevich, Initial stages of localized corrosion at cut-edges of adhesively bonded Zn and Zn-Al-Mg galvanized steel, Electrochimica Acta 211 (2016) 126–141. https://doi.org/10.1016/j.electacta.2016.06.045.

[116] F. Thébault, B. Vuillemin, R. Oltra, C. Allely, K. Ogle, O. Heintz, Influence of magnesium content on the corrosion resistance of the cut-edges of Zn-Mg-coated steel, Corrosion Science 97 (2015) 100–106. https://doi.org/10.1016/j.corsci.2015.04.019.

[117] T. Prosek, A. Nazarov, A.L. Gac, D. Thierry, Coil-coated Zn-Mg and Zn-Al-Mg: Effect of climatic parameters on the corrosion at cut edges, Progress in Organic Coatings 83 (2015) 26–35. https://doi.org/10.1016/j.porgcoat.2015.01.023.

[118] M. Stratmann, H. Streckel, R. Feser, A new technique able to measure directly the delamination of organic polymer films, Corrosion Science 32 (4) (1991) 467–470. https://doi.org/10.1016/0010-938X(91)90126-A.

106

[119] A. Leng, H. Streckel, M. Stratmann, The delamination of polymeric coatings from steel. Part 1: Calibration of the Kelvinprobe and basic delamination mechanism, Corrosion Science 41 (3) (1998) 547–578. https://doi.org/10.1016/S0010-938X(98)00168-1.

[120] K. Wapner, G. Grundmeier, Scanning Kelvin probe measurements of the stability of adhesive/metal interfaces in corrosive environments, Advanced Engineering Materials 6 (3) (2004) 163–167. https://doi.org/10.1002/adem.200300579.

[121] K. Wapner, M. Stratmann, G. Grundmeier, In situ infrared spectroscopic and scanning Kelvin probe measurements of water and ion transport at polymer/metal interfaces, Electrochimica Acta 51 (16) (2006) 3303–3315. https://doi.org/10.1016/j.electacta.2005.09.024.

[122] A. Leng, H. Streckel, K. Hofmann, M. Stratmann, The delamination of polymeric coatings from steel Part 3: Effect of the oxygen partial pressure on the delamination reaction and current distribution at the metal/polymer interface, Corrosion Science 41 (3) (1998) 599–620. https://doi.org/10.1016/S0010-938X(98)00168-1. [

[123] T.D. Singewald, T.M. Bruckner, R. Gruber, G. Schimo-Aichhorn, L. Hader-Kregl, S. Andronescu, M. Klotz, M. Müller, C. Kern, M. Rosner, G. Luckeneder, K.-H. Stellnberger, B. Strauß, M. Hafner, M. Valtiner, Systematic variation of inorganic additives and their impact on interfacial delamination processes of automotive coating systems, Progress in Organic Coatings 173 (2022) 107172. https://doi.org/10.1016/j.porgcoat.2022.107172.

[124] L. Goglio, M. Rezaei, Degradation of epoxy-steel single lap joints immersed in water, The Journal of Adhesion 91 (8) (2015) 621–636. https://doi.org/10.1080/00218464.2014.948614.

[125] M.R. Bowditch, The durability of adhesive joints in the presence of water,

International Journal of Adhesion and Adhesives 16 (2) (1996) 73–79. https://doi.org/10.1016/0143-7496(96)00001-2.

[126] Y. Tu, J.K. Spelt, Blistering as a form of degradation in adhesive joints, The Journal of Adhesion 72 (3-4) (2000) 359–372. https://doi.org/10.1080/00218460008029290.

[127] S. Effendy, T. Zhou, H. Eichman, M. Petr, M.Z. Bazant, Blistering failure of elastic coatings with applications to corrosion resistance, Soft Matter 17 (41) (2021) 9480–9498. https://doi.org/10.1039/D1SM00986A.

[128] R.C.L. Tai, Z. Szklarska-Smialowska, Effect of fillers on the degradation of automotive epoxy adhesives in aqueous solutions, Journal of materials science 28 (22) (1993) 6205–6210. https://doi.org/10.1007/BF00365045.

[129] J. Cognard, Blistering of glass-epoxy amine adhesive joints in water vapour at high pressure. An indication of interfacial crumpling, The Journal of Adhesion 47 (1-3) (1994) 83–93. https://doi.org/10.1080/00218469408027091.

[130] A. Leng, H. Streckel, M. Stratmann, The delamination of polymeric coatings from steel. Part 1: Calibration of the Kelvinprobe and basic delamination mechanism, Corrosion Science 41 (3) (1998) 547–578. https://doi.org/10.1016/S0010-938X(98)00166-8.

[131] J. Rimsza, A. Ilgen, Water weakening of calcium oxide, The Journal of Physical Chemistry C 126 (22) (2022) 9493–9501. https://doi.org/10.1021/acs.jpcc.2c01343.

[132] H. Manzano, R.J.M. Pellenq, F.-J. Ulm, M.J. Buehler, A.C.T. van Duin, Hydration of calcium oxide surface predicted by reactive force field molecular dynamics, Langmuir 28 (9) (2012) 4187–4197. https://doi.org/10.1021/la204338m.

[133] A. Rudawska, M. Frigione, Cold-cured bisphenolic epoxy adhesive filled with low amounts of $CaCO_3$: Effect of the filler on the durability to aqueous environments, Materials 14 (6) (2021). https://doi.org/10.3390/ma14061324.

[134] F. Mustata, N. Tudorachi, D. Rosu, Thermal behavior of some organic/inorganic composites based on epoxy resin and calcium carbonate obtained from conch shell of Rapana thomasiana, Composites Part B: Engineering 43 (2) (2012) 702–710. https://doi.org/10.1016/j.compositesb.2011.11.047.

[135] N.A.N. Azman, M.R. Islam, M. Parimalam, N. M. Rashidi, M. Mupit, Mechanical, structural, thermal and morphological properties of epoxy composites filled with chicken eggshell and inorganic $CaCO_3$ particles, Polymer Bulletin 77 (2) (2020) 805–821. https://doi.org/10.1007/s00289-019-02779-y.

[136] I. O. Oladele, A.D. Akinwekomi, O.G. Agbabiaka, M.O. Oladejo, Influence of biodegradation on the tensile and wear resistance properties of bio-derived $CaCO_3$/epoxy composites, Journal of Polymer Research 26 (2018) 16. https://doi.org/10.1007/s10965-018-1676-2.

[137] M. Frigione, M.A. Aiello, C. Naddeo, Water effects on the bond strength of concrete/concrete adhesive joints, Construction and Building Materials 20 (10) (2006) 957–970. https://doi.org/10.1016/j.conbuildmat.2005.06.015.

[138] A. Rudawska, M. Frigione, Aging effects of aqueous environment on mechanical properties of calcium carbonate-modified epoxy resin, Polymers (Basel) 12 (11) (2020). https://doi.org/10.3390/polym12112541.

[139] H. Barthel, M. Dreyer, T. Gottschalk-Gaudig, V. Litvinov, E. Nikitina, Fumed silica – rheological additive for adhesives, resins, and paints, Macromolecular Symposia 187 (2002) 573–584. https://doi.org/10.1002/1521-3900(200209)187:1<573:AID-MASY573>3.0.CO;2-1.

[140] T.G. Maciá-Agulló, J.C. Fernández-García, A. Torró-Palau, A.C. Orgilés Barceló, J.M. Martín-Martínez, Hydrophobic or hydrophilic fumed silica as filler of polyurethane adhesives, The Journal of Adhesion 50 (4) (1995) 265–277. https://doi.org/10.1080/00218469508014557.

[141] G.S. Byrne, Adhesive formulations manipulated by the addition of fumed colloidal silica, Studies in Conservation 29 (sup1) (1984) 78–80. https://doi.org/10.1179/sic.1984.29.Supplement-1.78.

[142] A.M. Torró-Palau, J.C. Fernández-García, A. César Orgilés-Barceló, J.M. Martín-Martínez, Characterization of polyurethanes containing different silicas, International Journal of Adhesion and Adhesives 21 (2001) 1–9. https://doi.org/10.1016/S0143-7496(00)00021-X.

[143] L. Zhang, B. Zhang, Z. Yang, M. Guo, The role of water on the performance of calcium oxide-based sorbents for carbon dioxide capture: A review, Energy Technology 3 (2015) 10–19. https://doi.org/10.1002/ente.201402099.

[144] G. K. van der Wel, O.C.G. Adan, Moisture in organic coatings — a review, Progress in Organic Coatings 37 (1999) 1–14. https://doi.org/10.1016/S0300-9440(99)00058-2.

[145] G. Roventi, T. Bellezze, E. Barbaresi, R. Fratesi, Effect of carbonation process on the passivating products of zinc in $Ca(OH)_2$ saturated solution, Materials and Corrosion 64 (11) (2013) 1007–1014. https://doi.org/10.1002/maco.201206868.

[146] R.A. Sharma, Physico-chemical properties of calcium zincate, Journal of The Electrochemical Society 133 (11) (1986) 2215–2219. https://doi.org/10.1149/1.2108376.

[147] F. Ziegler, C.A. Johnson, The solubility of calcium zincate ($CaZn_2(OH)_6 \cdot 2H_2O$), Cement and Concrete Research 31 (9) (2001) 1327–1332. https://doi.org/10.1016/S0008-8846(01)00557-9.

[148] Y.-Q. Wang, G. Kong, C.-S. Che, T.-Y. Weng, Z.-W. Sun, Corrosion behavior of Zn-Mg alloys in saturated $Ca(OH)_2$ solution, Corrosion Science 136 (2018) 374–385. https://doi.org/10.1016/j.corsci.2018.03.032.

[149] H. Huang, X. Sheng, Y. Tian, L. Zhang, Y. Chen, X. Zhang, Two-dimensional nanomaterials for anticorrosive polymeric coatings: A review, Industrial & Engineering Chemistry Research 59 (35) (2020) 15424–15446. https://doi.org/10.1021/acs.iecr.0c02876.

[150] N.H. Othman, M.C. Ismail, M. Mustapha, N. Sallih, K.E. Kee, R.A. Jaal, Graphene-based polymer nanocomposites as barrier coatings for corrosion protection, Progress in Organic Coatings 135 (2019) 82–99. https://doi.org/10.1016/j.porgcoat.2019.05.030.

[151] S.S.A. Kumar, S. Bashir, K. Ramesh, S. Ramesh, New perspectives on graphene/graphene oxide based polymer nanocomposites for corrosion applications: The relevance of the graphene/polymer barrier coatings, Progress in Organic Coatings 154 (2021) 106215. https://doi.org/10.1016/j.porgcoat.2021.106215.

[152] V.P. Chacko, F.E. Karasz, R.J. Farris, E.L. Thomas, Morphology of $CaCO_3$-filled polyethylenes, Journal of Polymer Science: Polymer Physics Edition 20 (12) (1982) 2177–2195. https://doi.org/10.1002/pol.1982.180201202.

[153] N.G. Shimpi, S. Mishra, Ultrasonic-assisted synthesis of nano-$BaSO_4$ and its effect on thermal and cross-linking density of epoxy nanocomposites, Journal of Reinforced Plastics and Composites 32 (13) (2013) 947–954. https://doi.org/10.1177/0731684412462754.

[154] L. Ejenstam, A. Swerin, J. Pan, P.M. Claesson, Corrosion protection by hydrophobic silica particle-polydimethylsiloxane composite coatings, Corrosion Science 99 (2015) 89–97. https://doi.org/10.1016/j.corsci.2015.06.018.

[155] Sh. Ammar, K. Ramesh, B. Vengadaesvaran, S. Ramesh, A.K. Arof, A novel coating material that uses nano-sized SiO_2 particles to intensify hydrophobicity and corrosion protection properties, Electrochimica Acta 220 (2016) 417–426. https://doi.org/10.1016/j.electacta.2016.10.099.

[156] G. Li, J. Yue, C. Guo, Y. Ji, Influences of modified nanoparticles on hydrophobicity of concrete with organic film coating, Construction and Building Materials 169 (2018) 1–7. https://doi.org/10.1016/j.conbuildmat.2018.02.191.

[157] F. Dolatzadeh, M.M. Jalili, S. Moradian, Influence of various loadings of hydrophilic or hydrophobic silica nanoparticles on water uptake and porosity of a polyurethane coating, Materials and Corrosion 64 (7) (2013) 609–618. https://doi.org/10.1002/maco.201106381.

[158] N. LeBozec, D. Thierry, A. Peltola, L. Luxem, G. Luckeneder, G. Marchiaro, M. Rohwerder, Corrosion performance of Zn–Mg–Al coated steel in accelerated corrosion tests used in the automotive industry and field exposures, Materials and Corrosion 64 (11) (2013) 969–978. https://doi.org/10.1002/maco.201206959.

[159] N. LeBozec, D. Thierry, P. Le Calvé, C. Favennec, J.-P. Pautasso, C. Hubert, Performance of marine and offshore paint systems: Correlation of accelerated corrosion tests and field exposure on operating ships, Materials and Corrosion 66 (3) (2015) 215–225. https://doi.org/10.1002/maco.201307340.

[160] B. Andreon, B.L. Guenther, W.L. Cavalcanti, L. Colombi Ciacchi, P. Plagemann, On the use of scanning Kelvin probe for assessing in situ the delamination of adhesively bonded joints, Corrosion Science 157 (2019) 11–19. https://doi.org/10.1016/j.corsci.2019.03.001.

[161] T. D. Singewald, I. Traxler, G. Schimo-Aichhorn, S. Hild, M. Valtiner, Versatile, low-cost, non-toxic potentiometric pH-sensors based on niobium, Sensing and Bio-Sensing Research 35 (2022) 100478.

https://doi.org/10.1016/j.sbsr.2022.100478.

[162] E. Tada, K. Sugawara, H. Kaneko, Distribution of pH during galvanic corrosion of a Zn/steel couple, Electrochimica Acta 49 (7) (2004) 1019–1026. https://doi.org/10.1016/j.electacta.2003.10.012.

[163] J. J. Ritter, J. Kruger, A qualitative ellipsometric-electrochemical approach to the study of film growth under organic coatings, Surface Science 96 (1-3) (1980) 364-374. https://doi.org/10.1016/0039-6028(80)90314-3.

[164] R.-G. Du, R.-G. Hu, R.-S. Huang, C.-J. Lin, In situ measurement of Cl-concentrations and pH at the reinforcing steel/concrete interface by combination sensors, Analytical Chemistry 78 (9) (2006) 3179–3185. https://doi.org/10.1021/ac0517139.

[165] S.-G. Dong, C.-J. Lin, R.-G. Hu, L.-Q. Li, R.-G. Du, Effective monitoring of corrosion in reinforcing steel in concrete constructions by a multifunctional sensor, Electrochimica Acta 56 (4) (2011) 1881-1888. https://doi.org/10.1016/j.electacta.2010.08.089.

[166] Y. Seguí Femenias, U. Angst, B. Elsener, Monitoring pH in corrosion engineering by means of thermally produced iridium oxide electrodes, Materials and Corrosion 69 (1) (2018) 76-88. https://doi.org/10.1002/maco.201709715

[167] L. Manjakkal, D. Szwagierczak, R. Dahiya, Metal oxides based electrochemical pH sensors: Current progress and future perspectives, Progress in Materials Science 109 (2020) 100635. https://doi.org/10.1016/j.pmatsci.2019.100635.

[168] G. da Silva, S. G. Lemos, L. A. Pocrifka, P. D. Marreto, A. V. Rosario, E. C. Pereira, Development of low-cost metal oxide pH electrodes based on the polymeric precursor method, Analytica Chimica Acta 616 (1) (2008) 36-41.

113

https://doi.org/10.1016/j.aca.2008.03.019.

[169] Z. Zhu, Z. Ye, Q. Zhang, J. Zhang, F. Cao, Novel dual Pt-Pt/IrO$_x$ ultramicroelectrode for pH imaging using SECM in both potentiometric and amperometric modes, Electrochemistry Communications 88 (2018) 47-51. https://doi.org/10.1016/j.elecom.2018.01.018.

[170] M. Wang, S. Yao, M. Madou, A long-term stable iridium oxide pH electrode, Sensors and Actuators B: Chemical 81 (2-3) (2002) 313-315. https://doi.org/10.1016/S0925-4005(01)00972-8.

[171] Z. Zhou, J. Li, D. Pan, H. Wei, C. Wang, F. Pan, J. Xia, S. Ma, pH electrodes based on iridium oxide films for marine monitoring, Trends in Environmental Analytical Chemistry 25 (2020) e00083. https://doi.org/10.1016/j.teac.2020.e00083.

[172] A. Fog, R. P. Buck, Electronic semiconducting oxides as pH sensors, Sensors and Actuators 5 (2) (1984) 137-146. https://doi.org/10.1016/0250-6874(84)80004-9.

[173] K. Uppuluri, M. Lazouskaya, D. Szwagierczak, K. Zaraska, M. Tamm, Fabrication, Potentiometric characterization, and application of screen-printed RuO$_2$ pH electrodes for water quality testing, Sensors 21 (16) (2021) 5399. https://doi.org/10.3390/s21165399.

[174] L. Manjakkal, K. Cvejin, J. Kulawik, K. Zaraska, D. Szwagierczak, A low-cost pH sensor based on RuO$_2$ resistor material, in: Nano Hybrids, Vol. 5, 2013, pp. 1-15. https://doi.org/10.4028/www.scientific.net/NH.5.1.

[175] R. Zhao, M. Xu, J. Wang, G. Chen, A pH sensor based on the TiO$_2$ nanotube array modified Ti electrode, Electrochimica Acta 55 (20) (2010) 5647-5651. https://doi.org/10.1016/j.electacta.2010.04.102.

114

[176] S. Drensler, S. Walkner, C.C. Mardare, A.W. Hassel, On the pH-sensing properties of differently prepared tungsten oxide films, Physica Status Solidi A 211 (6) (2014) 1340-1345. https://doi.org/10.1002/pssa.201330376.

[177] J. Izquierdo, L. Nagy, Á. Varga, J. J. Santana, G. Nagy, R. M. Souto, Spatially resolved measurement of electrochemical activity and pH distributions in corrosion processes by scanning electrochemical microscopy using antimony microelectrode tips, Electrochimica Acta 56 (24) (2011) 8846–8850. https://doi.org/10.1016/j.electacta.2011.07.076.

[178] I. H. Kadhim, N.M. Abd-Alghafour, A novel pH sensitivity of SnO_2 thin film based EGFET prepared using chemical bath method, Surface Review and Letters 28 (9) (2021) 2150074. https://doi.org/10.1142/S0218625X21500748.

[179] B. Seo, H. Hwang, S. Park, W. Choi, A simple fabrication route of porous palladium/palladium oxide/carbon nanostructures using one-step combustion waves for high-performance pH sensors, Sensors and Actuators B: Chemical 274 (2018) 37-46. https://doi.org/10.1016/j.snb.2018.07.142.

[180] A. Cranny, N.R. Harris, M. Nie, J.A. Wharton, R.J.K. Wood, K.R. Stokes, Sensors for corrosion detection: Measurement of copper ions in 3.5 % sodium chloride using screen-printed platinum electrodes, IEEE Sensors Journal 12 (6) 2012-2099. https://10.1109/JSEN.2012.2183867.

[181] L.A. Pocrifka, C. Gonçalves, P. Grossi, P.C. Colpa, E.C. Pereira, Development of RuO_2-TiO_2 (70-30) mol% for pH measurements, Sensors and Actuators B: Chemical 113 (2) (2006) 1012-1016. https://doi.org/10.1016/j.snb.2005.03.087.

[182] A.V. Korotcov, Y.-S. Huang, K.-K. Tiong, D.-S. Tsai, Raman scattering characterization of well-aligned RuO_2 and IrO_2 nanocrystals, Journal of Raman Spectroscopy 38 (2007) 737-749. https://doi.org/10.1002/jrs.1655.

[183] J.E. Baur, T.W. Spaine, Electrochemical deposition of iridium (IV) oxide from

alkaline solutions of iridium (III) oxide, Journal of Electroanalytical Chemistry 443 (2) (1998) 208-216. https://doi.org/10.1016/S0022-0728(97)00532-9.

[184] K. Yamanaka, Anodically electrodeposited iridium oxide films (AEIROF) from alkaline solutions for electrochromic display devices, Japanese Journal of Applied Physics 28 (4R) (1989) 632-637. https://doi.org/10.1143/JJAP.28.632.

[185] P.J. Kinlen, J.E. Heider, D.E. Hubbard, A solid-state pH sensor based on a Nafion-coated iridium oxide indicator electrode and a polymer-based silver chloride reference electrode, Sensors and Actuators B: Chemical 22 (1) (1994) 13-25. https://doi.org/10.1016/0925-4005(94)01254-7.

[186] J.V. Dobson, P.R. Snodin, H.R. Thirsk, EMF measurements of cells employing metal-metal oxide electrodes in aqueous chloride and sulphate electrolytes at temperatures between 25-250 C, Electrochimica Acta 21 (7) (1976) 527-533. https://doi.org/10.1016/0013-4686(76)85143-2.

[187] K. Kinoshita, M.J. Madou, Electrochemical measurements on Pt, Ir, and Ti oxides as pH probes, Journal of the electrochemical society 131 (5) (1984) 1089-1094. https://doi.org/10.1149/1.2115755.

[188] S. Zhuiykov, Morphology of Pt-doped nanofabricated RuO_2 sensing electrodes and their properties in water quality monitoring sensors, Sensors and Actuators B: Chemical 136 (1) (2009) 248-256. https://doi.org/10.1016/j.snb.2008.10.030.

[189] L. Manjakkal, A. Vilouras, R. Dahiya, Screen printed thick film reference electrodes for electrochemical sensing, IEEE Sensors Journal 18 (19) (2018) 7779-7785. https://doi.org/10.1109/JSEN.2018.2840349.

[190] R. Martínez-Máñez, J. Soto, E. García-Breijo, L. Gil, J. Ibáñez, E. Gadea, A multisensor in thick-film technology for water quality control, Sensors and Actuators A: Physical 120 (2) (2005) 589-595.

https://doi.org/10.1016/j.sna.2005.03.006.

[191] R.H.G. Mingels, S. Kalsi, Y. Cheong, H. Morgan, Iridium and Ruthenium oxide miniature pH sensors: Long-term performance, Sensors and Actuators B: Chemical 297 (2019) 126779. https://doi.org/10.1016/j.snb.2019.126779.

[192] S. Trasatti, G. Buzzanca, Ruthenium dioxide: a new interesting electrode material. Solid state structure and electrochemical behaviour, Journal of electroanalytical chemistry and interfacial electrochemistry 29 (2) (1971) A1-A5. https://doi.org/10.1016/S0022-0728(71)80111-0.

[193] R.K. Shervedani, H.Z. Mehrdjardi, S.K. Ghahfarokhi, Electrochemical characterization and application of Ni-RuO$_2$ as a pH sensor for determination of petroleum oil acid number, Journal of the Iranian Chemical Society 4 (2) (2007) 221-228. http://dx.doi.org/10.1007/BF03245970.

[194] C. V. D'Alkaine, L. M. M. de Souza, F. C. Nart, The anodic behaviour of niobium-II. General experimental electrochemical aspects, Corrosion Science 34 (1) (1993) 117-127. https://doi.org/10.1016/0010-938X(93)90263-G.

[195] B. Reichman, A.J. Bard, Electrochromism at niobium pentoxide electrodes in aqueous and acetonitrile solutions, Journal of the Electrochemical Society 127 (1) (1980) 241-242. https://doi.org/10.1149/1.2129628.

[196] C.-M. Yang, T.-W. Chiang, Y.-T. Yeh, A. Das, Y.-T. Lin, T.-C. Chen, Sensing and pH-imaging properties of niobium oxide prepared by rapid thermal annealing for electrolyte-insulator-semiconductor structure and light-addressable potentiometric sensor, Sensors and Actuators B: Chemical 207 (2015) 858-864. https://doi.org/10.1016/j.snb.2014.10.097.

[197] G.R. Lee, J.A. Crayston, Studies on the electrochemical deposition of niobium oxide, Journal of Materials Chemistry 6 (2) (1996) 187-192.

https://doi.org/10.1039/JM9960600187.

[198] E. Gill, K. Arshak, A. Arshak, O. Korostynska, Mixed metal oxide films as pH sensing materials, Microsystem Technologies 14 (2008) 499-507. https://doi.org/10.1007/s00542-007-0435-9.

[199] J. Yan, G. Wu, N. Guan, L. Li, Nb_2O_5/TiO_2 heterojunctions: synthesis strategy and photocatalytic activity, Applied Catalysis B: Environmental 152 (2014) 280-288. https://doi.org/10.1016/j.apcatb.2014.01.049.

[200] C. Baruffaldi, U. Casellato, S. Cattarin, M. Musiani, B. Tribollet, B. Vercelli, Characterisation of the surface films formed on Nb during electrodissolution in aqueous alkali, Electrochimica Acta 47 (18) (2002) 2989-2997. https://doi.org/10.1016/S0013-4686(02)00202-5.

[201] R.A. Rani, A.S. Zoolfakar, J.Z. Ou, M.R. Field, M. Austin, K. Kalantar-zadeh, Nanoporous Nb_2O_5 hydrogen gas sensor, Sensors and Actuators B: Chemical 176 (2013) 149-156. https://doi.org/10.1016/j.snb.2012.09.028.

[202] A. Borgschulte, J. H. Rector, B. Dam, R. Griessen, A. Züttel, The role of niobium oxide as a surface catalyst for hydrogen absorption, Journal of Catalysis 235 (2) (2005) 353-358. https://doi.org/10.1016/j.jcat.2005.08.018.

[203] R. Ziel, A. Haus, A. Tulke, Quantification of the pore size distribution (porosity profiles) in microfiltration membranes by SEM, TEM and computer image analysis, Journal of membrane science 323 (2) (2008) 241-246. https://doi.org/10.1016/j.memsci.2008.05.057.

[204] S. Ravichandran, C. Thiagarajan, P.S. Kumar, pH sensitivity estimation in potentiometric metal oxide pH sensors using the principle of invariance, International Journal of Chemical Engineering 2021 (2021). https://doi.org/10.1155/2021/5551259.

[205] J.-Q. Li, L. Meng, J. Cheng, Thermodynamic conditions for the Nernstian response of the flat band potential of the metal oxide semiconductor: A theoretical study, The Journal of Physical Chemistry C 126 (1) (2022) 578-587. https://doi.org/10.1021/acs.jpcc.1c07625.

[206] K. Jung, Y. Kim, Y.S. Park, W. Jung, J. Choi, B. Park, H. Kim, W. Kim, J. Hong, H. Im, Unipolar resistive switching in insulating niobium oxide film and probing electroforming induced metallic components, Journal of Applied Physics 109 (5) (2011) 054511. https://doi.org/10.1063/1.3552980.

[207] V.L.S. Teixeira da Silva, M. Schmal, S.T. Oyama, Niobium carbide synthesis from niobium oxide: study of the synthesis conditions, kinetics, and solid-state transformation mechanism, Journal of Solid State Chemistry 123 (1) (1996) 168-182. https://doi.org/10.1006/jssc.1996.0165.

[208] L. Wang, J. Sun, B. Kang, S. Li, S. Ji, Z. Wen, X. Wang, Electrochemical behaviour and surface conductivity of niobium carbide-modified austenitic stainless steel bipolar plate, Journal of Power Sources 246 (2014) 775-782. https://doi.org/10.1016/j.jpowsour.2013.08.025.

[209] Z. Zhu, C.Y. Cheng, Solvent extraction technology for the separation and purification of niobium and tantalum: A review, Hydrometallurgy 107 (1-2) (2011) 1-12. https://doi.org/10.1016/j.hydromet.2010.12.015.

[210] A. Shikika, M. Sethurajan, F. Muvundja, M.C. Mugumaoderha, S. Gaydardzhiev, A review on extractive metallurgy of tantalum and niobium, Hydrometallurgy 198 (2020) 105496. https://doi.org/10.1016/j.hydromet.2020.105496.

[211] G.E. Cavigliasso, M.J. Esplandiu, V.A. Macagno, Influence of the forming electrolyte on the electrical properties of tantalum and niobium oxide films: an EIS comparative study, Journal of Applied Electrochemistry 28 (11) (1998) 1213-1219. https://doi.org/10.1023/A:1003449917148.

119

[212] J.-P. Dasquet, D. Caillard, E. Conforto, J.-P. Bonino, R. Bes, Investigation of the anodic oxide layer on 1050 and 2024T3 aluminium alloys by electron microscopy and electrochemical impedance spectroscopy, Thin Solid Films 371 (1-2) (2000) 183-190. https://doi.org/10.1016/S0040-6090(00)01016-6.

[213] F. M. Al-Kharafi, W. A. Badawy, Phosphoric acid passivated niobium and tantalum EIS-comparative study, Electrochimica Acta 40 (16) (1995) 2623-2626. https://doi.org/10.1016/0013-4686(95)00123- V.

[214] D.G. Li, J.D. Wang, D.R. Chen, Influence of potentiostatic aging, temperature and pH on the diffusivity of a point defect in the passive film on Nb in an HCl solution, Electrochimica Acta 60 (2012) 134–146. https://doi.org/10.1016/j.electacta.2011.11.024.

[215] M. Pourbaix, Atlas of chemical equilibria in aqueous solutions, Pergamon Press Ltd., pp. 246-250, Chennai, NY, 1966.

[216] S. Li, Q. Xu, E. Uchaker, X. Cao, G. Cao, Comparison of amorphous, pseudohexagonal and orthorhombic Nb_2O_5 for high-rate lithium ion insertion, CrystEngComm 18 (14) (2016) 2532-2540. https://doi.org/10.1039/C5CE02069G.

List of figures

List of tables

List of publications

Submitted

- T. M. Bruckner, <u>T. D. Singewald</u>, R. Gruber, L. Hader-Kregl, M. Müller, C. Kern, M. Hafner, C. Paulik, Influence of hollow glass microspheres on 1K epoxy structural adhesive for the automotive industry, Journal of Adhesion and Adhesives (2022).

- T. M. Bruckner, <u>T. D. Singewald</u>, R. Gruber, L. Hader-Kregl, M. Klotz, M. Müller, G. Luckeneder, M. Rosner, C. Kern, M. Hafner, C. Paulik, Water absorption and leaching of a 1K structural model epoxy adhesive for the automotive industry, Polymer Testing (2022).

Accepted/Published

- <u>T. D. Singewald,</u> T. M. Bruckner, R. Gruber, G. Schimo-Aichhorn, L. Hader-Kregl, S. Pöller, M. Müller, C. Kern, G. Luckeneder, K.-H. Stellnberger, B. Strauß, M. Hafner, M. Valtiner, Water-uptake in hollow glass microspheres and their influence on cathodic and anodic delamination along the polymer/metal-interface, Corrosion Science 196 (2022) 110045. https://doi.org/10.1016/j.corsci.2021.110045.

- <u>T. D. Singewald</u>, I. Traxler, G. Schimo-Aichhorn, S. Hild, M. Valtiner, Versatile, low-cost, non-toxic potentiometric pH-sensors based on niobium, Sensing and Bio-Sensing Research 35 (2022) 100478. https://doi.org/10.1016/j.sbsr.2022.100478.

- I. Traxler, <u>T. D. Singewald</u>, G. Schimo-Aichhorn, S. Hild, M. Valtiner, SECM methods and ion-selective microelectrodes for corrosion studies, Corrosion Reviews (2022) https://doi.org/10.1515/corrrev-2021-0104.

- <u>T. D. Singewald</u>, T. M. Bruckner, R. Gruber, G. Schimo-Aichhorn, L. Hader-

Kregl, S. Andronescu, M. Klotz, M. Müller, C. Kern, M. Rosner, G. Luckeneder, K.-H. Stellnberger, B. Strauß, M. Hafner, M. Valtiner, Systematic variation of inorganic additives and their impact on interfacial delamination processes of automotive coating systems, Progress in Organic Coatings 173 (2022) 107172. https://doi.org/10.1016/j.porgcoat.2022.107172.

Copyright clearances

CCC RightsLink®

Home | Help ∨ | Email Support | Sign in | Create Account

Water-uptake in hollow glass microspheres and their influence on cathodic and anodic delamination along the polymer/metal-interface

Author:
Tanja Denise Singewald,Thomas Maximillian Bruckner,Ralph Gruber,Gabriela Schimo-Aichhorn,Laura Hader-Kregl,Sascha Poeller,Mathias Mueller,Carina Kern,Gerald Luckeneder,Karl-Heinz Stellnberger,Bernhard Strauß,Martina Hafner,Markus Valtiner

Publication: Corrosion Science

Publisher: Elsevier

Date: March 2022

© 2021 Elsevier Ltd. All rights reserved.

CCC | RightsLink®

Home   Help ∨   Email Support   Sign in   Create Account

Versatile, low-cost, non-toxic potentiometric pH-sensors based on niobium

Author: Tanja Denise Singewald,Ines Traxler,Gabriela Schimo-Aichhorn,Sabine Hild,Markus Valtiner

Publication: Sensing and Bio-Sensing Research

Publisher: Elsevier

Date: February 2022

© 2022 Published by Elsevier B.V.

Journal Author Rights

BACK   CLOSE WINDOW

CCC | RightsLink®

| My Orders | My Library | My Profile | Welcome tanja.singewald@cest.at | Log out | Help | FAQ |

My Orders > Orders > All Orders

License Details

This Agreement between CEST GmbH -- Tanja Singewald ("You") and Elsevier ("Elsevier") consists of your license details and the terms and conditions provided by Elsevier and Copyright Clearance Center.

[Print] [Copy]

License Number	5324170831842
License date	Jun 08, 2022
Licensed Content Publisher	Elsevier
Licensed Content Publication	Elsevier Books
Licensed Content Title	Principles of Corrosion Engineering and Corrosion Control
Licensed Content Author	Zaki Ahmad
Licensed Content Date	Jan 1, 2006
Licensed Content Pages	48
Type of Use	reuse in a thesis/dissertation
Portion	figures/tables/illustrations
Number of figures/tables/illustrations	1
Format	both print and electronic
Are you the author of this Elsevier chapter?	No
Will you be translating?	No
Title	Interfacial processes in adhesively bonded joints under corrosive load
Institution name	Institute of Applied Physics, TU Vienna
Expected presentation date	Oct 2022
Portions	Figure 2.18: Potential-pH diagram for iron
Requestor Location	CEST GmbH Stahlstraße 2-4 Linz, Upper Austria 4020 Austria Attn: CEST GmbH
Publisher Tax ID	GB 494 6272 12
Total	**0.00 EUR**

https://s100.copyright.com Page 1 of 1

TU Bibliothek
Your knowledge hub
WIEN

CCC | RightsLink

Home | Help ∨ | Live Chat | Sign in | Create Account

Systematic variation of inorganic additives and their impact on interfacial delamination processes of automotive coating systems

Author:
Tanja Denise Singewald,Thomas Maximillian Bruckner,Ralph Gruber,Gabriela Schimo-Aichhorn,Laura Hader-Kregl,Sascha Andronescu,Michael Klotz,Mathias Müller,Carina Kern,Martin Rosner,Gerald Luckeneder,Karl-Heinz Stellnberger,Bernhard Strauß et al.

Publication: Progress in Organic Coatings

Publisher: Elsevier

Date: December 2022

© 2022 Published by Elsevier B.V.

Journal Author Rights

BACK   CLOSE WINDOW

Curriculum Vitae

Personal Data

Name:	Singewald, Tanja Denise
E-Mail:	tanja.singewald@gmx.at

Education

Since 09/2019	**Technische Universität, Vienna** Doctoral programme in Engineering Sciences Diploma programme: Technical Physics Doctoral thesis: *Interfacial processes in adhesively bonded joints under corrosive load*
10/2017 – 08/2019	**Johannes-Kepler-Universität, Linz** Master program in Technical Chemistry Thesis Title: *Characterization of Complex Cross-Linked Polymers by Pyrolysis-GC/MS* Degree: Dipl.-Ing.
10/2010 – 06/2017	**Johannes-Kepler-Universität, Linz** Bachelor in Technical Chemistry Thesis Title: *Analysis of Clindamycin and Quinolones using Capillary Electrophoresis* Degree: Bachelor of Science

Work Experience

12/2020 – 12/2021	**External lecturer, FH Wels Lab worker** Lab course – Corrosion and corrosion protection
09/2018 – 09/2019	**Lab worker, Patheon Austria GmbH & Co KG, part of Thermo Fisher, Linz** Quality control – IR spectrometry, 10 h / week
07/2018 – 09/2018	**Internship, Patheon Austria GmbH & Co KG, part of Thermo Fisher, Linz** Quality control – IR spectrometry
07/2017 – 09/2017	**Internship, Patheon Austria GmbH & Co KG, Linz** Quality control – HPLC & wet chemistry

07/2016 – 08/2016	**Volunteer - Marine Dynamics and Dyer Island Cruises, South Africa**
07/2015 – 09/2015	**Internship, DPx Fine Chemicals Austria, Linz** Quality control – wet chemistry
07/2014 – 08/2014	**Internship, DSM Fine Chemicals Austria, Linz** Quality control – wet chemistry
10/2013 – 06/2018	**Tutor, Open Lab Linz** School laboratory
07/2006 – 08/2006	**Internship, Community Office, Rechberg**

Skills

Languages:
- German, native speaker
- English, advanced

Computer:
- MS Office (Word, Power-Point, Excel), advanced skills
- Origin Pro

Conference contributions

- EuroCorr2021 (Talk): "Investigations of water transport behavior and interfacial delamination of zinc coated steel/epoxy adhesive systems in NaCl solution".

- Euradh 2021 (Talk): "Investigations of structural adhesives for the automotive industry with focus on interfacial delamination and water absorption using EIS and SKP".

- COAST2022 (Poster): "Investigations of structural adhesives using EIS and HR-SKP".

- EuroCorr2022 (Talk): "Electrochemically produced pH sensors based on niobium for corrosion monitoring".

- Adhesion 2022 (Talk): "Progress of delamination and water transport in epoxy adhesives on galvanized steel surfaces in NaCl solution".
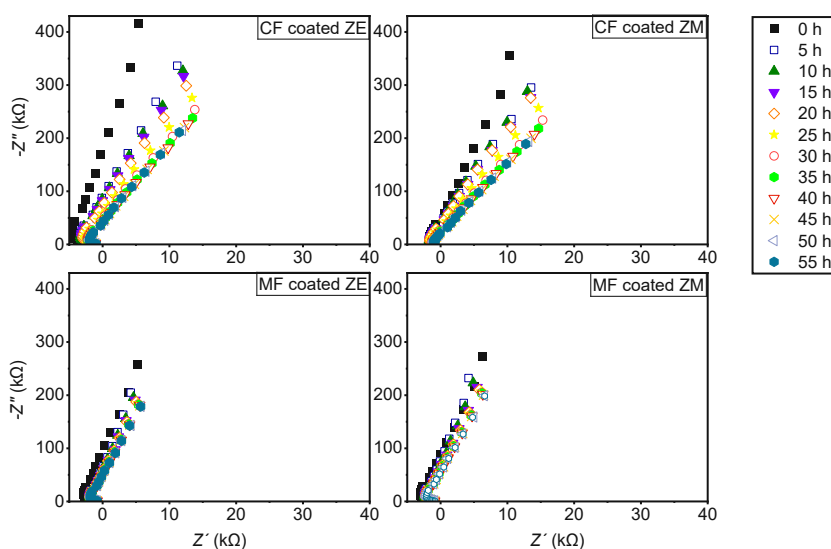
Appendices

A.1 The Bode diagrams and the Nyquist diagrams where the selected frequencies were marked with dotted lines in the Bode plots
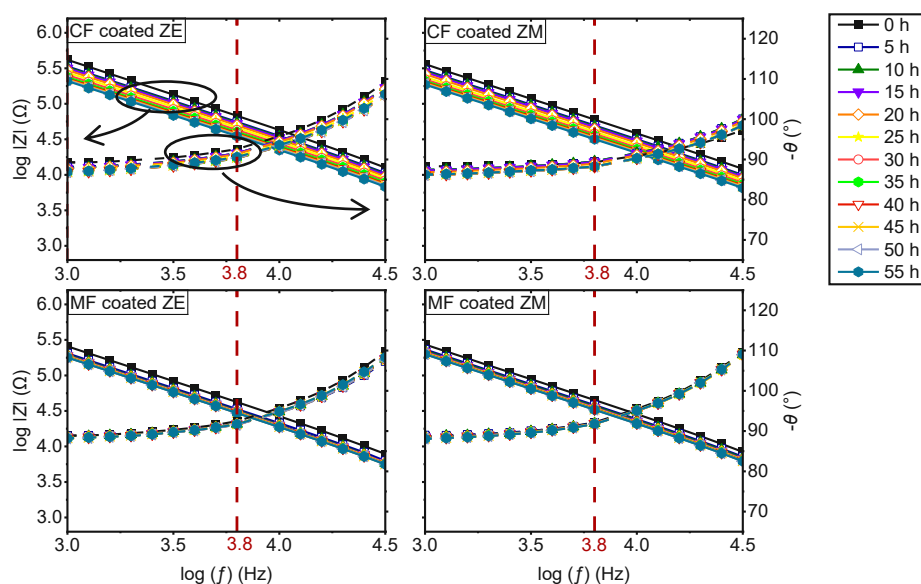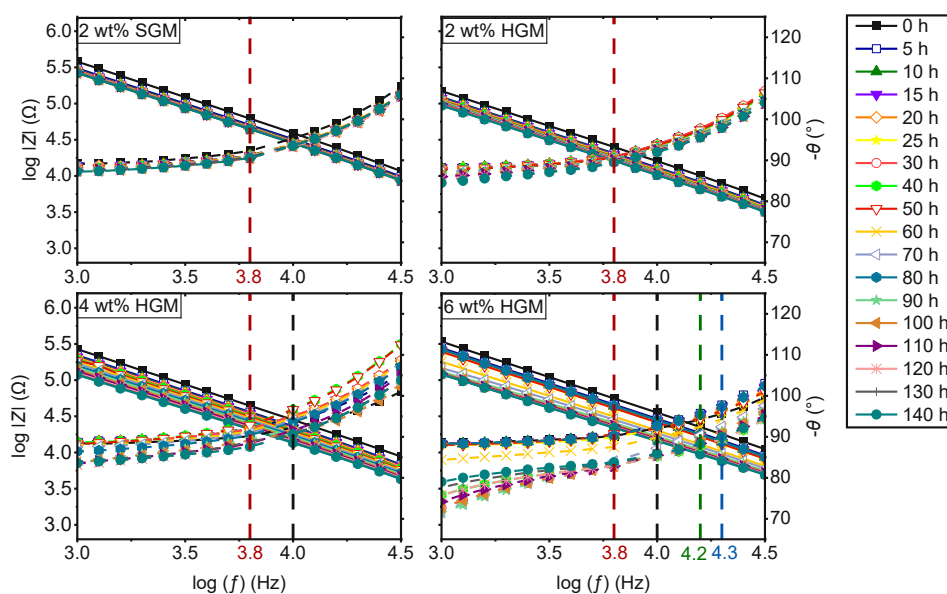

Figure A.1.1: Bode plots of CF and MF coated ZE and ZM exposed to 3.5 wt% NaCl solution for 55 h at room temperature with the red line marking the frequency chosen to calculate the coating capacitance at t = 0-140 h.
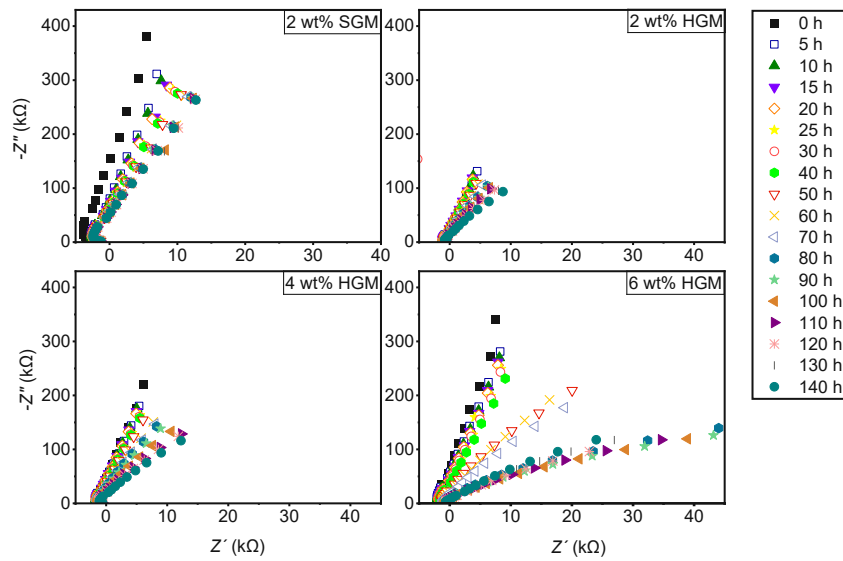
Figure A.1.2: Nyquist plots of CF and MF coated ZE and ZM exposed to 3.5 wt% NaCl solution for 55 h at room temperature.

Figure A.1.3: Comparison of the Bode plots of ZE coated with MF mixed with 2 wt% SGM, 2 wt% HGM, 4 wt% HGM and 6 wt% HGM exposed to 3.5 wt% NaCl solution for 140 h at room temperature with the lines marking the frequencies chosen to calculate the coating capacitance.

Figure A.1.4: Comparison of the Nyquist plots of ZE coated with MF mixed with 2 wt% SGM, 2 wt% HGM, 4 wt% HGM and 6 wt% HGM exposed to 3.5 wt% NaCl solution for 140 h at room temperature.